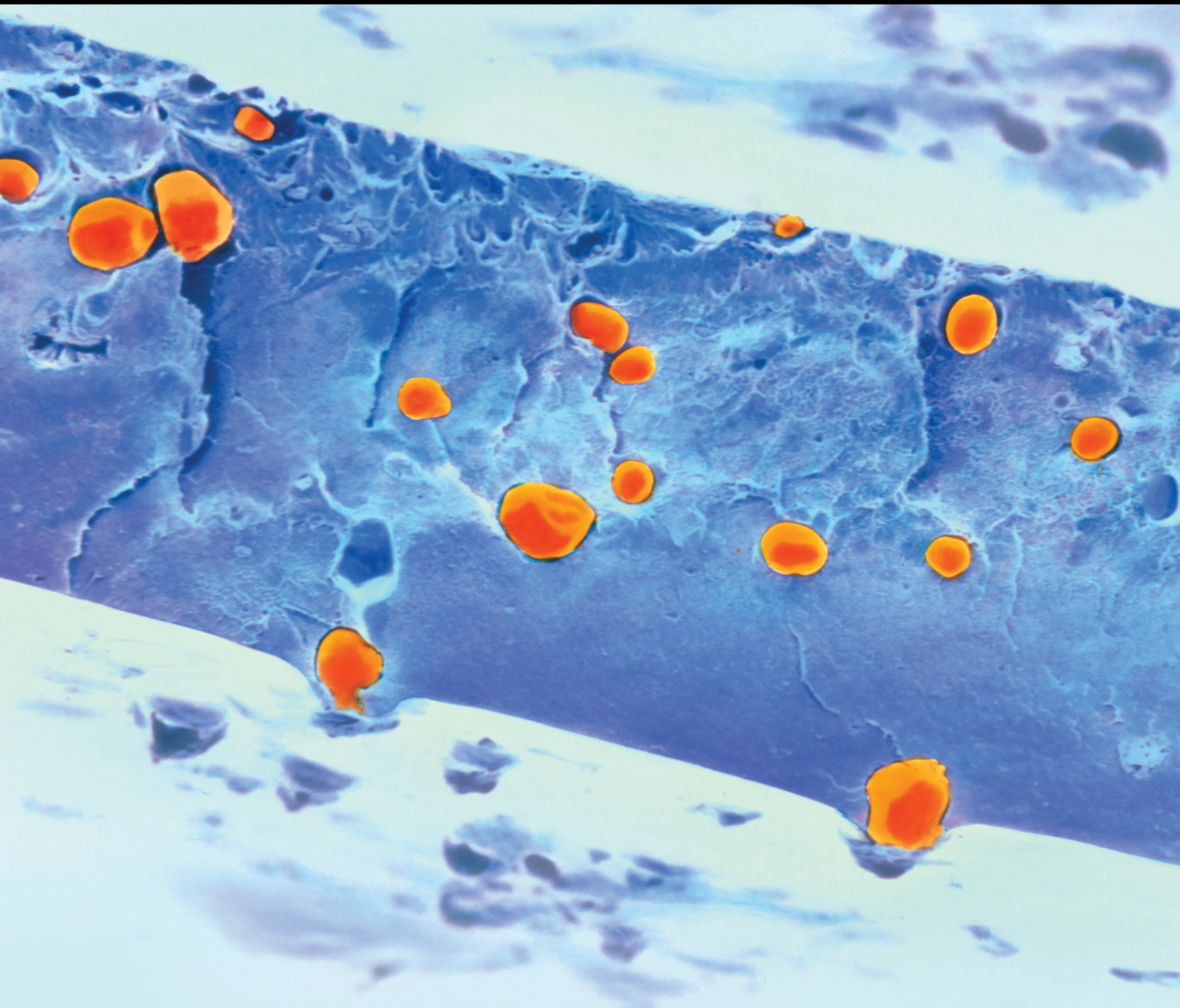# Natural-Based Nanocomposites and their Biomedical Applications

Lead Guest Editor: Ehsan Nazarzadeh Zare
Guest Editors: Pooyan Makvandi, Ai-min Wu, and Yuting Huang

Natural-Based Nanocomposites and their Biomedical Applications

Natural-Based Nanocomposites and their Biomedical Applications

Lead Guest Editor: Ehsan Nazarzadeh Zare
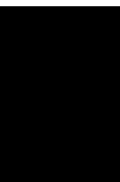Guest Editors: Pooyan Makvandi, Ai-min Wu, and
Yuting Huang

Chief Editor

Contents

Research Article

Spectroscopic Investigation of Chlorin-Based Photosensitizers in Polymer Matrix

Antonina Naumenko [1] and **Nataliya Kutsevol** [2]

[1]*Faculty of Physics, Taras Shevchenko National University of Kyiv, Kyiv, 01601, Ukraine*
[2]*Faculty of Chemistry, Taras Shevchenko National University of Kyiv, Kyiv, 01601, Ukraine*

Correspondence should be addressed to Antonina Naumenko; a_naumenko@univ.kiev.ua

Chlorin e6 and its derivatives are the basis of a number of drugs used in medicine in the treatment of various diseases, including cancer, by photodynamic therapy. Nonpolar derivatives of Chlorin e6—dimethyl ether of Chlorin e6 (DME Ce6) and trimethyl ether of Chlorin e6 (TME Ce6)—are actively studied for application during photodynamic therapy. In this work, based on the electron optical absorption spectra, the interaction of photosensitizer molecules with branched star-like copolymer dextran-graft-polyacrylamide in anionic form was investigated and the possibility of using the latter as a carrier for drug delivery to tumor cells was suggested.

1. Introduction

Photodynamic therapy (PDT) is an advanced method of treating cancer and various benign diseases, including infections [1]. The main components for photochemical reactions are light-activable molecule-photosensitizer (PS), light, and oxygen [2]. The principle of the method of PDT is that PS under irradiation with light of a specific wavelength is able to initiate the generation of singlet oxygen and other reactive oxygen species that either kill tumor cells directly or damage tumor vasculature [3, 4]. PDT has a number of advantages over conventional methods of cancer treatment. Among the PSs of natural or synthetic origin, the most promising is Chlorin e6 (Ce6), boasting high efficacy and very low toxicity [5, 6]. There are a number of drugs based on Ce6 or its derivatives that have been already created and applied in the clinic, such as Photolon, Radachlorin, Photoditazin, Talaporfin, and Pirlitin. To date, several modified derivatives of this compound have been developed that would increase the effectiveness of PDT. The low solubility of Chlorin e6 and its derivatives in water forces them to look for special carriers for their address delivery. A modern trend in PDT is the use of multifunctional polymer nanocarriers which can enhance target-oriented PDT. The polymer nanocarriers can be of few types: linear and branched polymers, dendrimers, micelles, and nanogels [7]. Our previous study has shown that branched star-like copolymer dextran-graft-polyacrylamide in anionic form could be efficient nanocarriers for drug delivery to tumor cells [7]) and can be efficient matrices for in situ synthesis of gold nanoparticles [8]. The theoretical [9–11] and experimental [12, 13] studies of star-like polymers proved that branched macromolecules have a higher local concentration of functional groups capable of binding drugs or other substances causing its incorporation into polymer nanocarriers.

The characteristics of the nanocomposite depend on the properties of PS and polymer matrices. The aim of this work was the comparative investigation of the absorption and fluorescence spectra of Chlorin e6, dimethyl ether of Chlorin e6, and trimethyl ether of Chlorin e6 (Ce6, DME Ce6, and TME Ce6, respectively) both in aqueous solutions and in water solution of branched polymer dextran-graft-polyacrylamide.

2. Materials and Methods

In this work, Chlorin e6 (Frontier Scientific, USA) was used. The Chlorin e6 (Ce6) derivatives dimethyl ester (DME Ce6) and trimethyl ester (TME Ce6) of Chlorin e6 were obtained
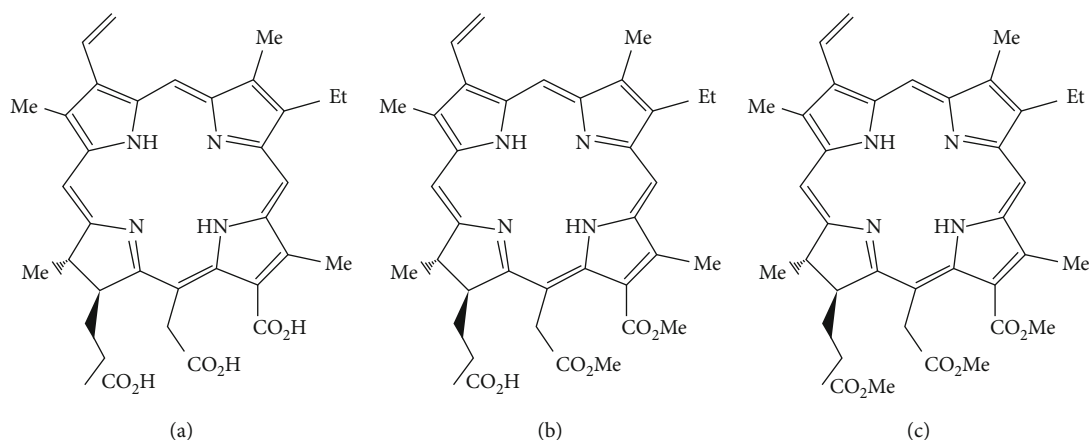
Figure 1: The structural formulas of the studied PSs: Ce6 (a), DME Ce6 (b), and TME Ce6 (c).

from the Laboratory of Biophysics and Biotechnology (Belarusian State University, Belarus). The structural formulas of the studied PSs are presented in Figure 1. As can be seen, the DME Ce6 and TME Ce6 molecules differ from the Ce6 molecule by the presence of two or three ether groups instead of carboxyl ones, which leads to their greater hydrophobicity and, consequently, the probability of aggregation of these molecules in aqueous solutions increases

Stock (concentrated) solutions of the Chlorin-type photosensitizers were prepared by dissolving the PS powder in ethanol. The weight was determined using analytical balance Vibra (Japan); the weighing accuracy is 0.05 mg. The solutions were prepared as follows: first, a stock solution in ethanol (2×10^{-3} M) was prepared; then, it was diluted in water to a concentration of 10^{-5} M.

As a nanocarrier, a branched copolymer obtained by grafting polyacrylamide (PAA) chains onto dextran ($M_w = 7 \times 10^4$ g/mol^{-1}) backbone was used. The details of the synthesis, identification, and analysis of the internal polymer structure were described in [14, 15]. The theoretical number of grafted polyacrylamide chains to the polysaccharide backbone for the sample we used as a polymer nanocarrier in the present work was equal to 5, and the related dextran-graft-polyacrylamide copolymer was referred to as D70-g-PAA. Molecular parameters of the polymer sample are $M_w = 2.15 \times 10^{-6}$ g/mol, $R_g = 85$ nm, and $M_w/M_n = 1.72$. The choice of this copolymer among the series of the branched samples synthesized was based on our previous research.

The D70-g-PAA copolymer was saponified by alkaline hydrolysis, by using NaOH to obtain branched polyelectrolyte dextran-graft-(polyacrylamide-co-polyacrylic acid) referred to as D70-g-PAA (PE) throughout [16]. The degree of saponification of carbamide groups to carboxylate ones in PAA-grafted chains determined by the potentiometric titration was equal to 43% [16].

The absorption spectra were registered with a spectrophotometer Cary 60 (Agilent) in the range of 200–800 nm. The spectral resolution was 1 nm. Fluorescence spectra were registered with a Cary Eclipse (Varian, Australia) fluorescent spectrophotometer in the range of 200–800 nm. The spectral width of slits for fluorescence measurements was of 5 nm. The

recording of all the spectra were carried out in standard quartz cuvettes $1 \times 1 \times 4$ cm (transmission range 170–1000 nm).

3. Results and Discussion

3.1. The Manifestation of Chemical Structure of Photosensitizers (Ce6, DME Ce6, and TME Ce6) in Absorption Spectra. Due to the highly coupled pi-electron system, porphyrins have a very characteristic absorption spectrum: one, the so-called Soret band, a very intense band in the region of 380–420 nm, and several less intense bands in the region of 500–750 nm (Q-band). Figure 2 shows absorption spectra of aqueous solutions of Ce6, DME Ce6, and TME Ce6.

In the absorption spectrum of the molecules under study in the UV and visible spectral regions, the distribution and intensity of absorption maxima characteristic of Chlorins are observed. The most intense bands appear at the boundary of the visible and UV regions of the spectrum at 399 nm (the Soret band) and at the boundary of the visible and IR regions of the spectrum at 662 nm. The optical density of Soret bands is approximately the same for all three compounds. The broadening of the bands and their redshift indicate an increase in aggregation processes with increasing hydrophobicity of the system. At the same time, the intensity of bands in the vicinity of Q-band at ~670 nm increases in the row: Ce6 ⟶ DME Ce 6 ⟶ TME Ce6, i.e., demonstration increasing of ratio D_{670}/D_{405} and enhancement of PDT activity of molecules. These results are in good agreement with published data [17, 18].

3.2. The Influence of Polymer Matrix on Absorption Spectra of Chlorin-Based Photosensitizer. The absorption spectra of Ce6 solutions in water and in anionic polymer D70-g-PAA (PE) are shown in Figure 3. The most intense Soret band (maximum absorption 405 nm) is located in the close UV range, while the Q-band (504 and 648 nm) is in the red part of the spectrum. The general appearance of the experimentally recorded spectrum coincides with the literature data [17, 18]. The following spectra show that the shape of the band in the absorption spectrum in the visible range of the photosensitizer Ce6 dissolved in water and in the presence of polymer D70-g-PAA (PE) practically does not change the optical
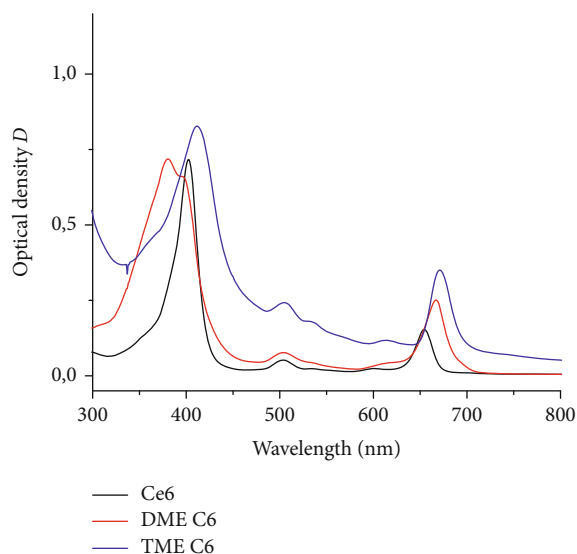
FIGURE 2: Absorption spectra of aqueous solutions of Ce6 (black line), DME Ce6 (red), and TME Ce6 (blue line).
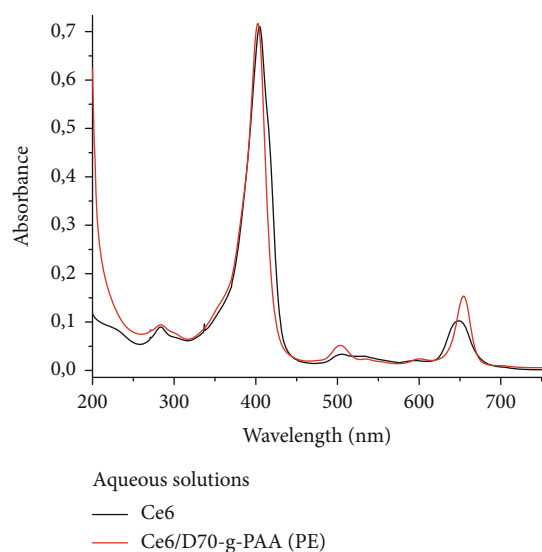
FIGURE 3: The absorption spectrum Ce6 solutions in water and with the presence of anionic polymer.

density, but the ratio changes of Soret and Q-band intensities are clearly visible. It has also been found that, depending on the polymer, the spectral position and optical absorption density of the Soret band and the Q-band with a maximum of 504 nm remain unchanged, while for the Q-band located around 650 nm, there is a slight redshift for the ionic polymer 648 $\longrightarrow$ 654 nm. Additionally, it can be seen that the bands become slightly narrower, which indicates that the presence of the polymer interferes with the aggregation processes inherent in the aqueous solutions of Ce6.

Figure 4 displays the more detailed absorption spectra of Ce6, DME Ce6, and TME Ce6 solutions in water and in

anionic polymer matrix D70-g-PAA (PE) in the vicinity of the Soret band. If we compare the shape of the Soret band lines for Ce6 and its modified forms, we will see the following features: for Ce6, it becomes narrower and symmetrical; the barely noticeable redshift of the shoulder, indicating the presence of aggregation in aqueous solution, disappears; for TME Ce6, there is a small low-frequency shift; for DME Ce6, a doublet structure is clearly observed. Such changes indicate that all three photosensitizers are embedded in the polymer matrix, but differently. This is especially true of Ce6 dimethyl ether, the absorption spectrum of which (the doublet nature of the Soret band) can demonstrate the aggregation of photosensitizer molecules that may not integrate into the polymer structure.

Regarding Q-bands in the spectral region at 450–620 nm (Figures 3 and 5), one can see that Ce6 shows the greater sensitivity to the polymer matrix, while for DME Ce6 and TME Ce6, they remain virtually unchanged.

Of particular interest is the band Q4, because greater is the PDT effect achieved for more intensity of this band. Figure 5 shows that in the presence of polymer, the shape of this band becomes more symmetrical and sharp, and its intensity increases in the row: Ce6 → DME Ce6 → TME Ce 6. Such changes in the spectrum once again confirm the fact of preventing the aggregation of photosensitizer molecules by the polymer matrix. Note that there is a redshift of the bands, which is an important factor for the effectiveness of PDT.

A generalized analysis of the spectral position of the bands is given in Table 1.

3.3. The Manifestation of Chemical Structure of Photosensitizers (Ce6, DME Ce6, and TME Ce6) in Absorption Spectra.
The interaction of the studied photosensitizers with the polymer matrix was also confirmed by the fluorescence spectra, which are presented in Figure 6.

Ce6 in the presence of a polymer gives the PL spectrum already described in the literature [17, 18]. The PL excitation spectrum coincides with the absorption spectrum, which indicates that the same centers are involved in the absorption and emission processes.

The fluorescence spectrum of Ce6 in the polymer when excited by radiation with $\lambda = 405$ nm (Figure 6(a), red line) shows an intense band with a maximum of 661 nm and a low-intensity broad shoulder of ~715 nm. In the same figure, the black line shows the absorption spectrum, which completely coincides with the excitation spectrum (dashed red line) of fluorescence, which indicates participation in the radiation process of the same centers.

For DME C6 (Figure 6(b)), the fluorescent band is redshifted by 2 nm. The shape of this line remains unchanged. But a comparison of the fluorescence excitation spectrum with the absorption spectrum indicates that the Soret band is a doublet, but intensities are "pumped," and the main contribution to the emission is made by the transition represented by the 399 nm band, which is less intense in the absorption spectrum, and the more intense absorption band (380 nm) in the PL excitation spectrum is presented only in the form of a low-intensity short-wavelength "shoulder."
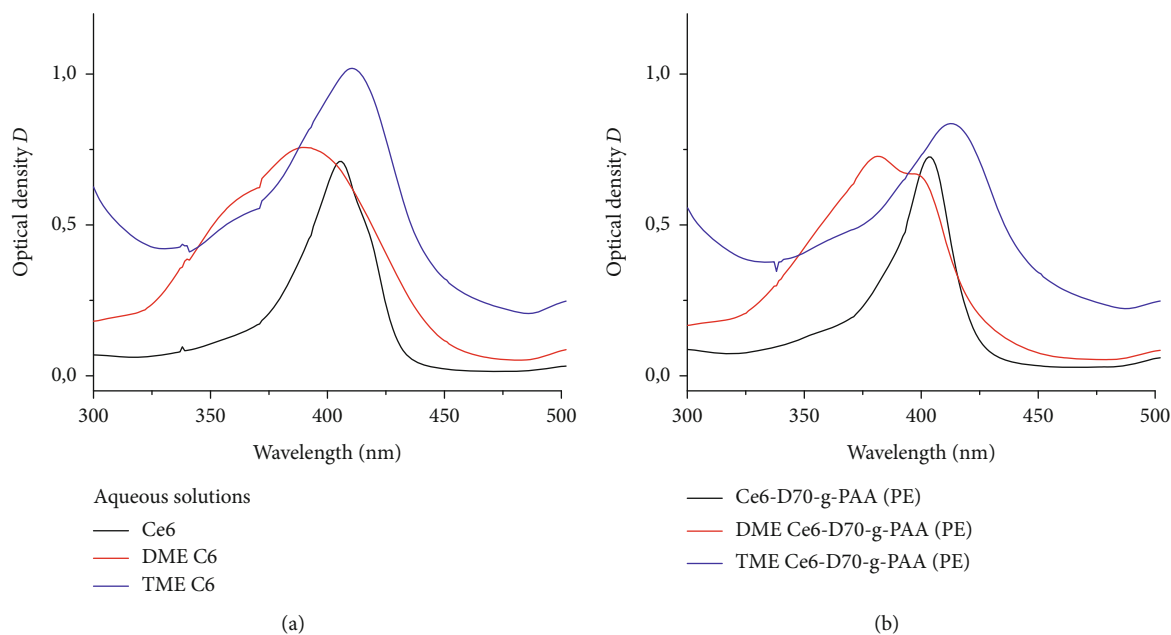
FIGURE 4: Absorption spectra of aqueous (a) and polymer (b) solutions of photosensitizers Ce6 (black line), DME Ce6 (red line), and TME Ce6 (blue line) in the region of Soret band.
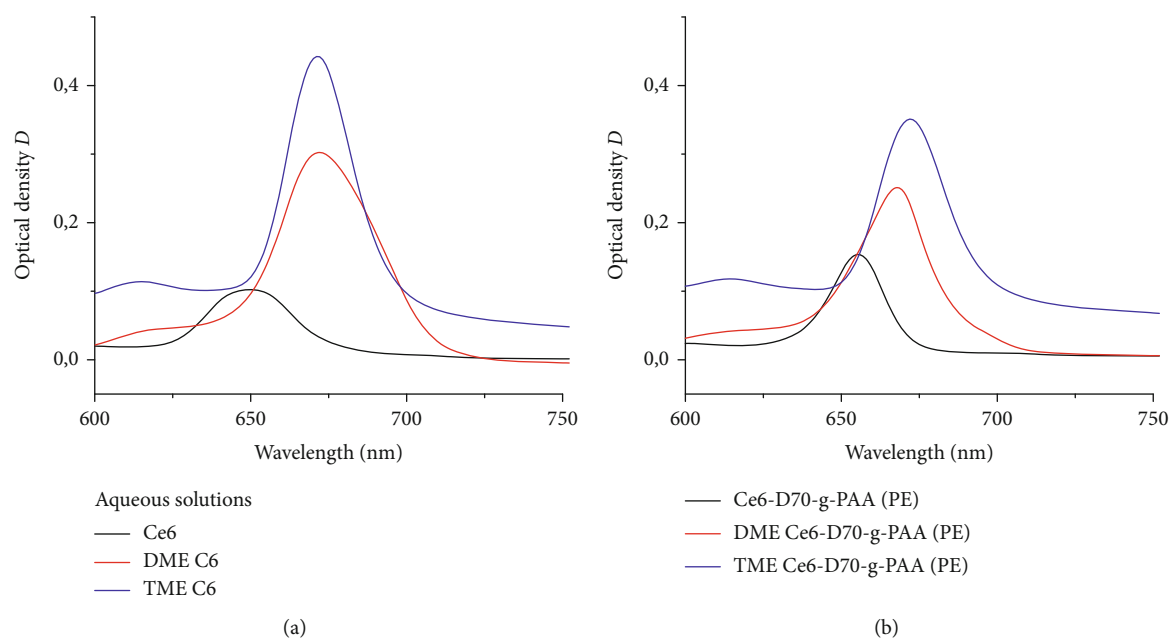
FIGURE 5: Absorption spectra of aqueous (a) and polymer (b) solutions of photosensitizers Ce6 (black line), DME Ce6 (red line), and TME Ce6 (blue line) in the region of Q4 band.

The TME Ce6 spectrum (Figure 6(c)) differs significantly from the two previous ones: first, an unexpected high-intensity band ~420 nm appeared, and second, in the region of the Q4 band, we see two bands with maxima of 678 and 752 nm. The spectral positions of these bands correspond to the Q4 band in the previous spectra (an intense band at 661 and 663 cm^{-1} in Ce6 and DME Ce6, respectively, and a broad low-intensity band at about 750 nm) at 678 and 752 nm. However, in this case, a redistribution of intensities occurred, and the second band (represented in the spectra of Ce6 and DME Ce6 by a wide low-intensity band) is narrow and clearly pronounced, and its intensity exceeds the intensity of the main Q4 band. That is, we see a significant increase in the probability of transition. The PL excitation spectrum indicates that the emission center is the same as for Ce6 and DME C6. For correct interpretation, it is necessary to carry out quantum mechanical calculations.

TABLE 1: The position of the bands in the absorption spectra of Ce6, DME Ce6, and TME Ce6 and composites D-g-PAA/Ce6, D-g-PAA/DME Ce6, and D-g-PAA/TME Ce6.

| PS/solution | Spectral position of absorption bands (nm), FWHM (nm), and optical density | | | | | |
| | Soret | | | Q4 | | |
	λ	FWHM	D	λ	FWHM	D
Ce6	405	34	0.91	648	33	0.1
Ce6/D70-g-PAA (PE)	402	28	0.72	654	22	0.15
DME Ce6	389	82	0.76	671	37	0.3
DME Ce6/D70-g-PAA (PE)	380 399	62	0.72 0.65	667	29	0.25
TME Ce6	410	65	1.02	670	26	0.44
TME Ce6/D70-g-PAA (PE)	412	54	0.83	671	24	0.35

Ce6/d70-g-PAA (PE)
— Absorption
— Emission
--- Emission excitation

(a)

DME Ce6/D70-g-PAA (PE)
— Absorption
— Emission
--- Emission excitation

(b)

TME Ce6/D70-g-PAA (PE)
— Absorption
— Emission
--- Emission excitation

(c)
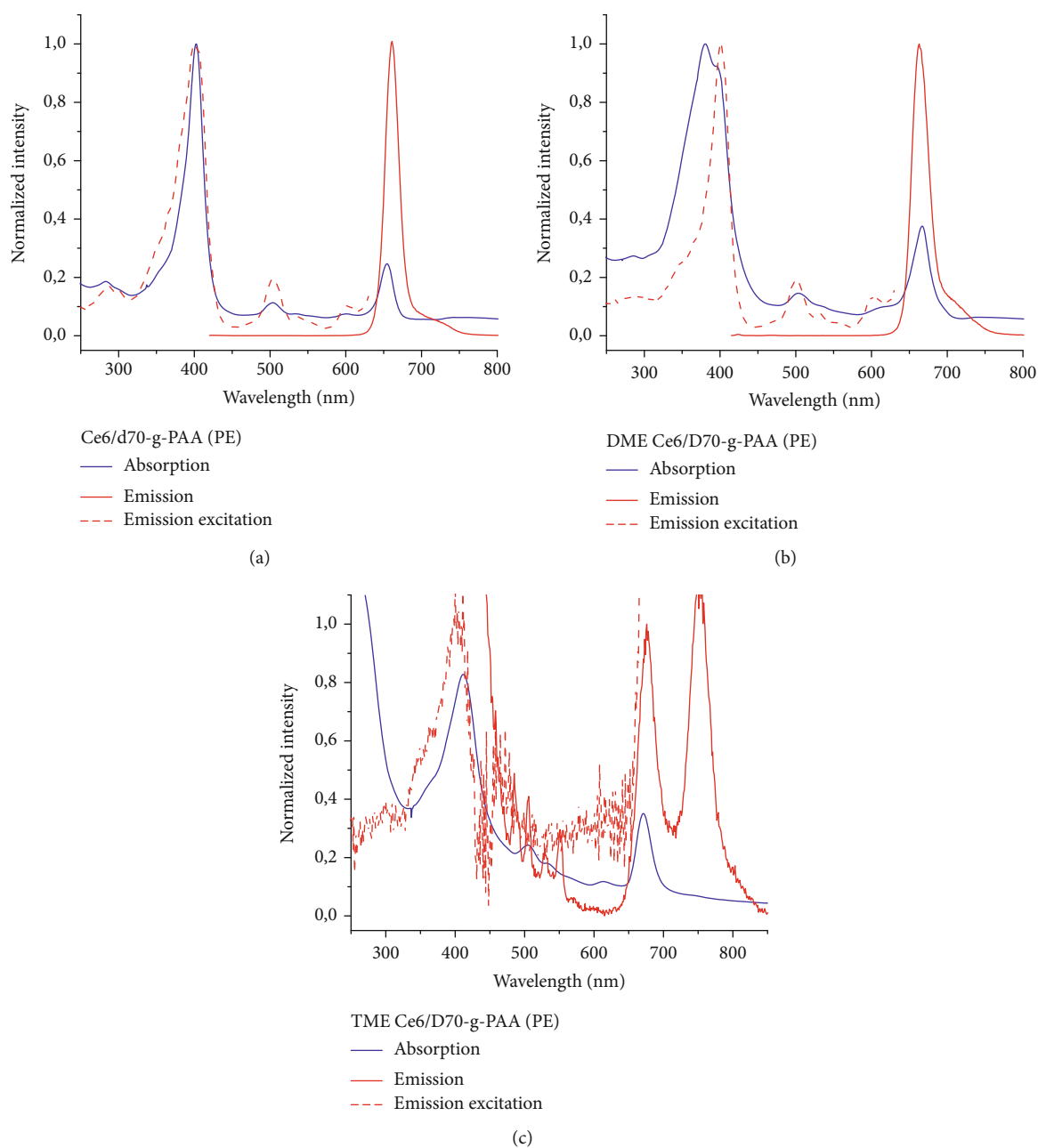
FIGURE 6: Fluorescence (red line) and fluorescence excitation (dotted red line) spectra of PS/D70-g-PAA (PE) systems, where PS = Ce6 (a), DME Ce6 (b), and TME Ce6 (c). The absorption spectra for comparison are given by a blue line.

4. Conclusions

The spectral characteristics of nanosystem polymer/photo-sensitizers of the Chlorin series have been studied. Comparison of the absorption and fluorescence spectra of solutions of Ce6 in water and in the presence of polymers dextran-polyacrylamide in anionic form showed a visible effect of the anionic matrix on the photophysical properties of studied photosensitizers. It was shown that in the absorption spectra of aqueous Ce6 and its modified forms—dimethyl (DME) and trimethyl (TME) esters—in the UV range and the visible range of the spectrum, there is a characteristic position of absorption maxima: Soret band 389-410 nm and Q-band 506, 536, and 590-616 nm; however, upon transition from Ce6 to DME and TME, changes in the intensities and band shapes of these spectra are observed. The broadening of the bands and their redshift indicate an increase in aggregation processes in aqueous solutions of threes PSs with increasing hydrophobicity of the system. It was shown that the polymer matrix effectively prevents the aggregation processes of photosensitizers. A comparison of the absorption spectra of PS/D70-g-PAA (PE) systems with the corresponding aqueous solutions showed that in the presence of a polymer, the FWHM of the characteristic bands decrease, which indicates an increase in the PS monomer content in the solutions. The shifts of the maxima of the position of the Soret band (blue for DME and red for TME) and Q4 band indicate the incorporation of PS into the polymer matrix, i.e., complex formation. This is also confirmed by fluorescence spectra. In addition, the redshift of the Q4 band in the row Ce6-DME Ce6-TME Ce6 and appearance of the band at 752 nm (for TME Ce6) when these PSs are introduced into the polymer matrix makes them somewhat more promising for PDT in comparison with aqueous solutions. In addition, the redshift of the Q4 band in the Ce6-DME-TME series and the appearance of a band at 752 nm (for TME), when these PSs are introduced into the polymer matrix, make them more promising for PDT compared to aqueous solutions.

Data Availability

Data is available on request.

Conflicts of Interest

The authors declare that there is no conflict of interest regarding the publication of this paper.

Acknowledgments

References

[1] P. Huang, J. Lin, X. Wang et al., "Light-triggered theranostics based on photosensitizer-conjugated carbon dots for simultaneous enhanced-fluorescence imaging and photodynamic therapy," *Advanced Materials*, vol. 24, no. 37, pp. 5104–5110, 2012.

[2] D. van Straten, V. Mashayekhi, H. S. de Bruijn, S. Oliveira, and D. J. Robinson, "Oncologic photodynamic therapy: basic principles, current clinical status and future directions," *Cancers (Basel)*, vol. 9, 2017.

[3] A. C. Kübler, "Photodynamische Therapie," *Medical Laser Application*, vol. 20, no. 1, pp. 37–45, 2005.

[4] K. Plaetzer, B. Krammer, J. Berlanda, F. Berr, and T. Kiesslich, "Photophysics and photochemistry of photodynamic therapy: fundamental aspects," *Lasers in Medical Science*, vol. 24, no. 2, pp. 259–268, 2009.

[5] H. Kataoka, H. Nishie, N. Hayashi et al., "New photodynamic therapy with next-generation photosensitizers," *Annals of Translational Medicine*, vol. 5, no. 8, p. 183, 2017.

[6] H. Wang and G. L. Rempel, "Introduction of polymer nanoparticles for drug delivery applications," *Nanotechnology: Nanomedicine&Nanobiotechnology*, vol. 2, pp. 1–6, 2015.

[7] K. Shrof and A. Vidyasagar, "Polymer nanoparticles: newer strategies towards targeted cancer therapy," *Journal of Physical Chemistry & Biophysics*, vol. 3, p. 125, 2013.

[8] V. A. Chumachenko, I. O. Shton, E. D. Shishko, N. V. Kutsevol, A. I. Marinin, and N. F. Gamaleia, "Branched copolymers dextran-graft-polyacrylamide as nanocarriers for delivery of gold nanoparticles and photosensitizers to tumor cells," in *Chapter in the Book: Nanophysics, Nanophotonics, Surface Studies, and Applications*, Volume 183 of the Series Springer Proceedings in Physics, pp. 379–390, OlenaFesenko, Leonid Yatsenko, 2016.

[9] O. A. Yeshchenko, N. V. Kutsevol, and A. P. Naumenko, "Light-induced heating of gold nanoparticles in colloidal solution: dependence on detuning from surface plasmon resonance," *Plasmonics*, vol. 11, no. 1, pp. 345–350, 2016.

[10] H. Merlitz, C. H. Wu, and J. U. Sommer, "Starlike polymer brushes," *Macromolecules*, vol. 44, no. 17, pp. 7043–7049, 2011.

[11] R. Everaers, A. Y. Grosberg, M. Rubinstein, and A. Rosa, "Flory theory of randomly branched polymers," *Soft Matter*, vol. 13, no. 6, pp. 1223–1234, 2017.

[12] N. V. Kutsevol, V. A. Chumachenko, M. Rawiso, V. F. Shkodich, and O. V. Stoyanov, "Star-like polymers dextran–polyacrylamide: the prospects of application for nanotechnology," *Journal of Structural Chemistry*, vol. 56, no. 5, pp. 1016–1023, 2015.

[13] F. Boué, J. Combet, B. Demé, M. Heinrich, J. G. Zilliox, and M. Rawiso, "SANS from salt-free aqueous solutions of hydrophilic and highly charged star-branched polyelectrolytes," *Polymers*, vol. 8, no. 6, p. 228, 2016.

[14] V. Solano-Umaña and J. R. Vega-Baudrit, "Gold and silver nanotechnology on medicine," *Journal of Chemistry and Biochemistry*, vol. 3, no. 1, pp. 21–33, 2015.

[15] M. Bezuglyi, N. Kutsevol, M. Rawiso, and T. Bezugla, "Water-soluble branched copolymers dextran-polyacrylamide and their anionic derivates as matrices for metal nanoparticles in-situ synthesis," *Chem*, vol. 66, no. 8, pp. 862–867, 2012.

[16] N. Kutsevol, M. Bezuglyi, M. Rawiso, and T. Bezugla, "Star-like dextran-graft-(polyacrylamide-co-polyacrylic acid) copolymers," *Macromolecular Symposia*, vol. 335, no. 1, pp. 12–16, 2014.

[17] S. N. Sakalou, S. L. Fiedaruk, T. V. Trukhacheva, and V. P. Kheidorov, "131,152-Dimethyl ester of chlorin e6 is a new photosensitizer. The proof of structure and purity," *Vestnik Farmatsii*, vol. 74, no. 4, pp. 53–61, 2016.

[18] T. E. Zorina, I. V. Yankovsky, I. V. Yakovets et al., "Intracellular localization and phototoxicity mechanisms of Chlorin e6 derivatives and their liposomal formulations," *Biophysics*, vol. 64, no. 4, pp. 533–542, 2019.

Research Article

Novel Nanoparticle Biomaterial of Alginate/Chitosan Loading Simultaneously Lovastatin and Ginsenoside RB1: Characteristics, Morphology, and Drug Release Study

Quan Vo-An,[1] **Thuy Chinh Nguyen** **Quang Tung Nguyen** **Quoc Trung Vu,**[4] **Cong Doanh Truong,**[3] **Thi Len Nguyen,**[3] **Thi Ngoc Lien Ly,**[3] **Long Giang Bach,**[5] **and Hoang Thai**

[1]*Institute for Tropical Technology, Vietnam Academy of Science and Technology, 18 Hoang Quoc Viet, Cau Giay, Ha Noi 100000, Vietnam*
[2]*Graduate University of Science and Technology, Vietnam Academy of Science and Technology, 18 Hoang Quoc Viet, Cau Giay, Ha Noi 100000, Vietnam*
[3]*Hanoi University of Industry, No. 298, Cau Dien Street, Bac Tu Liem District, Ha Noi 100000, Vietnam*
[4]*Faculty of Chemistry, Hanoi National University of Education, No. 136 Xuan Thuy Road, Cau Giay, Ha Noi 100000, Vietnam*
[5]*NTT Institute of High Technology, Nguyen Tat Thanh University, 300A Nguyen Tat Thanh, District 4, Ho Chi Minh City 700000, Vietnam*

Correspondence should be addressed to Quang Tung Nguyen; quangtungdhcnhn@gmail.com
and Hoang Thai; hoangth@itt.vast.vn

Recently, plenty of interesting studies on improvement of bioavailability for poorly soluble drugs were implemented with different approaches such as using of combined biopolymers as a delivery system that allowed to enhancing drug solubility and bioavailability. In this work, alginate and chitosan were blended together in the form of polymeric particles, loaded with both lovastatin and ginsenoside Rb1 to producing the four-component nanoparticles by ionic gelation method. $CaCl_2$ and sodium tripolyphosphate were used as gelation agent and cross-linking agent, respectively. The characteristics of obtained nanoparticles were studied by means of infrared spectra (IR), scanning electron microscopy (SEM), differential scanning calorimetry (DSC), and dynamic light scattering (DLS). In combination, ginsenoside Rb1 and lovastatin both interacted with each other to improve the drug release ability of the polymer particles. The change of initial content of drugs in the nanoparticles has a negligible effect on the functional groups in the structure of the nanoparticles but has a significant impact on drug release process of both lovastatin and ginsenoside Rb1 from the nanoparticles in selective simulated body fluids. In addition, the synergistic interaction of lovastatin and ginsenoside Rb1 could be also observed through the modification of relative crystal degree and drug release efficiency.

1. Introduction

Alginate (AG) and chitosan (CS) are two common natural polymers with very diverse applications in different fields such as medical, pharmaceutical, food, beverage, and arts. AG is found in 265 generals of brown algae's [1] as an organic acid with molecular weight of 32,000-200000 which was discovered by Stanford in the late 19th century [1, 2]. AG dissolves into water and forms a highly viscosity aqueous solution that is helpful for food preservation to enlarge the storage time while keeping the quality [3–8]. Moreover, AG has also been used in paper industry [9], biomedical

applications [3, 10, 11], wound management [12–14], and fiber industry [15] for its convenient-to-use, nontoxic characteristic.

Chitosan (CS), scientific name poly(1,4)-2-amino-2-deoxy-β-D-glucose or poly(1,4)-2-amino-2-deoxy-β-D-glucopyranose, is a deacetylate derivative of chitin—the second abundant polysaccharide in nature (after cellulose). It is also the second most popular biopolymer in the world [16] with large application in food industry [17, 18], agriculture [19–21], cosmetic [18], water treatment technology [17, 18, 22], and biomedical materials and pharmaceuticals [23–25]. Especially, CS is also a pivotal material in preparation glucosamine [26, 27].

The combination of these two abovementioned materials gives remarkable enhancement in antibacterial properties both for AG bandages as well as AG fibers while coming with CS [15]. Thus, the studies on fabricating and applying AG/CS polymer blend as material for loading drugs are now an attractive research direction.

Lovastatin (Lov) is a naturally occurring fermentation compound that was discovered in 1970. It was found in red yeast rice [28] and oyster mushrooms [29]. Lov inhibits cholesterol biosynthesis, reduces cholesterol in liver cells, and stimulates synthesis of LDL (low-density lipoprotein) receptors, thereby increasing LDL transport from blood to reduce plasma cholesterol levels. Thus, the prevention of cardiovascular diseases and treatment of dyslipidemia are main applications of Lov [30]. However, Lov has an average decomposition half-time approximately 3-4 hours, so patients have to take it several times a day to maintain the minimum drug level. To overcome this limitation, Lov is loaded into polymers that have the ability to control drug release through physical interactions between polymers and drug, decreasing number of drug using times. In the work on potential nanochitosan materials carrying Lov at different concentrations of CS, Shinde has figured out that Lov is absorbed by CS and the ability of drug loading decreases while increasing CS concentration. CS materials loading with Lov had shown its effectiveness in maintaining drug release for a long time [31]. Other studies on different drug-carrier polymer systems have also shown the same advantage in controlling drug release of these polymers [32–37]. Our previous studies have been done by preparing and releasing Lov from AG/CS polymers in both film materials [38] and nanoparticles [39], in which, the size of AG/CS/Lov nanoparticles was 50-100 nm. The efficacy of Lov release control was evident in the later stages, and the Lov release process from AG/CS/Lov nanoparticles had the most suitable Korsmeyer-Peppas kinetic model with complex mechanism [39].

Panax notoginseng is a well-known folk medicinal herbal using for the treatment of hemostatic, hemoptysis, and hematoma for centuries in China, Vietnam, and other Asian countries [40–44]. Over 200 chemical compounds have been isolated from the plant, but the main constituents are Panax notoginseng saponins (PNS) [39, 45]. Two major saponins as ginsenoside Rb1 and ginsenoside Rg1 have been identified from the PNS harvested in Vietnamese (*Vietnamese Panax pseudoginseng*). While ginsenoside Rg1 has stimulating effect on nerves system, antifatigue, improves brain work, ginseno-

side Rb1 has the effect of inhibiting nerves center for sedation and deep sleep. In our previous study, a composite film combining AG/CS material and ginsenoside Rb1 had been made by solution method, and results that AG, CS, and ginsenoside Rb1 had strongly interacted to each other and created a polyelectrolyte complex [46].

In the recent work, the drug delivery polymer system of AG/CS polymer blend with 5 wt.% ginsenoside Rb1 and different Lov contents in film form was produced and studied. The results showed that Lov and ginsenoside Rb1 had a synergistic effect which affect on the morphology, properties, and drug release ability of these polymer films [45]. In preparation of AG/CS nanocomposites loading with Lov and ginsenoside Rb1 by ionic gelation method, the impact of both calcium chloride as a gel forming substance and sodium tripolyphosphate (STPP) as a cross-linking agent to the properties of blend polymer was also reported [47]; from those, the most suitable concentration of calcium chloride and STPP was found.

Unlike the 3-components of AG/CS nanocomposites loading only with either Lov or ginsenoside Rb1, the synergism between Lov and ginsenoside Rb1 and AG/CS clearly appeared in the 4-component composite while in film form. This synergistic effect improved both of the drug loading ability and the releasing efficiency, overcoming the disadvantages of the 3-component nanocomposite such as limitation of drug release only reach 80-85% [39]. That caused the large amount of used drugs to be wasted.

Combining between the excellent features of each component as well as the results of previous studies, the simultaneous load of ginsenoside Rb1 and Lov into the drug delivery polymer system of AG/CS has proved to give a better result to the drug release process from AG/CS/Lov/ginsenoside Rb1 composite in film form [45, 46].

In order to inherit and promote the before-mentioned advantages and aiming to enhance practical application, a 4-component composite system with small size has been fabricated to facilitating surface interaction between the components, leading improvement of drug loading capacity and drug release efficiency.

In this paper, novel nanoparticle biomaterial of AG/CS loading simultaneously Lov and ginsenoside Rb1 (NPB) is produced by ionic gelation method in favorable condition. The physical characteristics, morphology, drug loading efficiency, and drug release process of obtained NPB have been studied and discussed.

2. Experimental

2.1. Materials. Chitosan (CS) powder with deacetylation degree of 75%, sodium alginate powder (AG) with viscosity 300-500 mPa.s, lovastatin powder (Lov) with purity of 98.0%, and sodium tripolyphosphate (STPP) were commercial chemicals from Sigma-Aldrich. Ginsenoside Rb1 in white powder with the purity of 98% was extracted from Panax pseudoginseng and provided by National Institute of Medicinal Materials, Vietnam. Other analytical grade chemicals and solvents are ethanol, acetic acid 1%, and calcium chloride ($CaCl_2$).

2.2. Preparation of AG/CS/LOV/Ginsenoside Rb1 Nanoparticle Biomaterials (NPB) by Ionic Gelation Method.

An ionic gelation method with $CaCl_2$ gelation agent and STPP crosslinking agent has been used for the procedure of nanoscale to microscale polymer granulars. This technique is favorable because of simple preparation in aqueous solution. The gelation process was conducted basing on the polymer characteristic to establishing cross-linking bonds in the presence of ions, resulting in the formation of nanoparticles. In this method, CS has been dissolved in acetic acid solution to obtain CS cation. Afterward, the cation solution has been added slowly under continuous stirring into an AG solution containing STPP. Due to the interaction between the opposite charges, AG/CS undergoes cross-linking and gel-ionization, then precipitates to forming spherical particles. This NPB was remarkably effective to enhance health and immunity and may reduce blood cholesterol concentration and treat cardiovascular disease in patients.

2.3. Preparation of NPB with Varied Lov and Ginsenoside Rb1 Content.

The preparation process is similar to the production of 4-component AG/CS/Lov/ginsenoside Rb1 with a selected concentration of $CaCl_2$ of 0.002 M. The Lov content ranges from 0 wt.%, 10 wt.%, 15 wt.%, to 20 wt.% (in comparison to the total mass of AG and CS); AG/CS/ginsenoside Rb1 ratio is 1 : 1 : 5 wt.%, ginsenoside Rb1 content ranging from 0 to 5 wt.%. Table 1 presents the composition and label of the different NPB samples.

The calculated CS, AG, Lov, and ginsenoside Rb1 were dissolved in acetic acid 1% solution, distilled water, and ethanol 99%, respectively. An STPP solution of 0.83 g/L and $CaCl_2$ aqueous 0.002 M solution were also prepared.

After obtaining the above solution, mixing the STTP and $CaCl_2$ solutions and stirring in high speed ultrasonic equipment at 20,000 rpm to increase the dispersion of the substances.

Gradually pour Lov solution to ginsenoside Rb1 and stir with high speed ultrasonic until reaching homogeneous mixture. Next, slowly drop the obtained STTP and $CaCl_2$ solutions into the Lov and ginsenoside Rb1 mixture and keep stirring to produce the mixture of drug.

The loading process of drug into the AG/CS mixture was performed by slowly add the mixture of drug to the mixture of AG and CS solutions, with dripping rate at 3 mL/min and keep stirring on high speed ultrasonic stirrer for 30 min.

The final product was then collected after going through the two stages of solvent removal, centrifugation, and freeze-dry. The FreeZone 2.5 (Labconco, USA) was used as a freeze-dried equipment to evaporate completely the remaining solvent out of the materials. It was then minced into fine powder and stored in a cool, dry place before use.

2.4. Standard Curve of Lov and Ginsenoside Rb1 in Different pH Solutions and in Ethanol

2.4.1. Standard Curve of Lovastatin and Ginsenoside Rb1 in Buffer and in Ethanol.

The standard curve and regression coefficients of Lov and ginsenoside Rb1 in different pH solutions (pH 2 and pH 7.4) and in ethanol are established based on the data from the UV-Vis spectra. The Lov or ginsenoside Rb1 was dissolved in buffer or ethanol solution and stirred and measured the UV spectra data of each solution with different concentrations. The standard curve equations and linear regression coefficients (R^2) were then calculated, in which x and y according to the optical absorbance (A) and concentration (C) of Lov and ginsenoside Rb1 (Table 2).

The regression coefficients of the standard curve equations presented in Table 2 are about ~1, which should be used to determine the efficiency of the Lov and ginsenoside carrying as well as their content released from the NPB.

2.4.2. Determination of Lov and Ginsenoside Loading Efficiency.

As opposed to the Lov and ginsenoside loading process, their release process has been carried out by putting a certain amount of Lov or ginsenoside Rb1 loaded nanoparticle into ethanol solution and stirring well for 24 hours. An exact volume of the solution was filtered and used to determining the optical density of Lov and ginsenoside Rb1. This data was used to comparing and calculating based on the standard curves of Lov and ginsenoside Rb1 in ethanol to obtain the loading efficiency of Lov and ginsenoside Rb1 in NPB samples.

2.4.3. Evaluation of Lov and Ginsenoside Rb1 Release Process from NPB.

The experiments of Lov and ginsenoside Rb1 release from NPB were conducted in the buffer solution at pH 2 and pH 7.4. A certain amount of the drug loading nanoparticle was taken into buffer at 37°C while continuously stirred at 20,000 rpm. After every hour, a certain volume of the solution was taken to filter and recorded UV data of Lov and ginsenoside Rb1 concentration. An equivalent amount of fresh buffer solution had been added to maintain the initial volume. Similar procedure was then repeated until finishing 32 testing hours.

The amount of Lov and ginsenoside Rb1 released from NPB was calculated in corresponding to the standard curve equation of Lov and ginsenoside Rb1 in buffer solution at pH 2 and pH 7.4. With each of Lov and ginsenoside Rb1, the percentage of them released at a time (t) is calculated by the following formula:

$$\text{Percentage of released Lov or ginsenoside Rb1 (\%)} = \left(\frac{C_{(t)}}{C_{(0)}}\right) * 100,$$

(1)

where $C_{(0)}$ is the initial amount of loaded Lov or ginsenoside Rb1 and $C_{(t)}$ is the amount of Lov or ginsenoside Rb1 released at a time (t).

2.5. Morphology and Characteristics of NPB

2.5.1. FTIR Spectra.

Fourier Transform Infrared (FTIR) spectra of AG, CS, Lov, ginsenoside Rb1, and drug-loading nanoparticles were recorded on a Nicolet iS10 spectrometer (Thermo Scientific, USA) at room temperature by 32 scans with 8 cm⁻¹ resolution and wavenumber ranging from 400 to 4000 cm⁻¹.

TABLE 1: Composition and label of NPB samples.

Samples label—R_xL_y (ratio of initial content of ginsenoside Rb1 and Lov in NPB)		Lov initial content (wt.%)				
		0	5	10	15	20
Ginsenoside Rb1 initial content (wt.%)	0%			R0L10		
	1%			R1L10		
	3%			R3L10		
	5%	R5L0	R5L5	R5L10	R5L15	R5L20

TABLE 2: LOV and ginsenoside Rb1 standard curve equations in different pH solutions and in ethanol.

Drugs	Medium	Parameters of standard curve equation of drugs		
		Standard curve equation	R^2	λ_{max} (nm)
Lov	pH 2	$y = 6187x + 0.011$	0.996	229.97
	pH 7.4	$y = 3197.2x + 0.019$	0.996	239.15
	Ethanol	$y = 31269x + 0.3012$	0.993	245.55
Ginsenoside Rb1	pH 2	$y = 5400x + 0.0196$	0.996	219.52
	pH 7.4	$y = 2077x + 0.014$	0.996	219.00
	Ethanol	$y = 4513.8x + 0.002$	0.991	213.55

2.5.2. Scanning Electron Nanoscopy (SEM). SEM images of the NPB were taken on a FESEM S4800 device (Hitachi, Japan) with magnification from 1000 times to 200000 times. The samples were coated with Pt to improve the conductivity of materials.

2.6. Differential Scanning Calorimetry (DSC). Schematic DSC curves of the NPB were measured on DSC-60 (Shimadzu, Japan) with heating condition from room temperature to 400°C, heat rate at 10°C/min in gaseous nitrogen.

2.6.1. Dynamic Light Scattering (DLS). The Zetasizer SZ-100 equipment was used to determine particle size of NPB at 25°C, with measuring range from 0.1 to 10000 nm. The NPB was dispersed in distilled water before recording the size distribution diagram.

2.6.2. Ultraviolet–Visible Spectroscopy (UV-VIS). The UV-Vis spectrometer (Cintra 40, GBC, USA) was used to determine the loading efficiency and concentration of Lov, ginsenoside Rb1 released from the NPB in different pH solutions and in ethanol.

3. Results and Discussion

3.1. FTIR Spectra of NPB. The FTIR spectra of AG, CS, Lov, and ginsenoside Rb1 are presented in Figure 1. Characterized bands of functional groups in AG are listed as follows: stretching C-H bonding at 2923.65 cm^{-1}; C=O group at 1626.64 cm^{-1}; C-O-C bending vibration at 1096.95 cm^{-1} and 1032.1 cm^{-1}; and the saccharide ring vibrations at 947.86 cm^{-1}, 891.80 cm^{-1}, and 824.34 cm^{-1}. A broad band at 3448.16 cm^{-1} represents the stretching vibrations of -OH group in AG macromolecule.
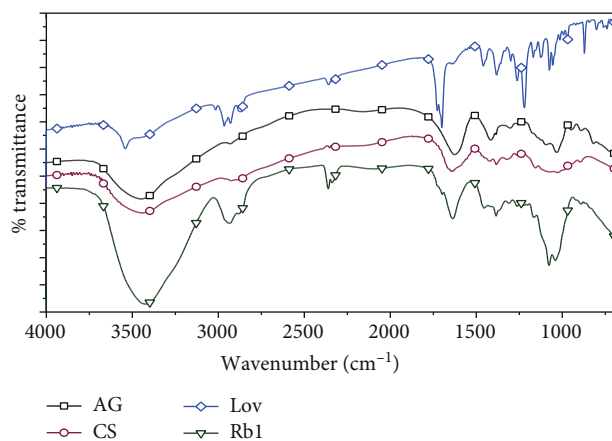
FIGURE 1: FTIR spectra of AG, CS, Lov, and ginsenoside Rb1.

In the FTIR spectrum of CS, the characteristic peaks of –CH and C-O groups are at 2883.51 cm^{-1} and 1082.75 cm^{-1}; a broad peak at 3447.62 cm^{-1} attributed to -OH and -NH$_2$ groups and amide group at 1598.29 cm^{-1} which is assigned for –NH$_2$ group; other peaks also appear at 895.17 cm^{-1} for saccharide ring vibration in CS and at 1651.26 cm^{-1} for C=O stretching.

In the FTIR spectrum of ginsenoside Rb1, the broad band at 3423.35 cm^{-1} represents for –OH stretching vibration and 2937.96 cm^{-1} and 2941.92 cm^{-1} band for CH$_2$ and CH stretching. The stretching vibration of C=C bonding appeared in 1640.73 cm^{-1} band. The absorption band at 1077.79 cm^{-1} is for C-O-C stretching and the –OH bending vibration at 1364.06 cm^{-1} band.

The IR spectrum of pure Lov has characterized groups such as –OH stretching vibration at 3640.99 cm^{-1}; the stretching vibration of C-H bonding in -CH$_3$, -CH$_2$-, and -CH- appeared in three bands at 2966 cm^{-1}, 2929 cm^{-1}, and 2867 cm^{-1}; and –C=O stretching vibration of saturated lactones at 1728.02 cm^{-1}. The absorption band at 1696 cm^{-1} characterized for the stretching vibration of C=C bonding of Lov, and the 1701.11 cm^{-1} band is due to C=O group in the Lov structure. The C-O-C stretching is at 1074.50 cm^{-1}.

The similarity has been found in the FTIR spectrum of other NPB-RxLy in comparison with the R5L10 sample (Figures 2 and 3). Thus, only the above characterized peaks of functional groups in the samples have been listed in Table 3.

The results of FTIR analysis of NPB-RxLy show that the peak position of the characterized groups in AG, CS, Lov, and ginsenoside Rb1 has shifted slightly due to the mutual

FIGURE 2: FTIR spectra of NPB-RxL10.

FIGURE 3: FTIR spectrum of NPB-R5Ly.

TABLE 3: IR band for characterized groups of AG, CS, Lov, ginsenoside Rb1, and NPB with different Lov content.

Sample	Wavenumber (cm^{-1})				
	$\nu_{NH2,OH}$	ν_{CH}	$\nu_{C=O}$	δ_{NH2}	ν_{C-O-C}
Alginat (AG)	3448.16	2923.65	1626.64	_	1096.95
Chitosan (CS)	3447.62	2883.51	_	1598.29	1081
Lovastatin (Lov)	3640.99	2966.06	1728.11	_	1077.79
Ginsenoside Rb1	3423.35	2941.92	1077.79	1451.91	1070
R5L0	3451.51	2928.31	1627.43	1414.17	1089.41
R0L10	3443.16	2928.37	1621.10	1416.30	1090.57
R3L10	3440.53	2931.39	1619.98	1415.55	1033.70
R5L10	3426.96	2931.39	1616.12	1415.55	1091.56
R5L20	3441.66	2968.62	1628.84	1535.36	1075.37

With 5% ginsenoside Rb1 (R5Ly), the rod/particle size of Lov in 4-component NPBs has been significantly reduced but still not evenly dispersed into the AG/CS polymer blend, resulting in the size of about 200 nm-1 μm observed. From Figures 5(b)–5(e), as the Lov content increases, it seems that the impact of drug-drug interaction exceeds the polymer-drug interaction, and the drug tends to agglomerate to form larger size rods/particles.

Figures 6(a) and 6(b) show the SEM image of R0L10 surface at magnifications of 10,000 times and 30,000 times. The polymer particles appeared with relatively large size and heavy rough surface; the Lov rod was 1.5 μm size and agglomerated together, much smaller in comparison with the size of pure Lov rod (Figure 4) ranging from 20 μm to 30 μm.

Figures 6(c) and 6(d) present SEM image of NPB with 1 wt.% ginsenoside Rb1 (R1L10 sample). The sizes of dispersed Lov rods are from 0.5 to 1 μm, and the particles are observed to be detached with each other. With the presence of ginsenoside Rb1, the Lov tends to have better dispersion in AG/CS polymer particles.

In Figures 6(e) and 6(f), the SEM image of R3L10 using 3 wt.% ginsenoside Rb1, the Lov rods have been covered with a polymer layer (brighter part surrounds the particles). Lov is better dispersed into AG/CS polymer blend in the size of 100-300 nm. With 5 wt.% Rb1 content (Figures 6(g) and 6(h)), the Lov rods tend to agglomerate together and form larger particles, about 200 nm-1 μm.

It is very likely that the increase in ginsenoside Rb1 content also increases the internal molecular linkage between ginsenoside Rb1 molecules, thus, leading to the aggregation of ginsenoside Rb1 particles, reducing their size stability of ginsenoside Rb1, and generating uneven structure in the NPB. Therefore, in addition to its biological activities, ginsenoside Rb1 might act as size stabilizer in NPBs through dipole-dipole interactions and hydrogen bonding [45, 46].

interaction between the characteristic groups in AG, CS, Lov, and ginsenoside Rb1 (polymer-polymer, polymer-drug, and drug-drug interactions). Following the FTIR spectra, the position of functional groups of 4 components in the NPB was a negligible change as adding or raising Lov's content while the intensity of these bands had varied. Thus, when using STPP as cross-linking agent, the band of the characterized groups in the NPB is significantly shifted; it might due to the better interaction and mixing of the components in NPB.

3.2. Morphology of NPB. FESEM images of Lov and ginsenoside Rb1 are displayed in Figure 4. Lov structure has a rod-shaped, irregular size about 20 μm–30 μm, and ginsenoside Rb1 has granular type with irregular size about 10 μm–15 μm.

In Figure 5(f), in the NPB-R0L10 sample (without Rb1), the size of the collected particles is relatively large; phase separation appeared; the Lov rod dispersed unevenly with 1.5 μm size and agglomerated into cluster, while the initial size of Lov rod is about 20-30 μm. Thus, just only loading in AG/CS, combined with a fabrication method with STPP as a cross-linking agent and high-speed ultrasonic stirring, the Lov rod sizes have been reshaped into much smaller.

3.3. Thermal Characteristics of AG, CS, Lov, Ginsenoside Rb1, and NPB. DSC diagrams of NPB with 10% Lov (R0L10) and 5% ginsenoside Rb1 (R5L0) are presented in Figure 7. Figure 8(a) presents DSC diagrams of R5Ly group with a fixed content of 5 wt.% ginsenoside Rb1. And Figure 8(b)

(a)   (b)
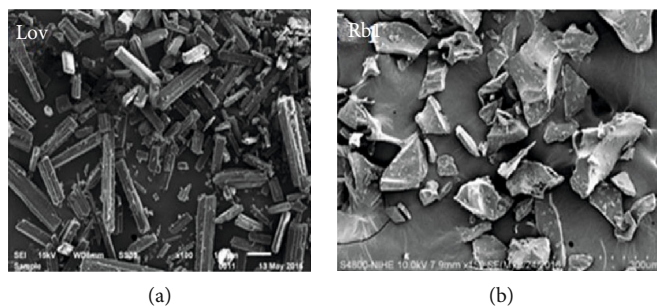
FIGURE 4: FESEM image of Lov (a) and ginsenoside Rb1 (b).

(a)   (b)   (c)

(d)   (e)   (f)
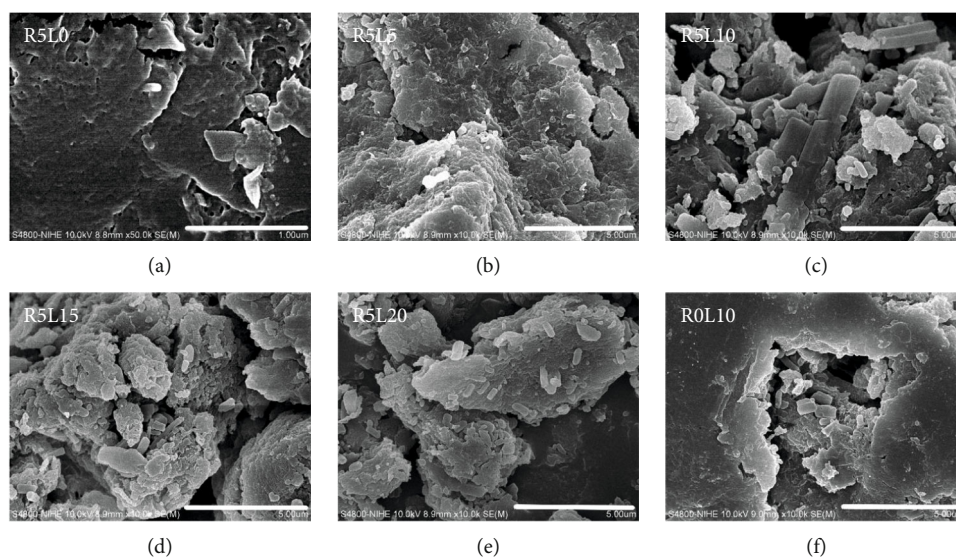
FIGURE 5: FESEM image of NPB with ginsenoside Rb1 5 wt.% and (a–e) Lov 0, 5, 10, 15, and 20 wt.% and (f) Lov 10 wt.%.

presents DSC diagrams of RxL10 NPB group with 10% Lov. The endothermic peak temperatures and exothermic peak temperatures of AG, CS, Lov, ginsenoside Rb1, and NPBs are listed in Table 4.

In Figure 7, the R5L0 sample has its two endothermic peaks at 89.51°C and 214.63°C corresponding to the dehydration and melting of AG and CS in NPB. For the R0L10 sample, two endothermic peaks located at 73.24°C and 221.74°C were also attributed to the dehydration and melting temperature of AG and CS. Moreover, one exothermic peak at 172°C can be assigned to the decomposition of STPP in the sample. Due to the forming a eutectic system between ginsenoside Rb1 or Lov, CS, and AG, the melting temperature of the NPB was decreased significantly as compared to the single component.

In the DSC diagrams of the R5Ly group (Figures 8(a) and 8(b)), the two endothermic peaks appeared because of the dehydration process at the temperature under 100°C and melting process of components in the samples at the temperature around 210°C. Other two exothermic peaks are assigned for the decomposition of STPP cross-linking agent at the temperature about 174°C and the decomposition of AG, Lov, and ginsenoside Rb1 at the temperature above 300°C. For the R5L5 sample, the positions of two endother-

mic peaks at 101.14°C and 218.65°C and one exothermic peak at 174.81°C are slightly shifted in comparison with provided DSC peaks of AG, CS, Lov, and the 3-components R5L0 and R0L10 (Table 4). This result showed that the changes of initial Lov content or ginsenoside Rb1 content have a significant effect on phase transition of the NPB samples. In this case, due to synergistic effect, all the recorded DSC peaks of 4-component NPBs are broader and more flattened (Figures 8(a) and 8(b)).

3.4. Particle Size, Zeta Potential, and Polydispersity Index of NPBs. Dynamic light scattering (DLS) method has been used to measure particle size of materials with dispersed medium of distilled water. The particle size distribution diagram of NPB-R5Ly samples is shown in Figure 9, and the average particle size of the NPB is displayed in Table 5. Most of the NPB samples have more than 2 particle size ranges; the average particle size of those samples are taken to the peak with highest intensity value.

From the collected results, the R5L5 has a smaller and more uniform particle size than others; from 190.1 to 396.1 nm with the average particle size is 270.5 ± 18.735 nm with an intensity of 100.0%. This result can be explained by the significant role of ginsenoside Rb1 which acts as a particle
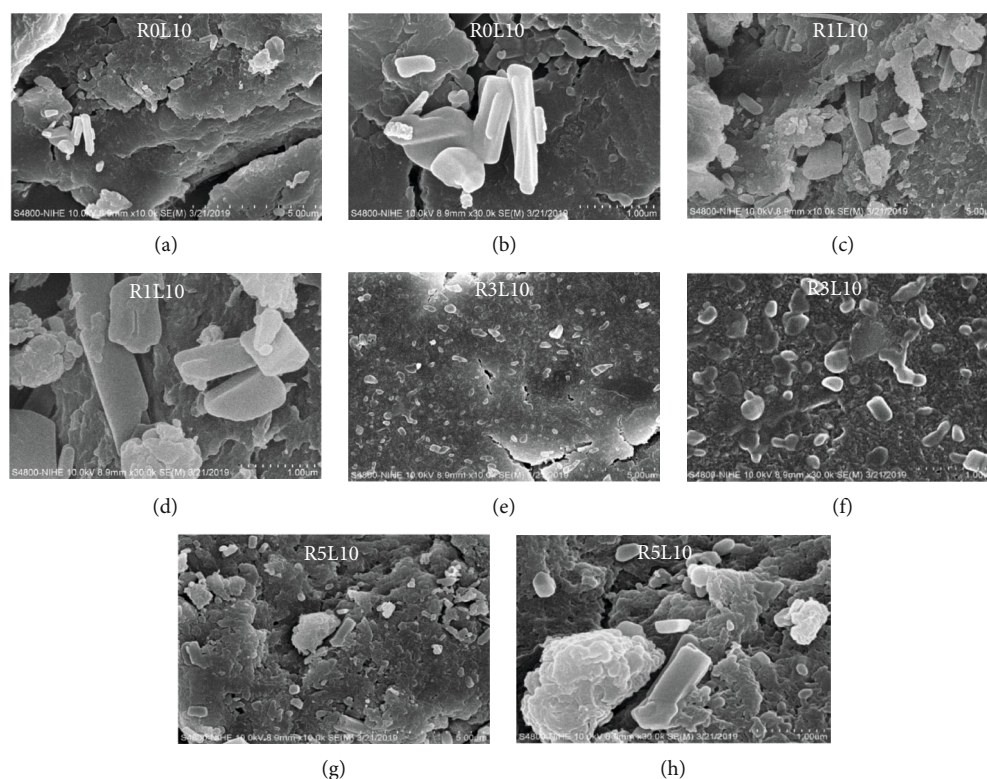
FIGURE 6: SEM image of AG/CS/Lov particles (without ginsenoside Rb1)—R0L10 sample and NPBs using 1%, 3%, and 5 wt.% ginsenoside Rb1—R1L10, R3L10, and R5L10 with magnification: ×10,000 (left) and ×30,000 (right).
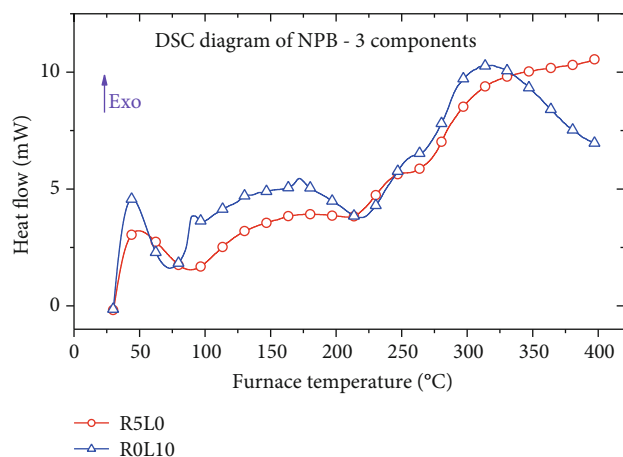
FIGURE 7: DSC diagrams of NPB of R5L0 and R0L10 samples.

size stabilizer in the NPB group. With the appropriate Lov content and the presence of Rb1, based on the interaction between ginsenoside Rb1 with AG, CS, and Lov, the Lov rods disperse more evenly into the AG/CS polymer blend.

Figure 10 and Table 5 show the result of particle size distribution diagram of the NPB group with fixed Lov content and altered ginsenoside Rb1 content. The average particle size of samples is reduced from 586.8 ± 61.85 nm of R0L10, 369.1 ± 38.46 nm of R1L10, 328.5 ± 68.45 nm of R3L10, and 333.5 ± 79.25 nm of R5L10. So, while increasing ginsenoside Rb1 content, the average particle size of NPB reduces.

In terms of NPB's particle size, in comparison between FESEM and DLS methods, these values differ between the two methods because in DLS, the particles are dispersed in distilled water; thus, obtained results are much smaller than the FESEM method.

The polydispersity index (PI) which indicates the uniformity of nanoparticles is used to evaluate the heterogeneity of a sample based on size. In accordance with ISO standards (ISO 22,412:2017), PI values < 0.5 are more common to monodisperse samples, while values > 0.7 are common to a broad size (e.g., polydisperse) distribution of particles [48]. With the low PDI value mainly ranges from 0.276 to 0.470, most of the NPBs were found to be stable and monodisperse in nature. The greater PDI values of 0.530-0.595 found in some NPB samples which have broader particle size.

In nano-drug delivery systems, zeta potential/surface charge (ZP) of polymeric particles is an important parameter; it causes major impacts on the various properties of drug delivery polymer particles, for both the stability of the nanoparticles and the rate of drug release. The high absolute value of ZP implies larger repulsive forces between particles, causing difficulty in agglomeration and thus facilitates redispersion of the particles [49]. The ZP values of R0L10, R5L0, R5L10, and R5L20 are -51.3, -23.9, -26.4, and 9.41 mV, respectively. It could be seen that the ZP value of R5L20 is lowest at 9.41 mV. The low ZP value indicates the low resultant repulsion to each other and fast aggregation that consists with the highest particle size of R5L20 sample. In case of the more agglomeration, the higher molecular weight, which

(a)

(b)
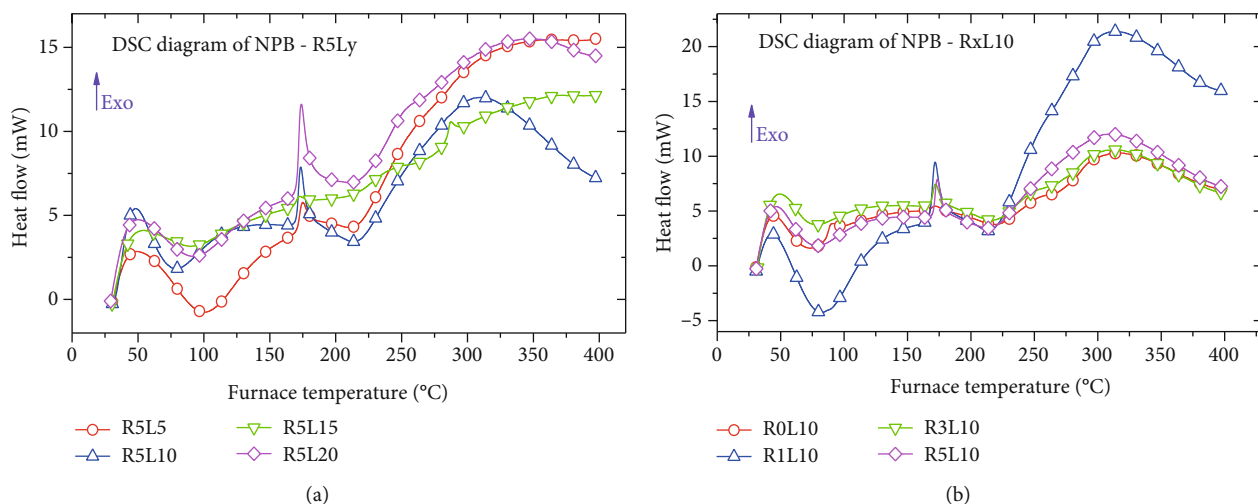
FIGURE 8: DSC diagrams of NPB with altered Lov content: R5Ly (a) and with altered ginsenoside Rb1 content RxL10 (b).

TABLE 4: Endothermic peak and exothermic peak temperatures of AG, CS, Lov, ginsenoside Rb1, and NPB using different content of Lov and ginsenoside Rb1.

Samples	1st endothermic peak temperature (°C)	1st exothermic peak temperature (°C)	2nd endothermic peak temperature (°C)
AG	119.70	238.90	—
CS	106.80	—	—
Lov	174.60	264.70	—
Rb1	98.90	230.40	—
R5L0	89.51	—	214.63
R5L5	101.14	174.81	218.65
R5L10	77.35	173.47	219.31
R5L15	91.38	172.54	219.31
R5L20	93.04	173.89	217.58
R0L10	73.24	172.14	221.74
R1L10	82.11	171.72	219.75
R3L10	76.51	172.05	219.67

FIGURE 9: Particle size distribution diagram of NPB using 5 wt.% ginsenoside Rb1 and different Lov content.

steric stabilisation will prevail, a reduction of the measured zeta potential appeared. Hence, despite the low ZP value, the stability of R5L20 is sufficient.

While absolute ZP values above 30 mV provide good stability and above 60 mV excellent stability for nanoparticles, the stability of R0L10 is excellent, and of R5L0 and R5L10 are considered as good. This might be the result of the firm rod-shape structure of Lov while appearing on the surface of the NPB, leading to the bigger size but stable of the nanoparticle; the higher Lov content, the higher the particle size.

With the presence of Rb1 in NPBs, the particle size is reduced due to the involvement of amorphous structure of Rb1 together with Lov, which could be seen while taking into account the R0L10 and R5L10 samples. ZP values of the two samples indicate the R0L10 is the most stable nanoparticle system.

3.5. Loading Efficiency of Lov and Ginsenoside Rb1 by AG/CS Polymer Blend. The loading efficiency of Lov and ginsenoside Rb1 by AG/CS polymer blend with different initial content of Lov and ginsenoside Rb1 is shown in Table 6. It could be seen that the Lov loading efficiency of the R5Ly group is a bit lower than in the RxL10 group. The highest Lov loading efficiency appeared in the R5L20 sample (78.59%). For ginsenoside Rb1 loading efficiency, the RxL10 group has a higher result of 71.22%, 76.8%, and 73.31%, respectively. From both results, the initial content of ginsenoside Rb1 in NPB has a major impact on Lov and ginsenoside Rb1 loading efficiency.

3.6. Release of Lov and Ginsenoside Rb1 from NPB Samples in Different pH Solutions

3.6.1. Influence of pH of Solution on Lov and Ginsenoside Rb1 Released Content from R5L10 Samples. Based on the calculated results of drug release percentage, Lov release process from the R5L10 in both pH 2 and pH 7.4 aqueous solutions

TABLE 5: Particle size of NPB using different Lov and ginsenoside Rb1 content.

Sample	Particle size range (nm)	Major particle size Nm (d)	%	Peak width (r) (nm)	Polydispersity index (PDI)	Average particle size (nm) $D = d \pm r/2$
R5L0	43.82-825	285	95.1	138.2	0.470	285 ± 69.1
	4145-6400	5272	4.9	426.7		5272 ± 213.35
R5L5	190.1-396.1	270.5	100.0	37.47	0.460	270.5 ± 18.735
R5L10	60–90.1	58.43	1.5	10.36	0.346	58.4 ± 5.18
	95–1050	333.5	93.6	159.5		332.5 ± 79.25
	3850-5560	5118.0	4.9	537		5118.0 ± 268.50
R5L15	43.82-190.1	76.86	7.2	14.52	0.595	76.86 ± 7.26
	190.1-1718	405.0	90.5	238.5		405 ± 119.25
	4801-6439	5560.0	2.3	0.00006		5560 ± 0.00003
R5L20	122.4-396.1	204.5	28.0	52.36	0.554	204.5 ± 26.18
	458.7-3580	1405.0	72.0	559.2		1405 ± 279.6
R0L10	480-1053	586.8	100	123.7	0.483	586.8 ± 61.85
R1L10	76-150	78.2	5.7	9.783	0.530	78.2 ± 4.89
	250-800	369.1	94.3	76.92		369.1 ± 38.46
R3L10	95-950	328.5	97.5	136.9	0.276	328.5 ± 68.45
	4000-6500	5274	2.5	424.6		5274 ± 212.3
R5L10	55-90	58.4	1.5	10.36	0.346	58.4 ± 5.18
	90-1050	333.5	93.6	158.5		333.5 ± 79.25
	4500-8500	5118	4.9	537		5118.0 ± 268.50
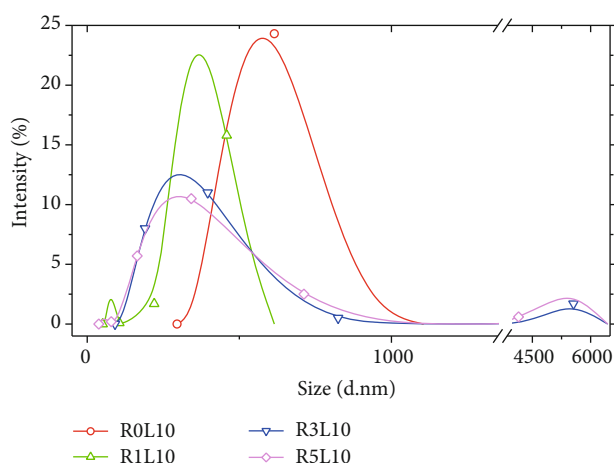
FIGURE 10: Particle size distribution diagram of NPB using 10 wt.% Lov and different ginsenoside Rb1 content.

TABLE 6: Loading efficiency of Lov and ginsenoside Rb1 by AG/CS polymer blend with different initial content of Lov and ginsenoside Rb1.

Sample	Drug loading efficiency (%)	
	LOV	Ginsenoside Rb1
R5L0	—	65.47
R5L5	39.25	64.21
R5L10	70.64	73.31
R5L15	57.63	61.35
R5L20	78.59	61.87
R0L10	62.81	
R1L10	61.38	71.22
R3L10	77.69	76.8

over experiment time has taken place in 2 stages; the release of Lov content has increased significantly during the first 10 hours (about 80 wt.%) and reached a stable value in later stage. It is reasonable because at the first stage, at the surface of NPB or closely to the surface, Lov is loaded or attached at high content; thus, it is allowed to quickly be released and strongly dispersed into testing medium. In the next stage,

Lov rods/particles are trapped deep inside the structure of the NPB and would be harder to access and diffuse outside in different pH solutions. Moreover, the external solutions are also facing more difficulty to penetrate the grain structure of the NPB due to the swelling, hydrolysis of AG and CS. The pH of the testing medium influences significantly on the Lov content released from the R5L10 sample (Figure 11). In more detail, after 32 hours, the Lov content released from the NPB in pH 2 solution is 96.99%, while in pH 7.4 solution, it reaches 99.15%. The released Lov content from NPB in
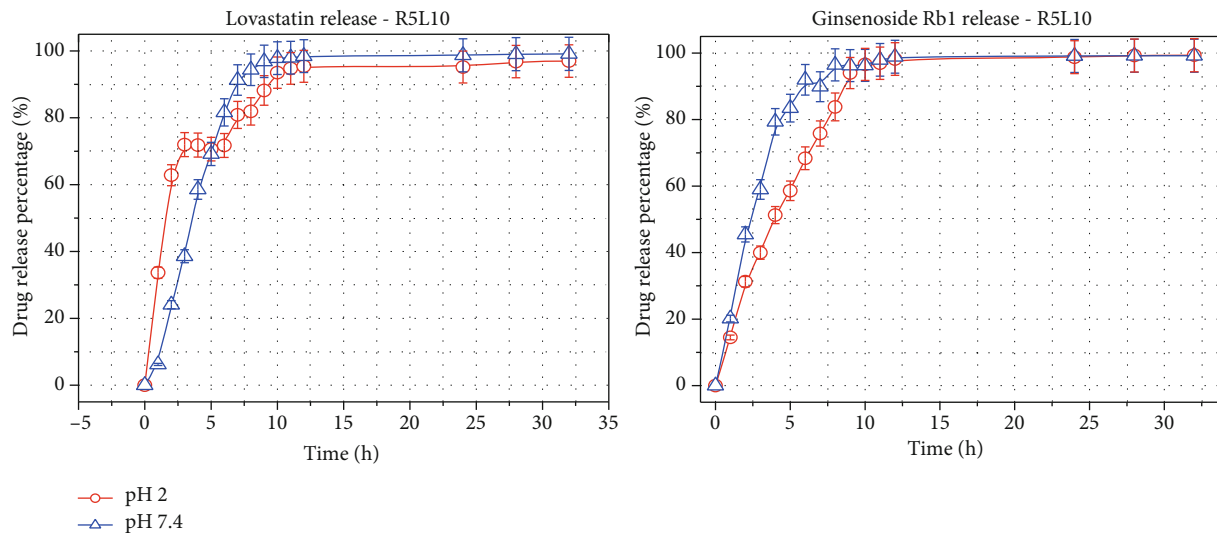
FIGURE 11: Percentage of Lov and ginsenoside Rb1 released from NPB-R5L10 sample in pH 2 and pH 7.4 solutions.
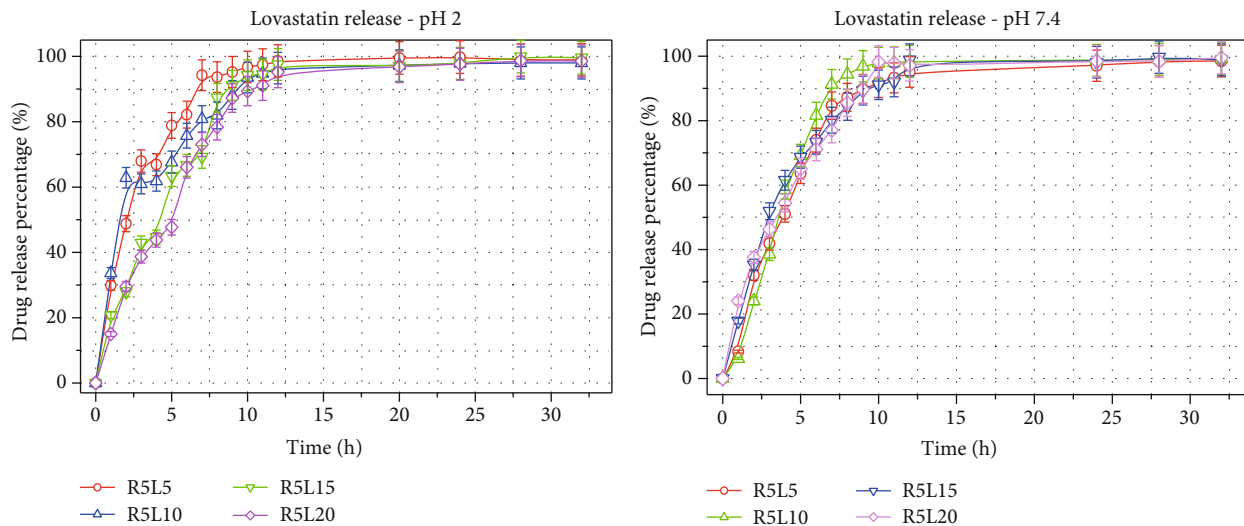
FIGURE 12: Percentage of Lov released from NPB-R5Ly samples in pH 2 and pH 7.4 solutions.

pH 2 solution is lower than in pH 7.4 solution because a portion of hydroxyl group in the released Lov reacts with H^+ ions in the acid, thus, reducing solubility of Lov in the acid solution. This is consistent with the previous findings in biomedical that Lov is poorly absorbed in the stomach, where the pH is low. Besides that, the H^+ ions also react with the amino groups of CS on the surface of the NPB, preventing Lov to diffuse into the solution [33, 34]. These results demonstrate that the drug-loading polymer particles are more suitable for the neutral environment of the large intestine and rectum mucosa than in acidic environment.

The similar tendency is observed in Figure 11 for the ginsenoside Rb1 released content from NPB. In pH 2 solution, the released content of Rb1 increases and reaches 93.60% for the first 10 hours and remains stable up to 95.36% after 32 hours. In pH 7.4 solution, this value more quickly reaches 96.30% within 8 hours and 99.19% after 32 hours, respec-

tively. In neutral environment, the released rate of Rb1 is higher and more stable than in acid environment because the H^+ ions react with the amino group of CS on the surface, reducing diffusion ability of ginsenoside Rb1 into the acid. Thus, it is possible to conclude that the pH of the environment significantly affects the released rate of Rb1.

3.6.2. Influence of Initial Lov Content on Lov Content Released from NPB Samples. Figure 12 presents the percentage of Lov released from the NPB–R5Ly samples over time in pH 2 and pH 7.4 solutions. Better Lov content released results received with lower initial Lov content among the R5Ly group for the whole experiments in pH 2 with the highest Lov released rate appeared in R5L5 and R5L10 (Figure 12). Might the small particle size help to increase the contact of NPB particles with the solution; therefore, the drug is more easily to dissolve into solutions. Moreover,
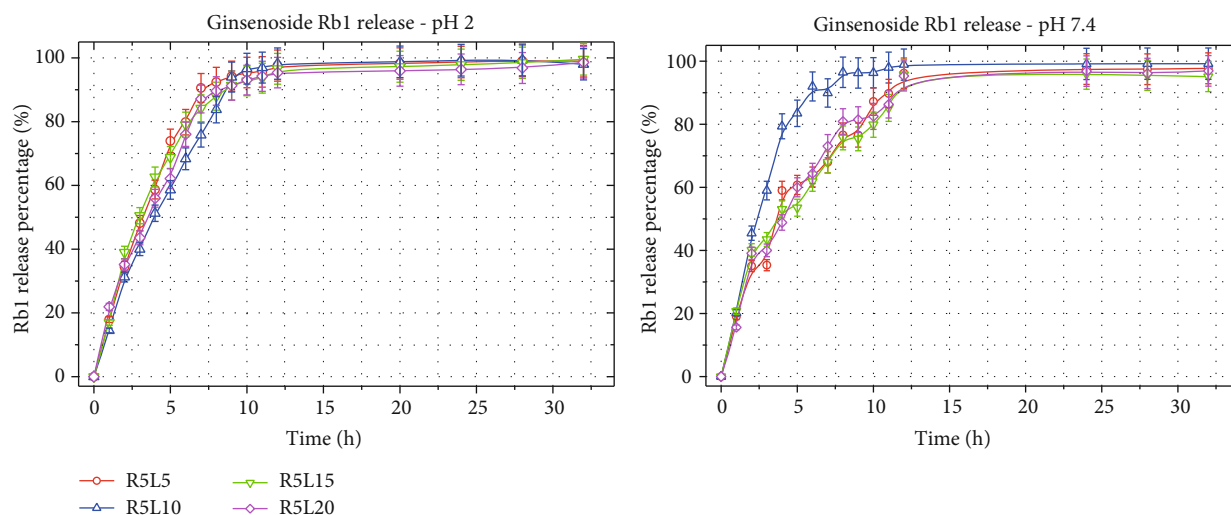
FIGURE 13: Percentage of ginsenoside Rb1 released from NPB-R5Ly samples in pH 2 and pH 7.4 solutions.

at appropriate initial content, the strong interaction between Rb1 and Lov also causes a synergistic impact in drug release rate.

In pH 7.4 solution, the released rate of Lov content is quite similar in the R5Ly group. The difference appeared mainly from 7 to 12 hours, of which, the R5L10 and R5L20 have a bit higher rate than R5L5 and R5L15. This result may be explained by burst release of drugs located on the surface and near the surface of particles at the high content of the drug in neutral environment.

3.6.3. Influence of Initial Lov Content on Ginsenoside Rb1 Content Released from NPB Samples. The dependence of initial Lov content on the percentage of ginsenoside Rb1 released from the R5Ly group over time in pH 2 and pH 7.4 solutions is shown in Figure 13.

At both pH solutions, contrary to the trend of Lov release rate, the ginsenoside Rb1 released rate is quite similar at pH 2 and much different at pH 7.4 in all of the R5Ly group. At pH 2, the R5L10 sample has the highest release rate for the first 10 testing hours compared with others; for the rest timing, it has kept a slight change from 1 to 2%, also similar to others. Thus, the ginsenoside Rb1 content released from the NPB in pH 2 solution is not significantly affected by initial Lov content. In pH 7.4 solution, the ginsenoside Rb1 released rate takes longer time to reach its maximum value (12 hours of experiment) in most of the R5Ly samples; thus, it was still highly impacted by the initial Lov content. The highest result is obtained in the R5L10 sample. This can be explained by the strong interaction of ginsenoside Rb1 and Lov with polymers which can impact the dispersed phase in polymer matrix and particle size of obtained NPB samples.

This result again reaffirms that ginsenoside Rb1 plays the role as a structural stabilizer, enhancing dispersion and mixing between AG, CS, Lov, and ginsenoside Rb1 as well as itself release ability from the NPB in pH 7.4 solution.

3.6.4. Influence of Initial Ginsenoside Rb1 Content on Lov Content Released from NPB Samples. Figure 14 describes the Lov content released rate from the RxL10 group over time in pH 2 and pH 7.4 solutions. In both cases, during the 8 first hours, Lov content released from the NPB–RxL10 samples is increased sharply (over 90%), then remains in both of the above solutions. According to the shape of the curves and the values of Lov content released rate, similarity has been found for both of pH. In both of pH, the variation of Lov content released from the NPB is quite the same over time. Hence, the change of initial ginsenoside Rb1 content has a small impact on the Lov released rate in the RxL10 group.

3.6.5. Statistical Evaluation within NPB Groups. Statistical calculation result with Student's t-test for data on Figure 12 shows that in the early stage of drug released process, within first 3 hours, the difference of released Lov content between R5Ly samples in pH 2 is highly significant different with those in pH 7.4 in comparing with the chosen level of significance $p = 0.05$, with p value ranges from 0.001 to 0.006, reaching different level at 99-99.8%. In the second stage of Lov released process, from 4 to 8 hours, the different level is decreased with higher p value ranges from 0.054 to 0.168, with the confidence level of 70-90%. For the rest period, with $p = 0.24$-0.49, Lov release percentage is quite similar within the R5Ly samples.

For the released Rb1 content (Figure 13), the R5Ly group has shown its very highly significant different level in t-student comparison from the period of 6-11 hours of experiments. During that period, the calculated p value reached 0.004–0.025, with the reliability of evaluation being in the range of 99.8-99.9%. From the first 1-5 hours, the calculated p value is in the range of 0.111–0.293, with the confidence level of 90–98%; the different level is highly significant. The rest timing of experiments is from 12 to 32 hours with $p = 0.075$-0.324, with lower but still being considered as good enough to support a conclusion of Rb1 released content between the two pHs is at significantly different levels, reaching 90-95%.
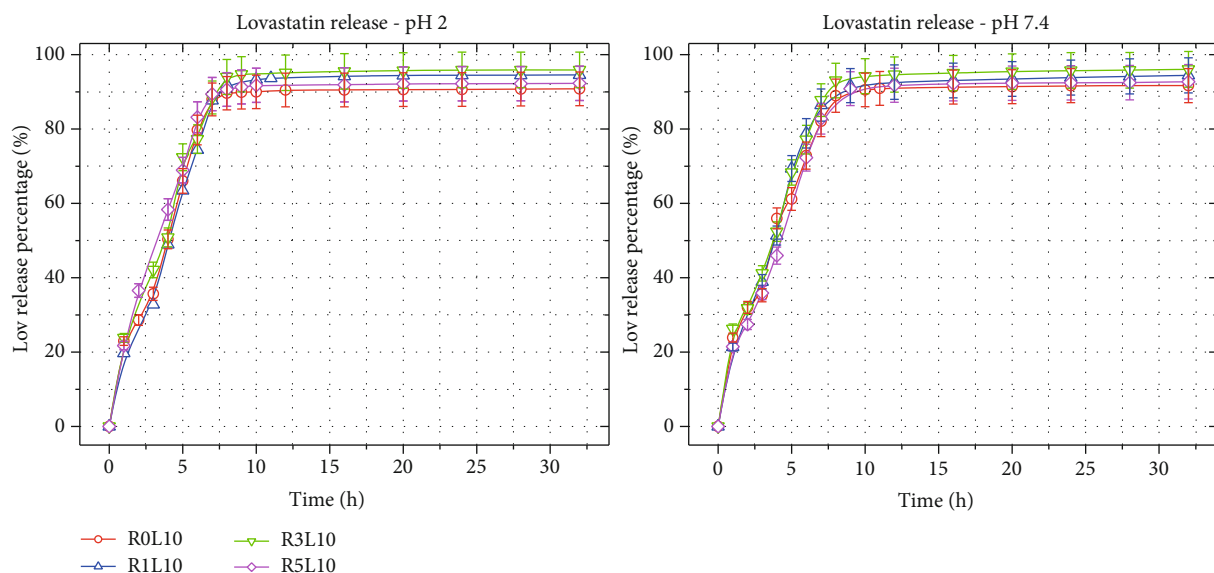
FIGURE 14: Percentage of Lov released from NPB–RxL10 samples in pH 2 and pH 7.4 solutions.

Hence, Lov released content and Rb1 released content of the R5Ly groups are not similar over the same period of experiment timing in each pH of experiments.

In overall, for every NPB sample, when adding an amount of ginsenoside Rb1 to the AG/CS/Lov particles, the Lov content released from the NPB sample is increased in both pH 2 and pH 7.4 solutions. In acidic environment, the released Lov content is lower than in neutral environment. Following the results, it could be suggested that 4-component NPB is suitable for use in the environment of intestinal and gastric fluid in human.

4. Conclusions

The novel nanoparticle biomaterials (NPB) of alginate/chitosan (AG/CS) polymer blend loading simultaneously lovastatin (Lov) and ginsenoside Rb1 were successfully fabricated by ionic gelation method using $CaCl_2$ and sodium tripolyphosphate as gelation agent and cross-linking agent, respectively. The results of FTIR analysis of NPB samples using different Lov and ginsenoside Rb1 content show that the peak position of the characterized groups in AG, CS, Lov, and ginsenoside Rb1 has shifted slightly due to the mutual interaction such as dipole-dipole interactions and hydrogen bonding between the characteristic groups in AG, CS, Lov, and ginsenoside Rb1. As a particle size stabilizer for AG/CS/Lov particles, ginsenoside Rb1 contributes to dispersing Lov rods more regularly into the AG/CS polymer blend. Among the investigated NPB samples, the NPB with AG/CS ratio of 1/1 (wt./wt.), 5 wt.% Lov and 5 wt.% ginsenoside Rb1 (R5L5) sample has a particle size in the range from 190.1 to 396.1 nm; the average particle size is 270.5 ± 18.735 nm with an intensity of 100.0%. Zeta potential values indicate the excellent stability of R0L10 and good stability of R5L0 and R5L10 which means the 4-components with 5 wt.% Rb1 and 10 wt.% Lov content is the decent stable nanoparticle system. The Lov release process from the NPB samples in both pH 2 and pH 7.4 solutions according to testing time includes 2 stages, quick release for the first testing 10 hours, then slow release to stable value. Similarly, the ginsenoside Rb1 release process from the NPB samples in both pH 2 and pH 7.4 solutions also includes 2 stages, quick release for the first testing 7 hours, then slow down to a stable value. The release of Lov and ginsenoside Rb1 content from the NPB samples in pH 2 solution is lower than in pH 7.4 solution with the same components of NPB samples and testing time.

Data Availability

Data availability statement is included in the paper content.

Conflicts of Interest

There are no conflicts to declare.

Acknowledgments

References

[1] W. Paul and C. P. Sharma, "Alginates: wound dressings," in *Encyclopedia of Biomedical Polymers and Polymeric Biomaterials*, 2015.

[2] E. C. Stanford, "Improvements in the manufacture of useful products from seaweeds," Tech. Rep. 142, British patent, 1881.

[3] K. Y. Lee and D. J. Mooney, "Alginate: properties and biomedical applications," *Progress in Polymer Science*, vol. 37, no. 1, pp. 106–126, 2012.

[4] W. Sabra and W.-D. Deckwer, *Alginate-A Polysaccharide of Industrial Interest and Diverse Biological Functions, in*

Polysaccharides—Structural Diversity and Functional Versatility, Marcel Dekker, New York, 2nd edition, 2005.

[5] Y. Pranoto, V. M. Salokhe, and S. K. Rakshit, "Physical and antibacte rial properties of alginate-based edible film incorporated with garlic oil," *Food Research International*, vol. 38, no. 3, pp. 267–272, 2005.

[6] K. Norajit and G. H. Ryu, "Preparation and properties of antibacterial alginate films incorporating extruded white ginseng extract," *Journal of Food Processing and Preservation*, vol. 35, no. 4, pp. 387–393, 2011.

[7] A. Mohammed Fayaz, "Mycobased synthesis of silver nanoparticles and their incorporation into sodium alginate films for vegetable and fruit preservation," *Journal of Agricultural and Food Chemistry*, vol. 57, no. 14, pp. 6246–6252, 2009.

[8] A. Concha-Meyer, R. Schöbitz, C. Brito, and R. Fuentes, "Lactic acid bacteria in an alginate film inhibit Listeria monocytogenes_ growth on smoked salmon," *Food Control*, vol. 22, no. 3-4, pp. 485–489, 2011.

[9] M. Joyce, R. Gilbert, and S. Khan, "Effect of Ca++ ions on the water retention of alginate in paper coatings," *Journal of Pulp and Paper Science*, vol. 22, no. 4, pp. J126–J130, 1996.

[10] A. Hambleton, F. Debeaufort, A. Bonnotte, and A. Voilley, "Influence of alginate emulsion-based films structure on its barrier properties and on the protection of microencapsulated aroma compound," *Food Hydrocolloids*, vol. 23, no. 8, pp. 2116–2124, 2009.

[11] L. P. da Costa, "Alginate in biomedical applications," in *Alginates*, p. 81, 2019.

[12] Y. Qin, "The gel swelling properties of alginate fibers and their applications in wound management," *Polymers for Advanced Technologies*, vol. 19, no. 1, pp. 6–14, 2008.

[13] T. Gilchrist and A. Martin, "Wound treatment with Sorbsan – an alginate fibre dressing," *Biomaterials*, vol. 4, no. 4, pp. 317–320, 1983.

[14] R. Fraser and T. Gilchrist, "Sorbsan calcium alginate fibre dressings in footcare," *Biomaterials*, vol. 4, no. 3, pp. 222–224, 1983.

[15] C. Knill, J. Kennedy, J. Mistry et al., "Alginate fibres modified with unhydrolysed and hydrolysed chitosans for wound dressings," *Carbohydrate Polymers*, vol. 55, no. 1, pp. 65–76, 2004.

[16] P. Yadav, H. Yadav, V. G. Shah, G. Shah, and G. Dhaka, "Biomedical biopolymers, their origin and evolution in biomedical sciences: a systematic review," *Journal of Clinical and Diagnostic Research: JCDR*, vol. 9, no. 9, pp. ZE21–ZE25, 2015.

[17] F. Shahidi, J. K. V. Arachchi, and Y.-J. Jeon, "Food applications of chitin and chitosans," *Trends in Food Science & Technology*, vol. 10, no. 2, pp. 37–51, 1999.

[18] S. Hirano, "Chitin biotechnology applications," in *Biotechnology annual review*, pp. 237–258, Elsevier, 1996.

[19] R. Yadav and M. Chauhan, "Pharmaceutical diversity of chitin and chitosan: a review," *International Journal of Pharmaceutical Sciences and Research*, vol. 2, pp. 6–11, 2017.

[20] L. Ilium, "Chitosan and its use as a pharmaceutical excipient," *Pharmaceutical Research*, vol. 15, no. 9, pp. 1326–1331, 1998.

[21] G. W. Gooday, "The ecology of chitin degradation," in *Advances in microbial ecology*, pp. 387–430, Springer, 1990.

[22] S. E. Bailey, T. J. Olin, R. M. Bricka, and D. D. Adrian, "A review of potentially low-cost sorbents for heavy metals," *Water Research*, vol. 33, no. 11, pp. 2469–2479, 1999.

[23] A. Singla and M. Chawla, "Chitosan: some pharmaceutical and biological aspects-an update," *Journal of Pharmacy and Pharmacology*, vol. 53, no. 8, pp. 1047–1067, 2001.

[24] S. Koide, "Chitin-chitosan: properties, benefits and risks," *Nutrition Research*, vol. 18, no. 6, pp. 1091–1101, 1998.

[25] V. Dodane and V. D. Vilivalam, "Pharmaceutical applications of chitosan," *Pharmaceutical Science & Technology Today*, vol. 1, no. 6, pp. 246–253, 1998.

[26] Y. Sun, J. Zhang, S. Wu, and Shujun Wang, "Preparation of D-glucosamine by hydrolysis of chitosan with chitosanase and β-D-glucosaminidase," *International Journal of Biological Macromolecules*, vol. 61, pp. 160–163, 2013.

[27] L. Dai Tran, H. V. Tran, T. T. Mai et al., "Biomedical and environmental applications of chitosan-based nanomaterials," *Journal of Chitin chitosan*, vol. 16, no. 1, p. 7, 2011.

[28] J. Liu, J. Zhang, Y. Shi, S. Grimsgaard, T. Alraek, and V. Fønnebø, "Chinese red yeast rice (Monascus purpureus) for primary hyperlipidemia: a meta-analysis of randomized controlled trials," *Chinese Medicine*, vol. 1, no. 1, p. 4, 2006.

[29] N. Gunde-Cimerman and A. Cimerman, "Pleurotus fruiting bodies contain the inhibitor of 3-hydroxy-3-methylglutaryl-coenzyme A reductase—lovastatin," *Experimental Mycology*, vol. 19, no. 1, pp. 1–6, 1995.

[30] R. V. Fugit and N. D. Resch, "Conversion of patients from simvastatin to lovastatin in an outpatient pharmacy clinic," *American Journal of Health-System Pharmacy*, vol. 57, no. 18, pp. 1703–1708, 2000.

[31] A. J. Shinde and H. N. More, "Lovastatin loaded chitosan nanoparticles: preparation, evaluation and in vitro release studies," *Research Journal of Pharmacy and Technology*, vol. 4, no. 12, pp. 1869–1876, 2011.

[32] C.-Y. Yu, X.-C. Zhang, F. Z. Zhou, X. Z. Zhang, S. X. Cheng, and R. X. Zhuo, "Sustained release of antineoplastic drugs from chitosan-reinforced alginate microparticle drug delivery systems," *International Journal of Pharmaceutics*, vol. 357, no. 1-2, pp. 15–21, 2008.

[33] N. S. Rejinold, M. Muthunarayanan, K. Muthuchelian, K. P. Chennazhi, S. V. Nair, and R. Jayakumar, "Saponin-loaded chitosan nanoparticles and their cytotoxicity to cancer cell lines in vitro," *Carbohydrate Polymers*, vol. 84, no. 1, pp. 407–416, 2011.

[34] R. Nanda, A. Sasmal, and P. Nayak, "Preparation and characterization of chitosan-polylactide composites blended with Cloisite 30B for control release of the anticancer drug paclitaxel," *Carbohydrate Polymers*, vol. 83, no. 2, pp. 988–994, 2011.

[35] P. Li, Y.-N. Dai, J. P. Zhang, A. Q. Wang, and Q. Wei, "Chitosan-alginate nanoparticles as a novel drug delivery system for nifedipine," *International journal of biomedical science: IJBS*, vol. 4, no. 3, pp. 221–228, 2008.

[36] L. Lacerda, A. L. Parize, V. Fávere, M. C. M. Laranjeira, and H. K. Stulzer, "Development and evaluation of pH-sensitive sodium alginate/chitosan microparticles containing the antituberculosis drug rifampicin," *Materials Science and Engineering: C*, vol. 39, pp. 161–167, 2014.

[37] A. García-Ceja, E. Mani-López, E. Palou, and A. López-Malo, "Viability during refrigerated storage in selected food products and during simulated gastrointestinal conditions of individual and combined lactobacilli encapsulated in alginate or alginate-chitosan," *LWT - Food Science and Technology*, vol. 63, no. 1, pp. 482–489, 2015.

[38] N. T. Chinh, N. T. Ly, T. T. Mai et al., "Characteristic and properties of chitosan/alginate polymer blend carrying lovastatin drug," *Journal of Science and Technology*, vol. 54, no. 2B, pp. 118–124, 2016.

[39] H. Thai, C. Thuy Nguyen, L. Thi Thach et al., "Characterization of chitosan/alginate/lovastatin nanoparticles and investigation of their toxic effects _in vitro_ and _in vivo_," *Scientific Reports*, vol. 10, no. 1, pp. 909–915, 2020.

[40] H. Zhang, Z. Li, Z. Zhou, H. Yang, Z. Zhong, and C. Lou, "Antidepressant-like effects of ginsenosides: a comparison of ginsenoside Rb_3 and its four deglycosylated derivatives, Rg_3, Rh_2, compound K, and 20(_S_)-protopanaxadiol in mice models of despair," *Pharmacology Biochemistry and Behavior*, vol. 140, pp. 17–26, 2016.

[41] W. Xie, X. Meng, Y. Zhai et al., "Panax notoginseng saponins: a review of its mechanisms of antidepressant or anxiolytic effects and network analysis on phytochemistry and pharmacology," *Molecules*, vol. 23, no. 4, p. 940, 2018.

[42] H. Xiang, Y. Liu, B. Zhang et al., "The antidepressant effects and mechanism of action of total saponins from the caudexes and leaves of Panax notoginseng in animal models of depression," *Phytomedicine*, vol. 18, no. 8-9, pp. 731–738, 2011.

[43] P. Su, L. Wang, S. J. du, W. F. Xin, and W. S. Zhang, "Advance in studies of Panax notoginseng saponins on pharmacological mechanism of nervous system disease," *China journal of Chinese materia medica*, vol. 39, no. 23, pp. 4516–4521, 2014.

[44] R. Bahramsoltani, M. H. Farzaei, M. S. Farahani, and R. Rahimi, "Phytochemical constituents as future antidepressants: a comprehensive review," *Reviews in the Neurosciences*, vol. 26, no. 6, pp. 699–719, 2015.

[45] H. Thai, D. L. Tran, T. L. Thach et al., "Effect of both lovastatin and ginsenoside Rb1 on some properties and in-vitro drug release of alginate/chitosan/lovastatin/ginsenoside Rb1 composite films," *Journal of Polymers and the Environment*, vol. 27, no. 12, pp. 2728–2738, 2019.

[46] T. Hoang, K. Ramadass, T. T. Loc et al., "Novel drug delivery system based on ginsenoside Rb1 loaded to chitosan/alginate nanocomposite films," *Journal of Nanoscience and Nanotechnology*, vol. 19, no. 6, pp. 3293–3300, 2019.

[47] D.-T. Nghiem, T.-C. Nguyen, M. T. Do et al., "Influence of the preparation method on some characteristics of alginate/chitosan/lovastatin composites," *Advances in Polymer Technology*, vol. 2020, Article ID 7879368, 12 pages, 2020.

[48] G. Kandav, D. Bhatt, and D. K. Jindal, "Formulation and evaluation of allopurinol loaded chitosan nanoparticles," *International Journal of Applied Pharmaceutics*, vol. 11, no. 3, pp. 49–52, 2019.

[49] S. Honary and F. Zahir, "Effect of zeta potential on the properties of nano-drug delivery systems - a review (part 1)," *Tropical Journal of Pharmaceutical Research*, vol. 12, no. 2, pp. 265–273, 2013.

Research Article

Bactericides Properties of Chitosan Metal Quantum Dots Microbial Pathogenicity Against *E. coli*, *S. aureus*, and *S. Typhi*

Galo Cárdenas-Triviño [ID],[1] **María J. Saludes-Betanzo**,[2] and **Luis Vergara-González**[2]

[1]*DIMAD, Faculty of Engineering, School of Chemical Engineering, Universidad del Bío-Bío, 1202 I. Collao Ave, Concepción, Chile*
[2]*Department of Biological Sciences and Chemistry, Faculty of Medicines and Science, Universidad San Sebastián, Las Tres Pascualas Campus, Concepción, Chile*

Correspondence should be addressed to Galo Cárdenas-Triviño; gcardenas@ubiobio.cl

The nanotechnology is considered as a tool to overcome antibiotic-resistant infections. The aim of this study was to investigate the antibacterial properties of quantum dots (QDs) of Au, Ag, and Cu supported in chitosan against *Escherichia coli* (ATCC 25922), *Staphylococcus aureus* (ATCC 29213), and *Salmonella Typhi* (ATCC 9993) strains. The QDs were synthesized by the method (Chemical Liquid Deposition, CLD) using 2-ethoxyethanol as solvent (1×10^{-3} M approximate dispersion concentration). Then, NPs supported in chitosan were synthesized by solvated metal atom dispersion (SMAD) in two concentrations, labelled [A] and [B] (0.05 and 0.1 g/L) for each metal with chitosan resulting in an average size of Au 10 ± 2.0, Ag 6 ± 1.3, and Cu 10 ± 2.4 nm, respectively. Several other techniques were performed such as TEM, SEM/EDX, TGA, DSC, and FT-IR for characterizing QDs. The antibacterial assay was performed with 8 agents on cultures of *E. coli*, *S. aureus*, and *S. Typhi* by disk diffusion, broth macrodilution, and determining death curve to the most sensitive pathogen. The antibacterial effect of the nanoparticles was compared using the diameter of growth inhibition zone by agar disk diffusion and through the minimal inhibitory concentration (MIC) and minimal bactericide concentration (MBC) obtained by macrodilution in batch culture with an initial inoculum of 5×10^5 CFU/mL. The highest bactericidal effect was obtained with nanoparticles of Au, Ag, and Cu (0.1 g/L) with MIC and MBC of 200 and 400 mg/mL, respectively. The greatest bactericidal effect considering the three pathogens turned out to be Ag QDs (0.05 and 0.1 g/L). A bactericidal effect of metal nanoparticles is affected mainly by the electronegativity, the concentration of nanoparticles, and the bacterial age culture.

1. Introduction

The biocide properties of metal nanoparticles (MNPs) have generated great interest for their application as new antimicrobial agents [1, 2]. This is due to their higher surface area which would generate more contact with the cell surface of pathogens. This feature generates a tendency to form agglomerates mainly due to Van der Waals and electrostatic forces. The importance of stabilizing the high surface energy to avoid such agglomeration with the use of an agent capable of associating with the surface of the particles is finally in their suspended stabilization and subsequent improvement of antimicrobial activity [3]. One of the protective agents used to reduce the energy on the surface of the NPs is chitosan. This is a natural polymer of high availability, biodegradability, nontoxicity, biocompatibility, and with a polycationic structure that allows to form chelates with antimicrobial activity [4]. These characteristics make chitosan, and other natural polymers, an ideal material to be used as a support for metallic nanoparticles, with antibacterial properties, for its potential use in replacement of some conventional treatments with antibiotics [5, 6]. The rise of bacterial strains with acquired antibiotics resistance in recent years had been associated with the overuse of such drugs [7], increasing the morbidity and mortality that can require a greater cost of longer treatments including hospitalization [8, 9]. Furthermore, it is unlikely that bacteria could develop resistance to the NPs compared to antibiotics, since metals

affect multiple targets in microbial cells including the cell membrane, DNA, and enzyme activity [10, 11, 12].

The aim of this study was to develop an antimicrobial agent with bactericide properties using a not conventional formulation in which the quantum dots of gold, silver, and copper supported in chitosan were used and their antibacterial activity was proved against three pathogens (*Escherichia coli*, *Staphylococcus aureus*, and *Salmonella Typhi*).

2. Experimental

2.1. Synthesis of Metal QDs (Au, Ag, and Cu) in Colloidal Suspension. The solvent 2-ethoxyethanol (Merck p.a.), nitrogen and nitrogen gas (Linde), and ultrapure metals analytical grade (Aldrich) were used. The colloids of Au, Ag, and Cu were prepared by a method called Chemical Liquid Deposition (CLD). The method involved codeposition with physical metal vapor and organic vapor under high vacuum pressure of 10^{-5} bar and temperature of 77 K in a metal atom reactor [13]. The metal quantum dots of Au, Ag, and Cu in 2-ethoxyethanol were synthesized at a concentration of 1.0×10^{-3} M (19.69 mg Au, 10.77 mg Ag, and 6.35 mg Cu in 100 mL solvent). Then, those were characterized in order to determine if this concentration will produce stable colloids. Finally, after the characterization, supported metal QDs in chitosan were synthesized by the method of solvated metal atom dispersion (SMAD). This method allows to prepare very small particles due to the solvation of a polar organic solvent and allows to incorporate them in polymer either in a solid or liquid phase.

2.2. Characterization of Metal Colloids. Metal colloids were characterized by Ultraviolet and Visible Spectroscopy (UV-VIS) and transmission electron microscopy (TEM) with X-ray diffraction (XRD). The absorption spectra of UV-Visible NPs of colloidal solutions were measured by the selection of wavelengths from 200 to 500 nm at $25 \pm 2°C$ using a Shimadzu UV-spectrometer Corp, Kyoto Japan. The colloidal dispersions were diluted about 0.1 mL dispersion in 3 mL of 2-ethoxyethanol solvent, prior to analysis to avoid excessive concentration of colloidal particles and higher absorption. For transmission electron microscopy, a drop of colloidal dispersions was placed with their respective solvent and dried on a copper grid of 150 mesh carbon-coated. The transmission micrographs were obtained using a JEM JEOL1200 EX microscope operated with an accelerating voltage of 120 keV; this equipment reaches a resolution of 4 Å. Then, the equipment operates in X-ray diffraction (XRD) to determine the chemical species of nanoparticles. To obtain the size of the quantum dots, these will be determined by optical measurements (digital measurements in pixels), where specific particle diameters were measured at random by the Mac Biophotonics software Image J. Finally, the data obtained are plotted in the form of a frequency histogram with Gaussian distribution.

2.3. Synthesis of Metal Nanoparticles Supported in Chitosan. Chitosan (Qs) with 95% deacetylation degree and molecular weight 350.000 Da provided by Quitoquímica Co. (Coronel,

Bío-Bío Region, Chile), 2-ethoxyethanol (Merck p.a.), liquid nitrogen, ultrapure nitrogen gas (Aga), and metals of analytical grade (Sigma-Aldrich). The QDs (Au, Ag, and Cu) supported on chitosan were synthesized by the method of solvated metal atom dispersion (SMAD). In the synthesis, the solvent is responsible to open the polymer chains of chitosan and allowed the inclusion of quantum dots [14].

The SMAD method involves the physical codeposition vapor of metal-organic vapors (2-ethoxyethanol) in the same physical conditions of the CLD method, but with the introduction of chitosan in the reactor [15]. Also, ethanol was used, basically both for their higher dielectric constant to help colloidal stabilization. The solvent is recovered after each reaction.

Two different concentrations of metal quantum dots (MQDs) were synthesized labeled as [A], which has a concentration of 5 mg in 100 mL of solvent and 2 g of chitosan (0.05 g/L 2gQs), and [B] 10 mg in 100 mL of solvent and 2 g of chitosan (0.10 g/L 2 g Qs). In terms of molarity, labeling [A] for QDs is as follows: Au 2.53×10^{-4} M, Ag 4.64×10^{-4} M, and Cu 7.87×10^{-4} M supported in 2 g of chitosan. The concentration [B] for QDs is as follows: Au 8.5×10^{-4} M, Ag 9.27×10^{-4} M, and Cu 15.7×10^{-4} M equally supported.

Since the concentrations in terms of molarity are different, we carried out a synthesis of Ag QDs of 7.87×10^{-4} M in order to obtain a molar equivalence with Cu QDs, Cu [A]-Qs and analyzed the influence on bacterial susceptibility test. Doped chitosan with QDs and chitosan alone were suspended at 1% (w/v) in 1% acetic acid and stored in the freezer at 4°C in amber vials for the subsequent susceptibility test. The MW of chitosan remains the same after the reaction. There are other methods recently published to obtain nanoparticles [16, 17].

2.4. Characterization of Metal Nanoparticles Supported in Chitosan. The NPs supported on chitosan were characterized by measuring using the scanning electron microscopy (SEM) with X-ray spectroscopy (EDX), thermogravimetric analysis (TGA), differential scanning calorimetry (DSC), and Fourier transform infrared spectroscopy (FTIR). Transmission electron micrographs were obtained, placing a drop of colloidal dispersion on a grid, let it dry, and then coated with gold atoms for 3 min with a thickness of 150 Å. Then, the sample is dried to finally be observed under the microscope JSM 6380LV-JEOL Scanning Electron Microscope with 20 kV acceleration voltage. The TGA analysis for NPs supported was performed taking place in a thermogravimetric analyzer Q-1000 Thermo. The mass of the sample is generally in the range of 7.0 ± 2 mg. Samples were taken to a balance system equipped, and the temperature was increased from 25°C to 550°C at a heating rate of 10°C/min under a nitrogen gas atmosphere. To obtain the thermograms, the mass of the sample is continuously recorded as a function of temperature. The DSC analysis for QDs supported took place in a METTLER TOLEDO DSC analyzer, equipped with the STAR MODEL 822 software system. The mass of the sample was in a range of 7.0 ± 2 mg and a heating rate of 10°C/min under a nitrogen gas flow. The Fourier transform infrared (FTIR) spectra were performed on a Nicolet

TABLE 1: Equivalence of mix Qs-QDs tested with NPs (mg) present in each tube.

Concentration	QDs	1600 ppm	800 ppm	400 ppm	200 ppm	100 ppm
A	Au	40	20	10	5	2.5
A	Ag	40	20	10	5	2.5
A	Cu	40	20	10	5	2.5
B	Au	80	40	20	10	5
B	Ag	80	40	20	10	5
B	Cu	80	40	20	10	5

[A] =5 mg/100 ml solvent (2 g chitosan); [B] =10 mg/100 ml (2 g chitosan).

Magna 5PC spectrophotometer, and KBr pellets 2% concentration were prepared using the Omnic 5.2a program at room temperature.

2.5. Ultraviolet and Visible Spectroscopy.
UV-VIS absorption spectra of the colloidal quantum dots in solutions were measured by wavelength selection, from 200 to 500 nm at 25°C, using a UV–Shimadzu Corp spectrometer, Kyoto, Japan. The baseline with the same solvent for the reaction was used, and each QDs (gold, silver, and copper) was examined at different times, to perform the study of the effect of sedimentation or flocculation and how the size of the colloids influences it. Colloidal solutions were diluted at approximately 0.1 mL of dispersion in 3 mL of pure solvent prior to analysis to avoid excessive agglomeration of colloidal particles and their high absorption.

2.6. Thermogravimetric Analysis.
TGA analyses for supported NPs are performed on a *Thermo Q-1000* thermogravimetric analyzer. The mass of the NPs is 7.0 ± 2 mg where they are carried to a balance system equipped with a heating temperature system that increases from 25 to 550°C with a heating rate of 10°C/min in gas nitrogen flow. To obtain the thermograms, the mass of the sample is continuously recorded according to the temperature.

2.7. Antimicrobial Activity Analysis.
Escherichia coli (ATCC 25922), *Staphylococcus aureus* (ATCC 29213), and *Salmonella Typhi* (ATCC 9993) strain were used, and a stock of them was maintained at -20°C in San Sebastian University laboratory. All assay was performed in Mueller-Hinton (Merck) broth or agar and was prepared according to the manufacturer's instructions and stored at 4°C.

Three different assays were performed to determine the antimicrobial properties of chitosan-supported NPs.

2.7.1. Disk Diffusion Test.
The disc diffusion test was performed to determine the sensitivity of bacterial strains to chitosan alone and gold, silver, and copper NPs supported in chitosan (Au-Qs, Ag-Qs, and Cu-Qs). The assay was performed according to (CLSI) [18] guidelines using disk (6.3 mm diameter) impregnated with 20 μL of each solution to be tested.

2.7.2. Serial Macrodilution Method.
One of the methods used to determine the minimal inhibitory concentration (MIC) is the broth dilution method [18]. This is based on the decreasing concentrations of an agent with antibacterial properties, acting on a standard inoculum of the microorganism. To achieve the macrodilution test in broth, an inoculum is initially prepared approximately at 10^6 CFU/mL. Then, a series of tubes were set up with a solution of each agent to study from 0.010% to 0.16% w/v (100 to 1600 ppm) suspended in 1% acetic acid plus 2 mL of inoculum previously prepared around 1.0×10^6 CFU/mL to finally produce an inoculum of 5×10^5 CFU/mL and allowed to incubate at 37 ± 2°C for 18-24 hours. The equivalence to QDs is shown in Table 1. The tube with a higher concentration that did not show growth, indicates the MIC. From each tube with no growth, a sample of 0.1 mL was obtained and streak onto a Mueller-Hinton agar plate and incubated 18-24 hours at 37 ± 2°C. The higher dilution that did not shown growth of colonies in the plates was considered the MBC (minimal bactericidal concentration).

2.8. Death Curve Determination for E. coli by Direct Plate Counting Method.
For death curve assessment, 10 mL of inoculum adjusted to 0.5 McFarland was added to 90 mL of fresh Mueller-Hinton medium to generate a final inoculum of 1×10^7 CFU/mL. A final concentration of 400 mg/mL of chitosan doped with gold ($B = 8.5 \times 10^{-4}$ M) and copper ($B = 15.7 \times 10^{-4}$ M) was used (Au [B]-Qs and Cu [B]-Qs); a positive control was prepared in the same way that of the samples but without chitosan/quantum-dots. All tests were done in duplicate. The flasks were incubated at 37°C and 150 rpm. Every two hours, the samples were taken to perform the count of viable cells. For that, 1 ml of each flask was added to 9 ml of sterile distilled water and made serial dilutions 4 times to obtain 10^6, 10^5, 10^4, and 10^3 CFU/mL of the original inoculum. From each dilution, 0.1 ml was spread onto a Mueller-Hinton agar plate and incubated overnight at 37°C. Colony counts were done using a Suntex 570 colony counter. The viable bacterial counts were plotted against the exposure time of *E. coli* to antibacterial agents and compared with positive control.

3. Results

3.1. Characterization of Metal Quantum Dots of Au, Ag, and Cu in Colloidal Suspensions.
The results determine that by the CLD method using 2-ethoxyethanol, it is possible to obtain Au, Ag, and Cu QDs with 10 ± 2.0 nm, 6 ± 1.3 nm, and 10 ± 2.4 nm, respectively; to simplify, we round the values obtained from the micrographs (Au 9.64 ± 2.00, Ag 5.50 ± 1.30, and Cu 10.0 ± 2.39 nm). Also, the prevalence of

spheroidal shape QDs of the three metals was observed. This can be correlated with the results of UV-VIS spectroscopy, summarized in Table 2. The spectra obtained for each run showed a single symmetrical band of surface plasmon resonance, reaching for Au QDs in a wavelength range of 235-505, then 383 for Ag and 210-305 nm for Cu, respectively.

Figure 1 shows the TEM images, with their respective histogram for a total of 100 QDs. For Au, Ag and Cu QDs solvated in 2-ethoxyethanol, Figure 2 shows the diffraction pattern.

Using the ED pattern (Figure 2), it was possible to confirm the crystalline nature through Miller's indices and the presence of the Au, Ag, and Cu quantum dots at the nanometric level. Interplanar distances are from diffraction rings and can be indexed according to the cubic structure centered on the faces (fcc) of the metals. The Au's QDs represent a mixture of cubooctahedral and icosahedral systems; Ag's QDs a mixture of tetragonal, hexagonal, cubic, and trigonal; and Cu's QDs a cubic and trigonal system.

3.2. Characterization of Metal Nanoparticles of Au, Ag, and Cu Supported in Chitosan.

Through scanning electron microscopy (SEM), differences were observed in the morphology of the different composites obtained from the synthesized colloids, being the chitosan-Ag the smoother surface. Furthermore, EDX confirms the presence of the metal on the surface.

The elemental analysis of each composite through dispersive X-ray spectroscopy (SEM/EDX) provides the Au quantum dots [B] are those with the lowest atomic percentage (0.06%) in the polymer surface compared to Ag and CuNPs. This explains that the AuQDs are mostly absorbed by the polymer, CuQDs [B], that have the highest metal percentage (1.59%) which leads to greater instability and tendency to agglomeration and oxidation. The results can be complemented with those obtained by X-ray diffraction (XRD) of the CuQDs. Obtaining absolute certainty of the composition of metals in the polymer requires elemental analysis by atomic absorption.

Figure 3 shows the SEM micrograph and EDX analysis of quantum dots supported on chitosan concentration [B]. TGA tests were performed for all blends metal polymer and the polymer itself.

Table 3 summarizes the results of the percentage of mass and atomic percentage of the QDs of Au, Ag, and Cu in concentration [B], read in the graphs obtained in Figure 3.

3.3. UV-Vis.

The optical absorption spectra of metallic QDs are referred to by surface plate resonances [20]. These resonances are located at larger wavelengths as the particle size increases. Figure 4 shows the result of the UV-VIS analysis NPs after their synthesis (30 min) and 3 months later. Only a slight difference in the spectrum between the two is observed, indicating the high stability of the QDs over time.

3.4. Thermogravimetric and Scanning Calorimetry Analysis.

Thermogravimetry analyses were performed for all polymer-

Table 2: UV-Vis spectrum of the Au, Ag, and Cu solvated in 2-ethoxyethanol.

Metal	Experimental band (nm)	Theoretic band (nm) [19]
Au	235-505	250-510
Ag	383	392
Cu	210-305	205-310

metal mixtures and for the polymer itself. Figure 5 shows the TGA of chitosan, showing the respective temperature of the maximum rate of decomposition and the behavior of the polymer when it is heated above 100°C. There is a slight weight loss around 100°C, which is attributed to the evaporation of water, whose content is about 3 to 5%. The bottom line shows a sharp decrease around 200°C, which ends up with the loss of almost the entire sample.

The results of the thermogravimetric method show that the thermal degradation of the MQDs supported on chitosan has a decomposition temperature (DT) lower than the pure polymer. This is because the metal QDs act as an impurity lowering the temperature of decomposition of the latter, which increases the entropy to be a composite. But in the metals with higher oxidation potentials such as Ag and Cu, the Td decreases with the amount of metal QDs. See Figures 6, 7, and 8.

However, this difference between the pure chitosan and chitosan doped with NPs is low and is within the range of 3°C, so the NPs did disrupt the inherent physical properties of chitosan itself.

With respect to the DSC results, Table 4 summarizes all the kinetic parameters for the thermal degradation of chitosan and chitosan doped with MQDs. The DSC either exo or endo shows values lower than pure chitosan; those results confirm the influence as impurities of the nanoparticles.

3.5. Fourier Transformed Infrared Spectroscopy.

FT-IR analyses for solvent, chitosan, and metal NPs supported in Qs are shown in Figure 9. Absorption spectra are analyzed in the midrange and far range through the *peaks* obtained.

Table 5 presents the allocations of the *peaks* of the solvent, chitosan, and NPs Au, Ag, and Cu in their two concentrations ([A] and [B]).

The FT-IR analysis for the solvent, chitosan, and MQDs supported was carried out in the middle and far range spectra. The analysis can clarify that for midrange spectra, only show typical absorptions of chitosan does not appear any new absorption band of the polymer with the QDs. The analysis can clarify that for midrange spectra, only typical absorptions of chitosan are shown and any new absorption band of the polymer with the QDs does not appear. Evidence shows the interaction between the amino groups of the Qs and the atoms of the surface of MQDs. Also seen in this spectrum are the new bands near 150 cm^{-1} which can be assigned to metal-metal interaction (MM) of the quantum dots.

3.6. Antimicrobial Activity Analyses

3.6.1. Agar Diffusion Method.

As expected, the best activity was seen in all assay with a higher concentration of QDs

(a)

(b)

(c)
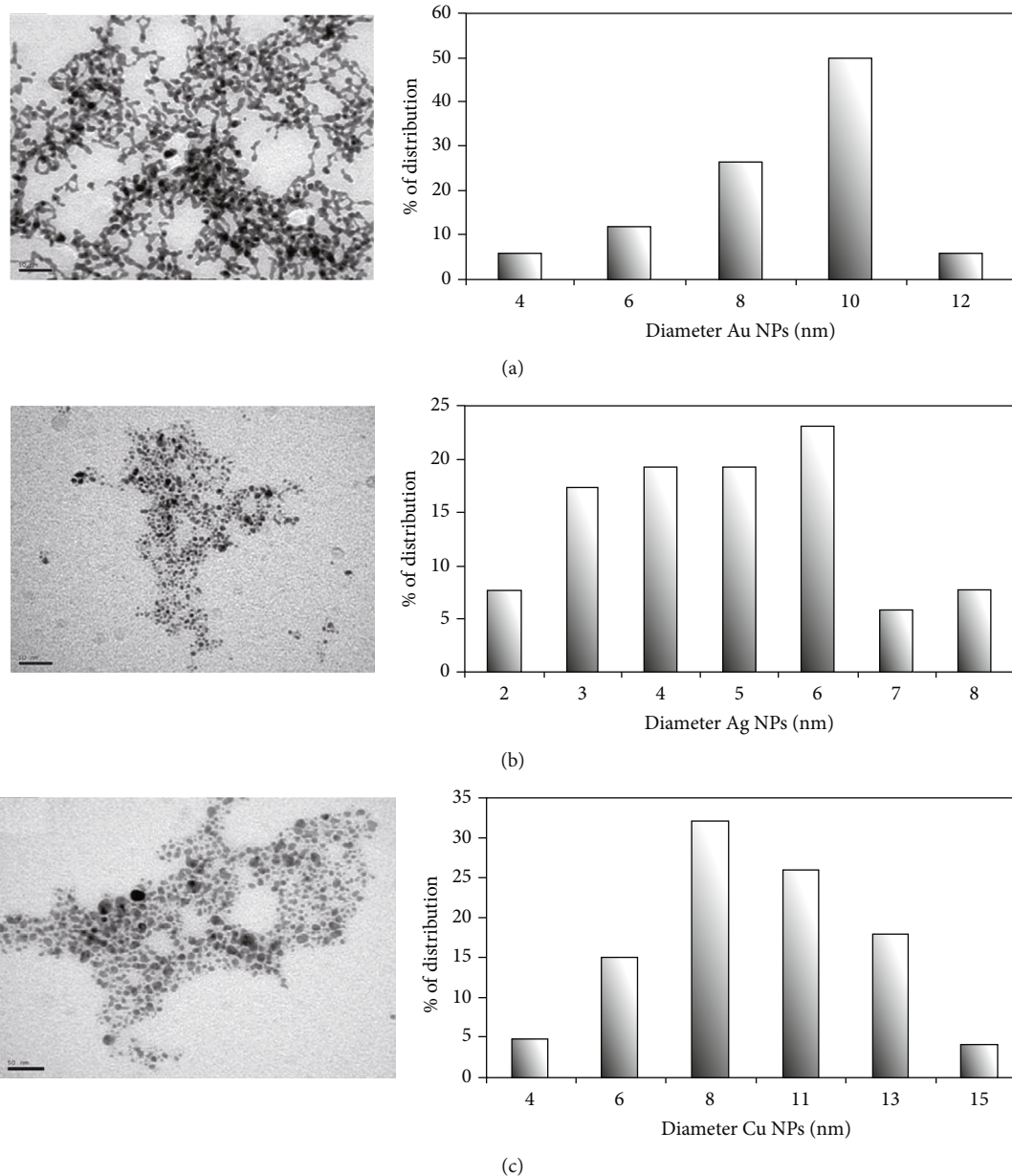
Figure 1: TEM micrograph and histogram of the size of NPs of (a) gold, (b) silver, and (c) of copper in 2-ethoxyethanol. The histograms show the distribution of the diameter measurement of solvated metal NPs in 2-ethoxyethanol. The quantum dot size is as follows: Au 10 ± 2.00 nm, Ag 6 ± 1.3 nm, and Cu 10 ± 2.39 nm.

(a)

(b)

(c)
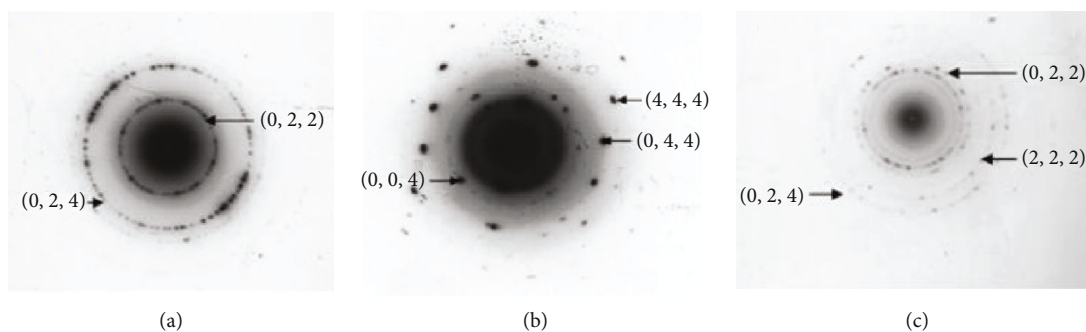
Figure 2: Diffraction pattern of solvated metal quantum dots in 2-ethoxyethanol: (a) gold, (b) silver, and (c) copper.

(a)

(b)

(c)
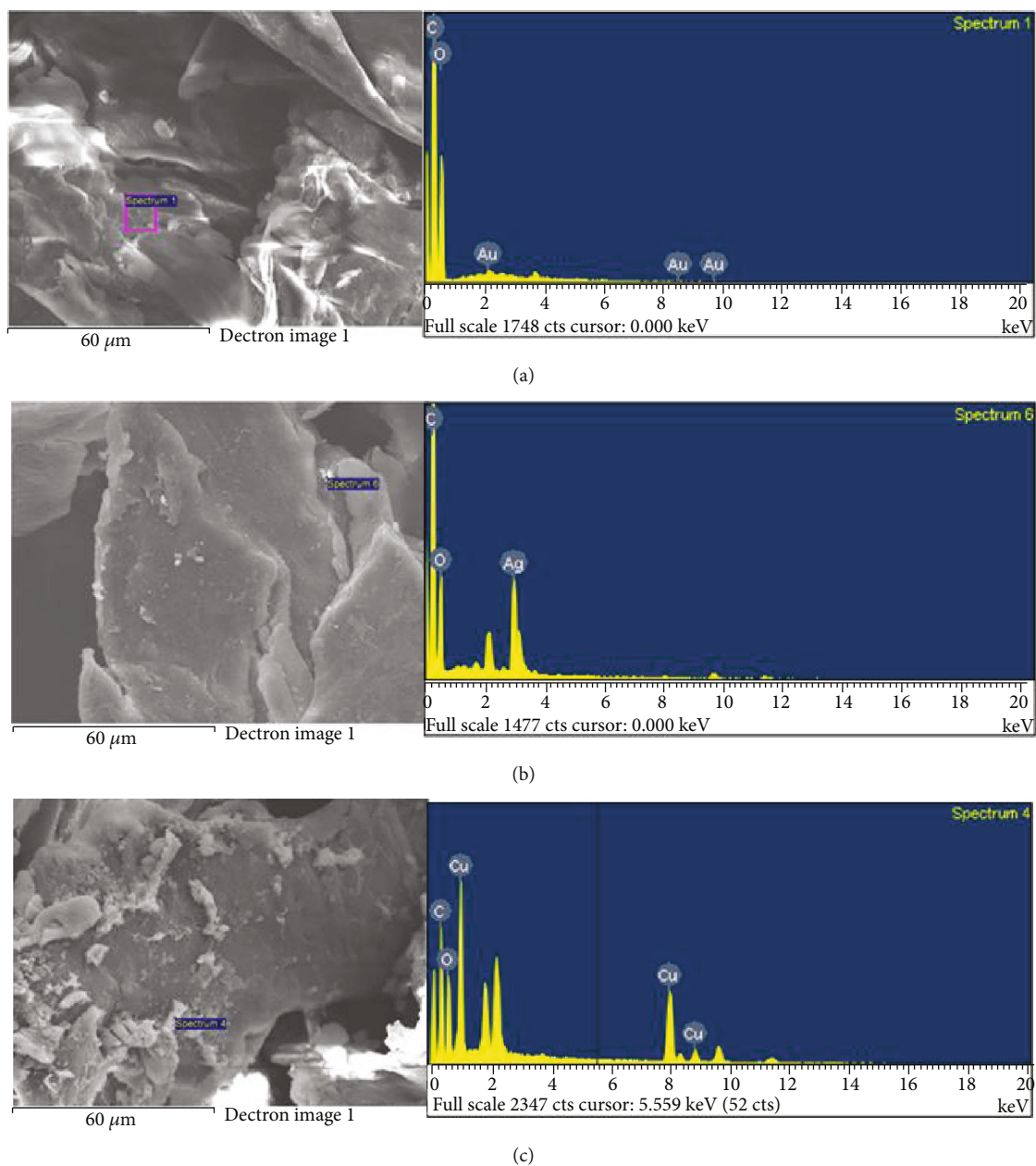
FIGURE 3: SEM and EDX elemental analysis of gold (a) silver (b) and copper (c) nanoparticles at a concentration of 0.1 g/L supported on chitosan.

([B]). As shown in Figure 10, a trend of increased susceptibility was found to *E. coli* especially to Au QDs.

However, for *S. aureus*, a best or similar activity was shown using the lowest concentration [A] with all QDs. Antibacterial activity was seen too in not doped chitosan against the three tested bacterial strains.

3.6.2. Serial Macrodilution. Table 6 presents the results of MIC and MBC obtained in each composite studied. As shown, no correlation between QD concentration and CMI-CBM was observed in all cases. For example, *E. coli* present the same MIC to AgQDs although [A] concentration is half of [B] concentration. The same occurs with other microorganisms

and metal suggesting that metal concentration is not the only variable that influences the antibacterial activity.

3.6.3. Dead Curve of E. coli. Figure 11 describes the death curve of *E. coli* in the presence of gold and copper quantum dots at a concentration of 0.1 g/L in 2 g of chitosan (concentration [B]). The results show that *E. coli* is more sensitive to copper QDs, producing the best bactericidal effect after 16 h of incubation with a reduction of 5 logs (3.3×10^7 to 3.7×10^2 CFU/mL). Conversely, the gold nanoparticles have the major antimicrobial effect after 7 hours of incubation with a slight reduction of 1 log (3.3×10^7 to 1.52×10^6 CFU/mL).

TABLE 3: Percentage of mass and atomic of elemental analysis by EDX of QDs of (a) gold, (b) silver, and (c) copper in the concentration of 0.1 g/L.

(a)

Element	% weight	% atomic
C	55.2	62.5
O	44.0	37.4
Au	0.83	0.006
Total	100	—

(b)

Element	% weight	% atomic
C	69.1	76.3
O	28.2	23.4
Ag	2.76	0.34
Total	100	—

(c)

Element	% weight	% atomic
C	59.89	69.7
O	32.87	28.7
Cu	7.24	1.59
Total	100	—

4. Discussion

The size of nanoparticles synthesized ranged between 5 to 10 nm, and for that, we call them quantum dots [21, 22]. According to Shah et al. [10], silver QDs exhibit the antimicrobial effect in very low concentration due to a large active surface area and high surface charge density, compared to silver metal.

With regard to the ED of Au, QDs generally represent a cube octahedral and icosahedral structure and the NPs of Ag and Cu, a mixture of rectangular and cubic structures. When considering the error rate, greater certainty is found in the crystalline nature of the Au and Ag QDs, since there is greater sharpness in the diffraction rings (Figures 2(a) and 2(b)) with respect to Cu's QDs (Figure 2(c)), so Ag's QDs would be the ones with the highest cubic crystallinity, followed by Cu's, while those of Au are entirely icosahedral which could influence the difference in bactericidal activity of QDs against *E. coli* and *S. aureus* cultures. The Au QDs having an icosahedral structure have a greater area of contact with the cell wall because this structure has 20 faces compared to the Ag and Cu QDs, which have cubic structure (smaller area). This would lead Au QDs to a greater interaction between the metal structure and the phosphate groups present on the cell surface, or the DNA present in the cell, which would generate a greater biocidal effect on these two pathogens.

When considering the three pathogens in the variance analysis, Ag QDs ([A] and [B]) turn out to be the most
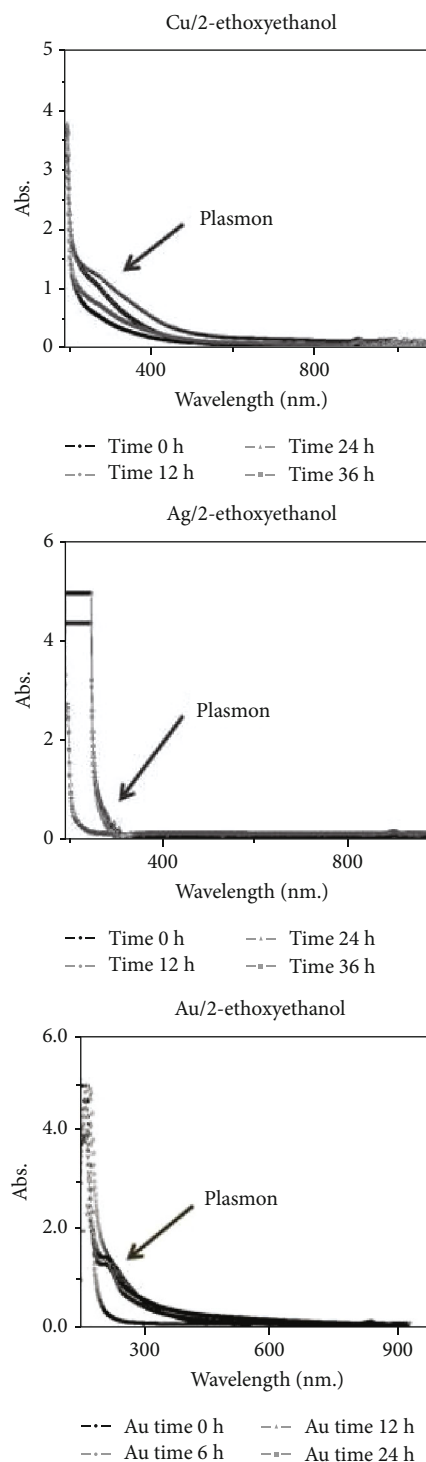
FIGURE 4: Cu, Ag, and Au QDs UV-VIS analysis in 2-ethoxyethanol solvent.

biocidal effect on these two pathogens, so more than the crystalline structure of the QDs and electronegativity [23]. It seems that the size of these is what would most influence the biocidal activity because it was shown that Ag has a diameter (6.0 ± 1.3 nm) approximately twice smaller than Au and Cu (10.0 ± 2.0 nm and 10.0 ± 2.3 nm, respectively).
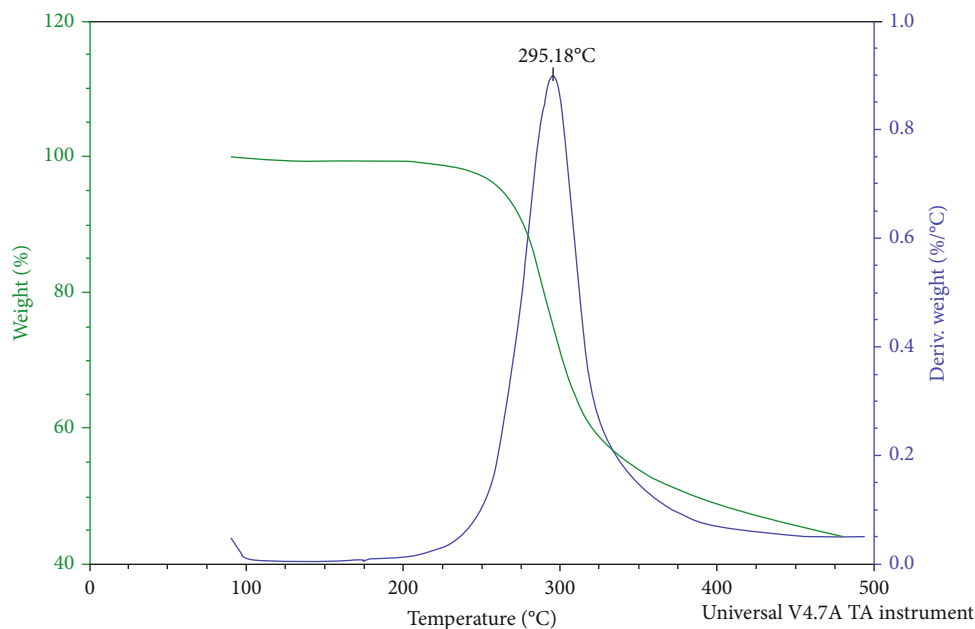
FIGURE 5: TGA of chitosan shows the decomposition temperature (295.18°C) obtained at a heating rate of 10°C/min in nitrogen gas flow.
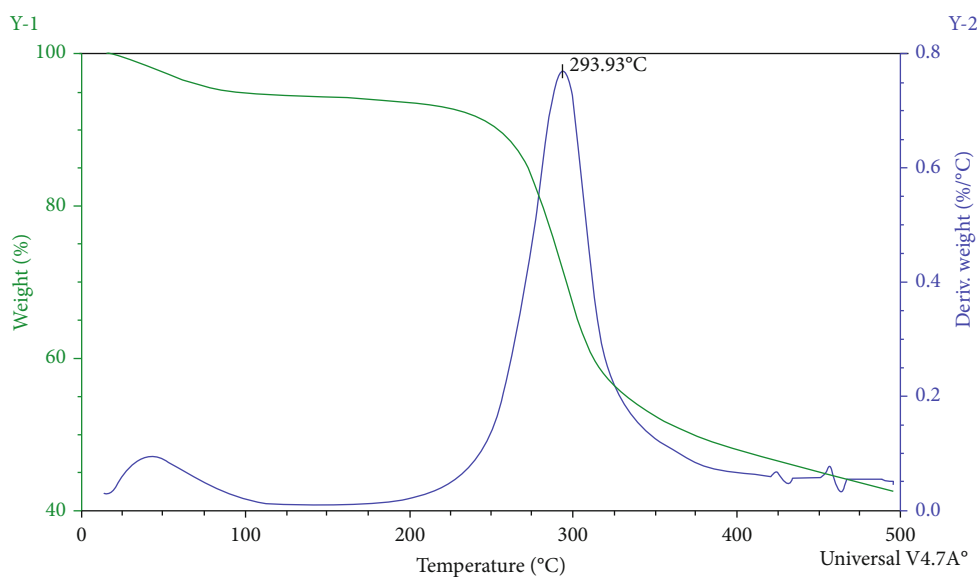
FIGURE 6: TGA Ag [A]-Qs QDs. The decomposition temperature of the compound (293.93°C) at a heating rate of 10°C/min in gas nitrogen flow.

The elemental analysis of each composite by means of dispersive X-ray spectroscopy (SEM/EDX) determines that Au QDs, both in concentration [A] and [B], are those with the lowest atomic percentage (0% for those of [A] and 0.06% for [B]) in the surface of the polymer compared to the Ag and CuQDs. This could suppose that Au QDs are absorbed by the polymer and tend to be less likely to oxidize, unlike Cu [B] QD which has the highest percentage (1.59% for [B]) leading to an increased instability and a tendency to agglomeration and oxidation. But to have absolute certainty of the composition of the metals in the polymer, elemental analysis by atomic absorption is required.

As for the results obtained in thermogravimetric methods, it is observed that the thermal degradation of metal QDs supported in chitosan has a lower decomposition temperature than that of pure polymer. This is because the covered metal nanoparticles act as an impurity by lowering the decomposition temperature of the metal, which increases entropy as it is a composite. However, this difference between pure chitosan and doped chitosan QDs is sparse and is within a range of 291-296°C, so QDs do not alter the inherent physical properties of the chitosan itself. MQDs generally decrease Td, because they are incorporated, and increase system entropy. In addition, DSC shows that all QDs undergo
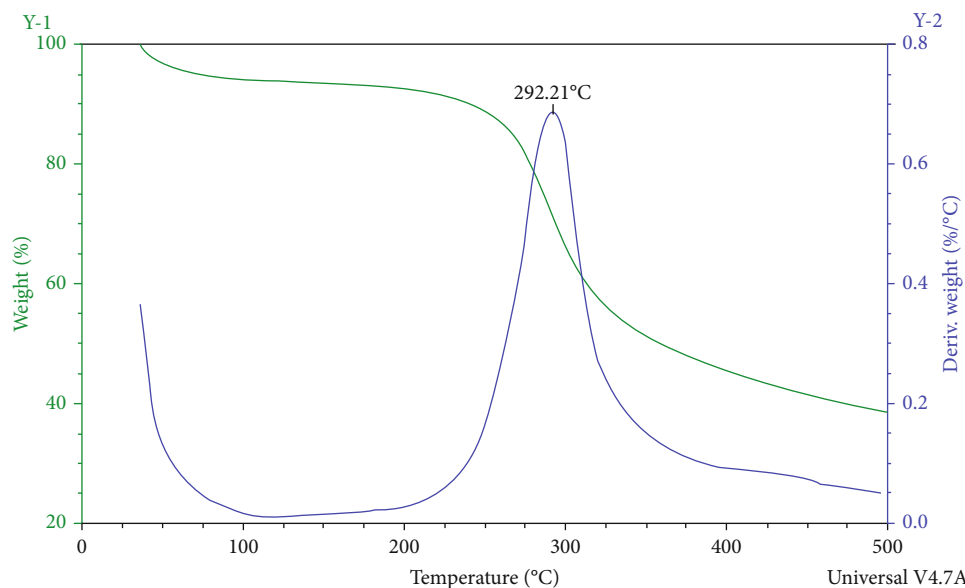
FIGURE 7: TGA Cu [A]-Qs QDs. The decomposition temperature of the compound (292.21°C) at a heating rate of 10°C/min in gas nitrogen flow.
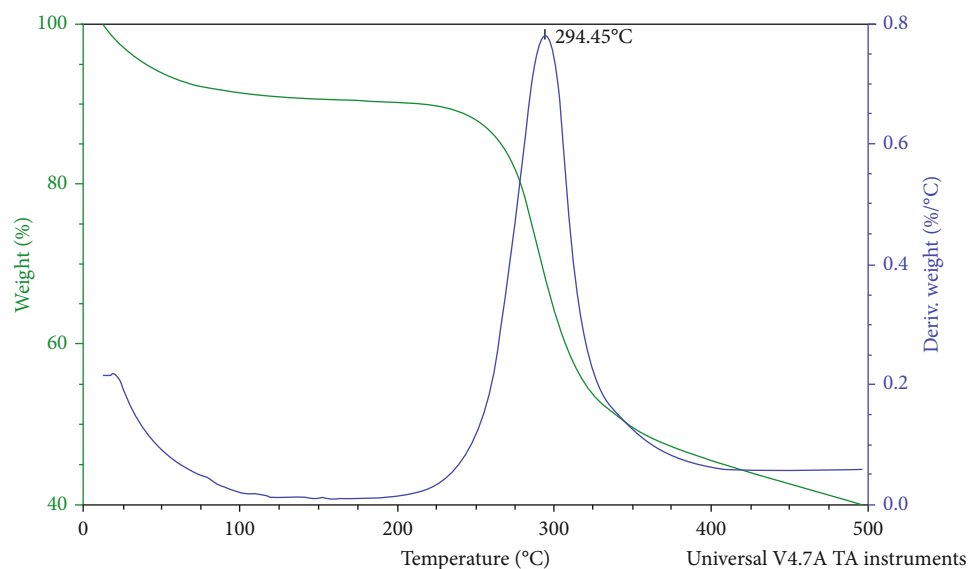
FIGURE 8: TGA Au [A]-Qs QDs. The decomposition temperature of the compound (294.45°C) at a heating rate of 10°C/min in gas nitrogen flow.

the same transition change as chitosan when subjected to heating of 10°C, i.e., they go through a cold crystallization prior to the fusion process.

FT-IR analyses confirm the interaction of gold, silver, and copper QDs due to the M-N (Metal-Amine) groups of the chitosan. A decrease in the absorption wavelength of M-N occurs due to the back bonding of nitrogen electrons into the orbitals of the metal. Due to the presence of the M-M (Metal-Metal) interaction present in the far infrared, it is clear that there is a duality of metal particles, presenting the two forms, oxidized and nonoxidized of metal QDs. This may be because 2-ethoxyethanol is used as a solvent in the stirring stage within the reactor, which can oxidize the supported colloid in the polymer matrix, even if it is dry. According to Mayer et al. [24], MQDs are encapsulated in a sphere of solvation that helps stabilize QDs with subsequent inclusion in the chitosan matrix at the time of synthesis. Also checked in the FT-IR is the M-O (oxygen - OH of the solvent) stretch that is generated in the far range, which determines the interaction of the metal particles with the electron pair of the 2-ethoxyethanol OH functional group, through the M-O bond. In addition, the results show high carbon content present in metals so that the above mentioned by Mayer et al. [24] is met.

TABLE 4: Summary table of kinetic parameters for thermal degradation of chitosan and chitosan doped metal nanoparticles (MQDs).

Polymer	Concentrations $(M) \times 10^{-4}$	DT (°C)	DSC EXO mJ(−) (°C)	DSC ENDO mJ(−) (°C)
Qs	1111	295.18	1838.5 (96.7)	1800.1 (308)
Au [A]	2.5	294.45	1124.7 (95.5)	901.47 (309)
Au [B]	5.1	294.84	859.63 (90.6)	833.20 (307)
Ag [A]	4.6	293.93	808.90 (99.5)	1025.3 (310)
Ag [B]	9.3	293.37	1302.2 (98.4)	1365.3 (307)
Cu [A]	7.9	292.21	1613.9 (103)	1107.4 (306)
Cu [B]	15.7	291.60	641.90 (100)	85.400 (306) 8.110 (338)
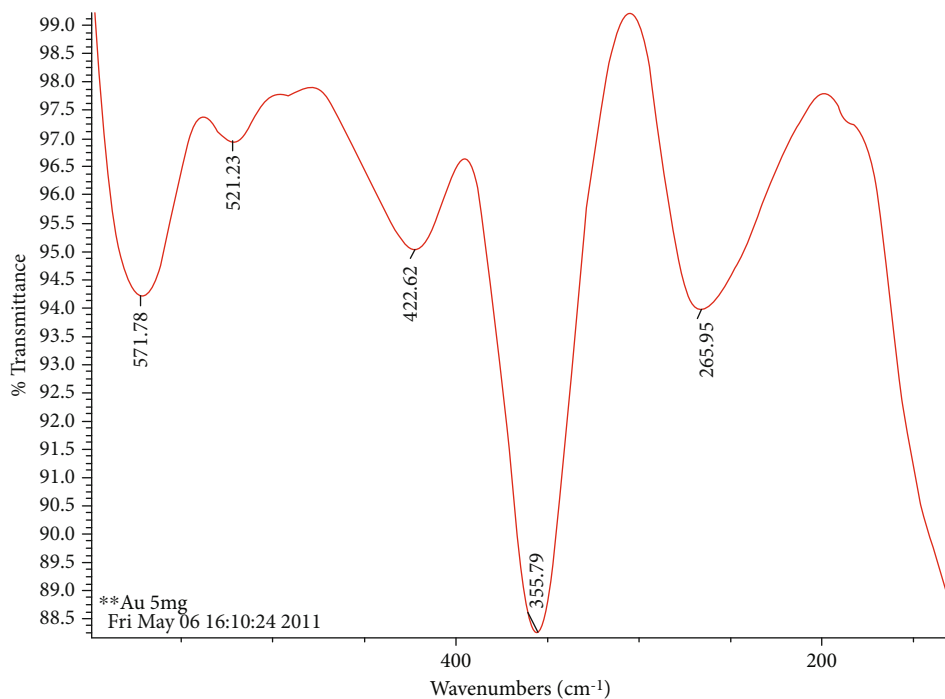
FIGURE 9: Far infrared spectrum for gold quantum dots (Au [A]-Qs) supported in chitosan.

In microbial susceptibility tests, both agar diffusion and macro serial dilution show a tendency of a best antimicrobial activity of QDs at concentration [B] against Gram-negative (G(-)) bacteria (*E. coli* and *S. Typhi*) and concentration [A] on Gram-positive (G(+)) *S. aureus*. This may be due to the structure of the cell wall where the G (-) have an outer membrane with lipopolysaccharide (LPS), which is a highly electronegative charge. On the other hand, the teichoic acid present on the surface of G(+) bacteria is less electronegative, which would generate more adsorbed chitosan on Gram-negative bacteria and therefore greater inhibitory effect, which is why according to Chung et al. [25], increased antimicrobial activity is obtained against *E. coli* culture than in *S. aureus*.

The lower inhibition zone shown by *S. Typhi* means that this microorganism was the most resistant to the tested compounds. This result is consistent with macrodilution in broth. This may be due to the chemical composition of the LPS

layer, which is composed of sugars such as galactose, glucose, rhamnose, and mannose that form sequences of four or five units that are often branched. This can be an obstacle for the binding of chitosan to fatty acids present in the LPS by an amino ester bond [26]. Another factor that could influence the resistance of this bacteria is its ability to survive at low pH media and the presence of many organic acids [27], and the chitosan-QDs were solubilized in 1% acetic acid.

The low ratio MBC/MIC (1 or 2) observed means that NPs have a predominantly bactericidal behavior [28]. The Ag NPs showed the best antibacterial effect expressed as the lower MIC for the bacterial strains tested. This could be explained because Ag's NPs are the smallest, which would facilitate their entry into the cell and hence its attack mechanism [29].

A best antibacterial effect was observed in the chitosan-supported metal QDs, compared to nondoped chitosan at

Table 5: FT-IR spectra in mid and far range of solvent, chitosan, and Au, Ag, and Cu solids supported in chitosan.

Characteristic bands	Solvent	Chitosan	Au [A]	Au [B]	Ag [A]	Ag [B]	Cu [A]	Cu [B]
Axial stretching -OH and -NH$_2$	3464	3375.62	3464.46 3289.85	3472.0 3290.46	3419.3	3426.71	3427.43	3425.01
Asymmetrical axial stretch -C-H$_2$	2918.5	2930.83	-	-	2920.25	2912.56	2919.76	2920.99
Symmetrical axial stretch -C-H$_2$	2875	-	2875.84	2878.22	2873.83	2874.78	2866.47	2862.62
Stretch -C=O	-	1558.61	1596.72	1596.88	1648.71	1601.51	1641.54	1721.70
Balancing -CH$_2$	1417	1411.46	1425.75	1426.19	1425.57	1426.08	1431.76	1426.10
Coupled deformation modes of H-C-H; C-H; -C-OH	1291 1231 1170	-	1331.02 1259.37	1327.25 1255.64	1329.87 1260.72	1329.87 1256.88	1321.58	1318.34 1264.56
Stretching of C-O and C-O-C	1057	1151.50	1090.31	1087.60	1089.76	1091.70	1084.41	1087.09
Stretching v (M-O)	-	517.11	571.95 521.23	564.78 515.23	578.12 522.77	579.96 522.17	584.34 524.53	518.15
Stretching v (M-N)	-	-	422.62	420.22	417.61	418.34	419.43	-
δ(CH) ρ(COO)	-	356.29	355.79	354.67	354.52	355.02	355.36	354.06
N-M-N	-	-	265.95	264.50	267.41	265.87	-	265.59
M-M	-	-	-	-	114.97	164.93 112.39	168.16 112.55	113.61
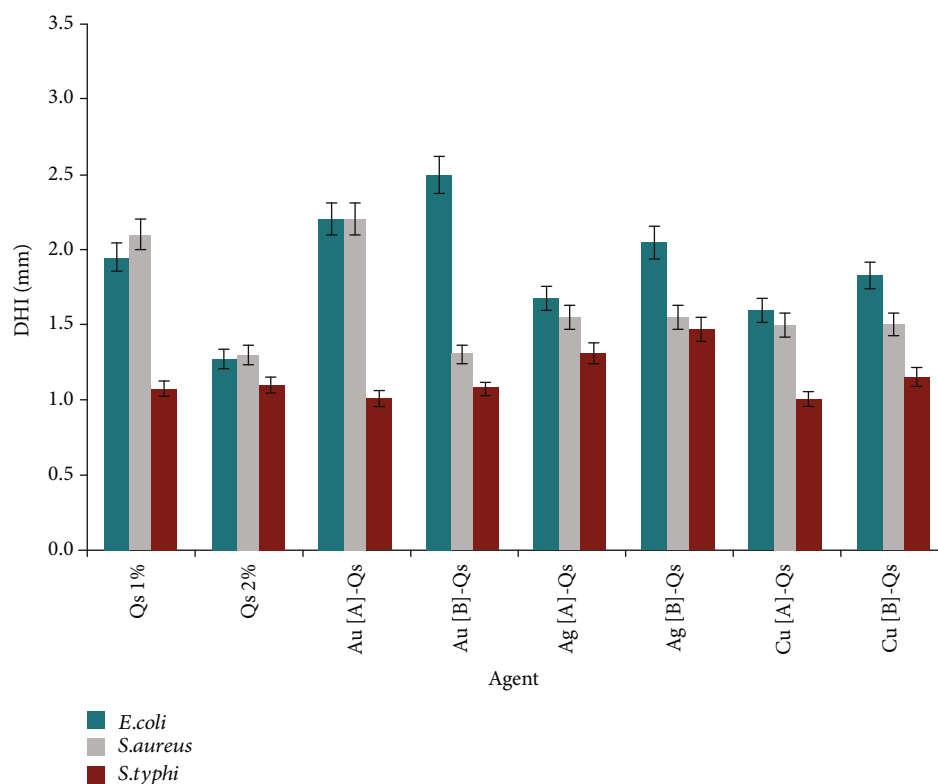
Figure 10: Diameter of inhibition zone (DHI) in disk diffusion test of the formulations studied at 1% w/v suspended in 1% v/v acetic acid for cultures of *E. coli*, *S. aureus*, and *S. Typhi*.

2% (w/v) which means that the combined antibacterial effect of chitosan and QDs had a synergistic effect.

It was also observed that Ag NPs synthesized at a concentration 7.7 M (molar concentration equal to Cu [A] QDs) show statistically different results from MIC to the treatments Ag [A], Ag [B], and Cu[A], so the wrapped metal and concentration are not the only variables that influence bacteriostatic activity.

The results of the death curve of QDs of Au [B]-Qs and Cu [B]-Qs against *E. coli* show that Cu-QDs has the higher

TABLE 6: Comparison of the MIC and MBC of samples against *E. coli*, *S. aureus*, and *S. Typhi*.

Treatments	Escherichia coli		Staphylococcus aureus		Salmonella Typhi	
	MIC	MBC	MIC	MBC	MIC	MBC
Au [A]	400	400	400	400	800	1600
Au [B]	200	400	400	1600	800	1600
Ag [A]	200	400	200	800	400	800
Ag [B]	200	400	400	1600	400	800
Cu [A]	400	800	200	800	400	800
Cu [B]	200	400	200	800	800	800
Qs 1%	400	400	400	400	800	1600
Qs 2%	800	800	800	800	800	1600
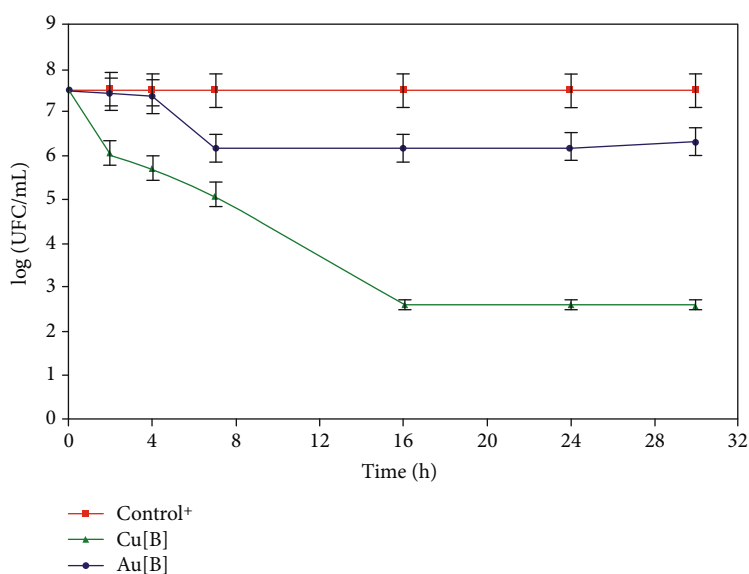
FIGURE 11: Death curve for *E. coli* exposed to the agent Au [B]-Qs and Cu [B]-Qs.

bactericidal activity after 16 h incubation, but after two hours, the effect is similar to the maximum obtained by Au QDs. These differences could be explained by the different action mechanisms of metals, which both interfere with the membrane structure, but copper nanoparticles produce multiple other toxic effects such as reactive oxygen species generation, lipid peroxidation, protein oxidation, and DNA degradation so its lethality is greater [30, 31, 32].

5. Conclusions

Through the synthesis process used in this research (CLD), it was possible to obtain QDs of Au, Ag, and Cu of relatively small size (6.0–10.0 nm on average) and uniform distribution.

The results obtained by UV-Vis and TEM confirm the presence of metals in colloidal suspension.

In the supported metal QDs, SEM with dispersive X-ray spectroscopy (EDX) makes it possible to corroborate the presence of metal clusters supported in chitosan, where the results obtained by the FT-IR method, in the far range, demonstrate that there is an interaction between the supported QDs in chitosan with the polymer matrix.

Thermal methods verify that the nanometals incorporated in the Qs do not lose the inherent thermodynamic properties of the polymer matrix and that these composites are stable up to 250°C.

The QDs of Au, Ag, and Cu obtained by the CLD method, supported in Qs by the SMAD method, and the Qs themselves, have antimicrobial activity and are demonstrated in diffusion assays in agar and in macrodilution in broth against *E. coli*, *S. aureus*, and *S. Typhi* strains, where the concentration, size, and crystalline structure of QDs together with the structure of the cell surface and the age of the culture influence the mentioned activity.

The results show that the MIC and disk diffusion test must be complemented with a death curve because the effect in the time of nanoparticles is quite different although the MIC were similar.

Data Availability

The data and additional material that support this study can be acquired directly in communication with the corresponding author.

Conflicts of Interest

The authors declare that they have no conflict of interest.

Acknowledgments

Supplementary Materials

Supplementary 1. Annex 1 shows the IR spectra of the silver and copper QDs, (Ag [A]-Qs) and (Cu [A]-Qs) respectively.

Supplementary 2. Annex 2 shows the detailed statistical analysis of antibacterial activity.

References

[1] E. N. Zare, P. Makvandi, A. Borzacchiello, F. R. Tay, B. Ashtaricf, and V. V. T. Padil, "Antimicrobial gum bio-based nanocomposites and their industrial and biomedical applications," *Chemical Communications*, vol. 55, no. 99, pp. 14871–14885, 2019.

[2] C.-Y. Wang, P. Makvandi, E. N. Zare, F. R. Tay, and L.-N. Niu, "Advances in Antimicrobial Organic and Inorganic Nanocompounds in Biomedicine," *Advanced Therapeutics*, p. 2000024, 2020.

[3] T. J. Jayeoye, O. F. Nwabor, and T. Rujiralai, "Synthesis of highly stable and dispersed silver nanoparticles/poly (vinyl alcohol-co-ethylene glycol)/poly(3-aminophenyl boronic acid) nanocomposite: characterization and antibacterial, hemolytic and cytotoxicity studies," *Journal of Industrial and Engineering Chemistry*, vol. 89, pp. 288–300, 2020.

[4] A. K. Chang, R. R. Frias Jr., L. V. Alvarez, U. G. Bigol, and J. P. M. D. Guzman, "Comparative antibacterial activity of commercial chitosan and chitosan extracted from Auricularia sp," *Biocatalysis and Agricultural Biotechnology*, vol. 17, pp. 189–195, 2019.

[5] M. K. Rai, S. D. Deshmukh, A. P. Ingle, and A. K. Gade, "Silver nanoparticles: the powerful nanoweapon against multidrug-resistant bacteria," *Journal of Applied Microbiology*, vol. 112, no. 5, pp. 841–852, 2012.

[6] S. Kalińska, M. Jaworski, and M. Wierzbicki, "Silver and copper nanoparticles—an alternative in future mastitis treatment and prevention?," *International Journal of Molecular Sciences*, vol. 20, no. 7, p. 1672, 2019.

[7] H. Holmes, L. S. P. Moore, A. Sundsfjord et al., "Understanding the mechanisms and drivers of antimicrobial resistance," *Lancet*, vol. 387, no. 10014, pp. 176–187, 2016.

[8] Z. Pang, R. Raudonis, B. R. Glick, T.-J. Lin, and Z. Cheng, "Antibiotic resistance in Pseudomonas aeruginosa: mechanisms and alternative therapeutic strategies," *Biotechnology advances*, vol. 37, no. 1, pp. 177–192, 2019.

[9] I. Ardoino, P. M. Mannucci, A. Nobili, and C. Franchi, "Antibiotic use and associated factors in a large sample of hospitalised older people," *Journal of Global Antimicrobial Resistance*, vol. 19, pp. 167–172, 2019.

[10] A. Shah, I. Hussain, and G. Murtaza, "Chemical synthesis and characterization of chitosan/silver nanocomposites films and their potential antibacterial activity," *International Journal of Biological Macromolecules*, vol. 116, pp. 520–529, 2018.

[11] N. Y. Elmehbad and N. A. Mohamed, "Designing, preparation and evaluation of the antimicrobial activity of biomaterials based on chitosan modified with silver nanoparticles," *International Journal of Biological Macromolecules*, vol. 151, pp. 92–103, 2020.

[12] R. Jamaledin, C. K. Y. Yiu, E. N. Zare et al., "Advances in antimicrobial microneedle patches for combating infections," *Advanced Therapeutics*, p. 2002129, 2020.

[13] G. Cárdenas-Triviño, "Chemical reactions at nanometal particles," *Journal of the Chilean Chemical Society*, vol. 50, pp. 603–612, 2005.

[14] G. Cárdenas-Triviño, C. Elgueta, L. Vergara, J. Ojeda, A. Valenzuela, and C. Cruzat, "Chitosan doped with nanoparticles of copper, nickel and cobalt," *International Journal of Biological Macromolecules*, vol. 104, pp. 498–507, 2017.

[15] A. D. Tiwari, A. K. Mishra, S. B. Mishra, O. A. Arotiba, and B. B. Mamba, "Green synthesis and stabilization of gold nanoparticles in chemically modified chitosan matrices," *International Journal of Biological Macromolecules*, vol. 48, no. 4, pp. 682–687, 2011.

[16] C. Cruzat, *Síntesis y caracterización de nanopartículas metálicas soportadas en Quitosano*, Tesis presentada a la Universidad de Concepción para grado académico de Doctor en Química, Chile, 2010.

[17] H. S. Mansur, A. P. Mansur, E. Curti, and M. V. De Almeida, "Bioconjugation of quantum-dots with chitosan and N,N,N-trimethyl chitosan," *Carbohydrate Polymers*, vol. 90, no. 1, pp. 189–196, 2012.

[18] A. P. Mansur, H. S. Mansur, F. P. Ramanerya, L. C. Oliveira, and P. P. Souza, ""Green" colloidal ZnS quantum dots/chitosan nano-photocatalysts for advanced oxidation processes: Study of the photodegradation of organic dye pollutants," *Applied Catalysis B: Environmental*, vol. 158-159, pp. 269–279, 2014.

[19] C. Gamazo, I. López, and R. Díaz, "Manual Práctico de Microbiología 3ra Edición," *Editorial Masson*, pp. 121–132, 2005.

[20] J. A. Creighton and D. G. Eadon, "Ultraviolet-visible absorption spectra of the colloidal metallic elements," *Journal of the Chemical Society, Faraday Transactions*, vol. 87, no. 24, pp. 3881–3891, 1991.

[21] S. I. Pokutnyi, O. V. Ovchinnikov, and T. S. Kondratenko, "Absorption of light by colloidal semiconductor quantum dots," *Journal of Nanophotonics*, vol. 10, no. 3, p. 033506, 2016.

[22] R. C. Ashoori, "Electrons in artificial atoms," *Nature*, vol. 379, no. 6564, pp. 413–419, 1996.

[23] M. A. Kastner, "Artificial atoms," *Physics Today*, vol. 46, pp. 1–24, 1993.

[24] G. Cárdenas, J. Díaz, and A. García, "Lethal effect of chitosan-Ag (I) films on Staphylococcus aureus as evaluated by electron microscopy," *Journal of Applied Microbiology*, vol. 108, pp. 633–646, 2009.

[25] C. R. Mayer, S. Neveu, C. Simonnet-Jégat, C. Debiemme-Chouvy, V. Cabuil, and F. Secheresse, "Nanocomposite systems based on gold nanoparticles and thiometalates. From colloids to networks," *Journal of Materials Chemistry*, vol. 13, no. 2, pp. 338–341, 2003.

[26] Y. Chung, Y. Su, C. Chen et al., "Relationship between antibacterial activity of chitosan and surface characteristics of cell

wall," *Acta Pharmacologica Sinica*, vol. 25, no. 7, pp. 932–936, 2004.

[27] V. N. Davydova, I. M. Yermak, V. I. Gorbach, I. N. Krasikova, and T. F. Solov'eva, "Interaction of bacterial endotoxins with chitosan. Effect of endotoxin structure, chitosan molecular mass, and ionic strength of the solution on the formation of the complex," *Biochemistry*, vol. 65, no. 9, pp. 1082–1090, 2000.

[28] S. L. Foley and A. M. Lynne, "Food animal-associated Salmonella challenges: pathogenicity and antimicrobial resistance," *Journal of Animal Science*, vol. 86, pp. 173–187, 2008.

[29] W. A. Craig, "State-of-the-art clinical article: pharmacokinetic/pharmacodynamic parameters: rationale for antibacterial dosing of mice and men," *Clinical Infectious Diseases*, vol. 26, no. 1, pp. 1–10, 1998.

[30] D. Wei, W. Sun, W. Qian, Y. Ye, and X. Ma, "The synthesis of chitosan based silver nanoparticles and their antibacterial activity," *Carbohydrate Research*, vol. 344, no. 17, pp. 2375–2382, 2009.

[31] A. K. Chatterjee, R. Chakraborty, and T. Basu, "Mechanism of antibacterial activity of copper nanoparticles," *Nanotechnology*, vol. 25, no. 13, p. 135101, 2014, (12pp).

[32] Y. Cui, Y. Zhao, Y. Tian, W. Zhang, X. Lü, and X. Jiang, "The molecular mechanism of action of bactericidal gold nanoparticles on Escherichia coli," *Biomaterials*, vol. 33, no. 7, pp. 2327–2333, 2012.

Research Article

Biodegradable Films from Phytosynthesized TiO$_2$ Nanoparticles and Nanofungal Chitosan as Probable Nanofertilizers

Mohamed E. EL-Hefnawy [1,2]

[1]*Department of Chemistry, Rabigh College of Science and Arts, King Abdulaziz University, Rabigh 21911, Saudi Arabia*
[2]*Department of Chemistry, Faculty of Science, Tanta University, Tanta 31527, Egypt*

Correspondence should be addressed to Mohamed E. EL-Hefnawy; drmhefnawy723@gmail.com

Titanium dioxide nanoparticles (TiO$_2$-NPs) have great importance for plant nutrition and growth, at little concentrations. The bioactive polymer chitosan and its NPs provide outstanding characteristics for capping and enhancements of nanometals. The phytosynthesis of TiO$_2$-NPswas promisingly achieved using an extract of pomegranate rind, whereas the fungal chitosan (FCt) was produced from *Aspergillus brasiliensis* biomass and was transformed to nanoform. The phytosynthesis of TiO$_2$-NPs generated homogenous spherical particles with 13 to 64 nm range and 37 nm mean size. The extracted FCt had 92% deacetylation degree and a molecular weight of 28,400 Da. The infrared spectral analysis of TiO$_2$-NPs, FCt-NPs, and their nanocomposite indicated their functional groups and biochemical interactions. The released amounts of TiO$_2$-NPs from their nanocomposite with FCt–NPs were 31% and 50% after the first and third hour, respectively. The nanocomposite film had a faster hydrodegradability rate which resulted from TiO$_2$-NP addition. Therefore, the fabricated nanocomposite from FCt/TiO$_2$-NPs could have elevated potentiality for application as liquid spray for foliar feeding or as powder for soil amendment.

1. Introduction

Titanium (Ti) element has important biological consequence for plants, being advantageous at lower concentrations and potentially toxic at higher ones, but with miniature toxicity toward animals or human [1]. Whereas TiO$_2$ antimicrobial potentiality was reported against many microorganisms [2, 3], it has many beneficial consequences for plant physiological attributes, especially at little dosages (the Ti contents in plant dry weight ranged from 1 to 1000 mg/kg with profitable application range of up to 100 mg/L), including their elemental contents, biomass yield, chlorophyll contents, and foliar growth [4–6].

Nanofertilizers emerged as promising candidates for enhancing micronutrients' uptake efficiency; their successful practical applications promoted the search for more systems to improve their delivery, e.g., nanocarriers and nanocomposites [7, 8]. Formulated nanofertilizers could have slower release of nutrients, which improves their usage, solubility, bioavailability, and dispersion [7]. Compared to traditional fertilizers, nanofertilizers could be absorbed by crops easily, with sustained nutrient delivery into soil/plant [8].

While numerous metals/metal oxide NPs were effectually applied in plant-related sciences (including TiO$_2$, ZnO, AgNO$_3$, Fe$_3$O$_4$, and CeO$_2$), TiO$_2$-NPs represented the most frequently applied nanometals in agricultural investigations [5, 9].

The practical exogenous applications of TiO$_2$-NPs in crop propagation indicated their efficacy for enhancing plant performance, biomass production, photo-reduction activities, and nitrogen assimilation [10, 11]. Moreover, these micronutrient NPs could protect chloroplast membranes from reactive oxygen species (ROS) attacking and destruction [4]. TiO$_2$-NPs can also improve other native nutrient

utilization via support of beneficial microbial activities [12]. The TiO$_2$-NPs were effectually phytosynthesized (synthesis enforced by plant derivatives) using extract of various parts of plants [13–15], which was advised for increasing the process safety, feasibility, and efficiency.

The biosynthesis (green synthesis) of nanomaterials has recently become a key method for preparation of many bioactive NPs with augmented activity and reduced toxicity during their preparation and applications; the synthesis could be enforced by NPs incorporation with numerous types of biopolymers [16–18].

Biosynthesized nanometals and nanocompounds were validated as effectual and powerful antimicrobial agents in biomedical fields and their successful applications were proved [19–21].

The extract of pomegranate rinds (PRE), as a byproduct with plenty of valuable phytochemicals and biological activities, was employed for the green phytosynthesis of many metal NPs including silver, iron, and zinc [22–24], as the PRE exhibited strong reducing capability for these metals.

Chitosan (Cts), the astonishing derived amino polysaccharide from chitin deacetylation, possesses plentiful advantageous attributes (e.g., its biosafety, biodegradability, biocompatibility, nontoxicity, and efficacious bioactivities) [25]. The extraction of Cts from different fungal biomasses was promisingly achieved [26, 27]; this fungal chitosan (FCt) had comparable or superior bioactivities than commercial Cts from crustacean shells.

The polymer NPs, particularly from Cts and FCt, are well proved for their surplus functionalities and bioactivities as nanocarriers, biochelators, antimicrobial, biosorbent, and plant protectant agents, in individual or composited forms with other bioactive compounds and nanomaterials [28–30].

The application of Cts and FCt-NPs was advised for soil and water remediation from heavy metals due to their capabilities for heavy metal chelation/adsorption [28, 29].

The incorporation of TiO$_2$ with Cts was reported to improve the composite structural, mechanical, optical, textural, vapor barring, and thermal properties and its biodegradability [31]. These composites had also augmented antimicrobial, viscoelastic, and biocompatibility attributes [3, 32, 33].

Accordingly, the intentions from this investigation were to phytosynthesize TiO$_2$-NPs using PRE, extract FCt from grown mycelia of *Aspergillus brasiliensis* and transform it to NP form, then to conjugate both NPs for augmenting their release pattern and hydrodegradability.

2. Materials and Method

2.1. Pomegranate Rinds' Extract (PRE) Preparation. Organic pomegranate fruits (*Punica granatum* L.), obtained from international markets in KSA, Jeddah, were used in study. Fruits were disinfected (using 5% sodium hypochlorite solution) and peeled and their rinds were dried (for 50 h at $48 \pm 2°$C) and ground to 60-mesh powder size. The PRE was prepared through powder immersion for 36 h in ethanol (70%) with agitation then filtration to have the extract, which was vacuum dried at 42°C and resuspended in deionized water (DIW) to have 10%(w/v) concentration [34].

2.2. Phytosynthesis of TiO$_2$ Nanoparticles. Titanium (IV) chloride (TiCl$_4$, Sigma-Aldrich, Saint Louis, MO; purity ≥ 99.9%) was the precursor for TiO$_2$-NP phytosynthesis.

For TiO$_2$-NP phytosynthesis, 50 mL of TiCl$_4$ solution in DIW (95 mg/mL) was mixed with equal volume of PRE with strong stirring for 60 min at $25 \pm 1°$C. The changing solution color to whitish-brown indicated TiO$_2$-NP synthesis. Ammonium hydroxide solution (0.2 M) was slowly added to NP solution under stirring at $25 \pm 1°$C, until reaching alkaline pH of 8.0 and precipitate formation. The precipitated TiO$_2$-NPs were collected via centrifugation (at 8600°g), washed with ethanol (95%), recentrifuged, and calcined at $470 \pm 5°$C for 200 min, then powdered finely.

2.3. Preparation of Fungal Chitosan/TiO$_2$-NP Composite. Grown mycelia of *Aspergillus brasiliensis* (ATCC-16404), after aerobic propagation in broth media of potato dextrose (containing infusion of 200 g potato+20 g dextrose/L), were used as chitosan source by extraction according to Tayel et al. [26]. Briefly, inoculated fungal conidial suspension (10^6 spores/mL), in 500 mL of broth medium, were incubated aerobically under stirring (120 g) for 6 days at 28°C.The FCt extraction involved fungal biomass harvesting and washing with DIW, treatment with 20 folds (v/w) from 1 M of NaOH then HCl and finally deacetylation by treatment with 20 folds from 60% (w/v) NaOH solution for 60 min at 110°C.

The molecular weight of FCt was determined by gel permeation chromatography (GPC) with the following specifications: GPC (PN-3000), together with a refractive index detector (PN-1000) from Post-nova analytics, Eresing, Germany, was operated at15°C and 90°C. The used columns for detection were Nucleogel GFC 1000-8 (Macherey-Nagel GmbH & Co. KG, Düren, Germany) and Gral300 by (Polymer Standards Service GmbH, Mainz, Germany). Standard pullulans (with molecular weight of 11,800, 47,300, 112,000, and 780,000) were used for calibration.

The calculation of FCt deacetylation degree (DD) was based on its infrared spectral analysis using FTIR (Fourier-transform infrared spectroscopic -FTS 45, Bio-Rad, Germany), using the absorbance ratios at A1655/A3450.2.4.

The FCt-NP synthesis employed ionotropic gelation method (based on the electrostatical interaction of positively charged FCt molecules with the negatively charged pentasodium tripolyphosphate "Na-TPP", Sigma-Aldrich, St. Louis, Mo.); FCt solution (0.5% w/v) in 1.5% acidic solution (CH$_3$COOH, Sigma-Aldrich) was prepared and sonicated at 50 W for 20 min (Braun-Labsonic, Germany). Equal volume from Na-TPP solution (of 0.5% w/v in DIW) was slowly dropped into stirred FCt solution, then resonicated and centrifuged (at 8400 × g for 25 min). The obtained FCt-NP pellet was sonicated after suspension in DIW and recentrifuged [29].

Later, 500 mg of FCt-NPs (dissolved in 50 mL of 1.5% acetic acid solution) and 50 mg from TiO$_2$-NPs (dispersed in 5 mL of DIW) were combined and then sonicated for 30 min. The uniform composite emulsion was further magnetically stirred for 250 min to enforce NP crosslinkage [3].
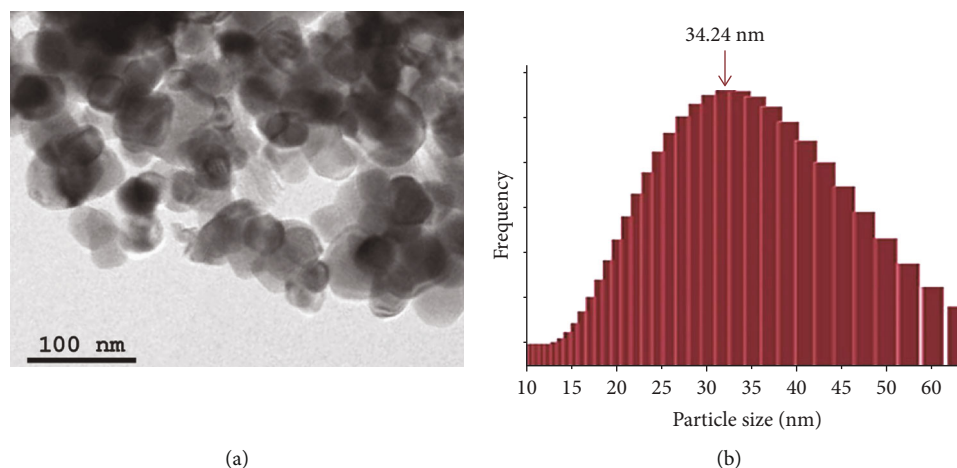
(a)

(b)

FIGURE 1: Phytosynthesized TiO$_2$ nanoparticles, indicating their morphological features using TEM (a) and particle size distribution (b).

2.4. Characterization of Synthesized Nanoparticles. The FTIR spectroscopy was employed for analyzing the functional groups of NPs and nanocomposite (TiO$_2$-NPs, FCt-NPs, and FCt/TiO$_2$-NPs) at a wavenumber range of 550-4000 cm^{-1}, after integration of NPs with 1% KBr. The TiO$_2$-NP size distribution and charges were estimated via PCS (photon correlation spectroscopy, Malvern™ Zetasizer, Malvern, UK), and their structure was further confirmed via TEM (transmission electron microscopy; Leica™ Leo0430, Cambridge Ltd., UK). The surface morphology and appearance of the nanocomposite were screened using SEM imaging (scanning electron microscopy, JEOL JSM-IT100, Tokyo, Japan).

2.5. TiO$_2$-NP Release from FCt Nanoconjugates. The dispersed TiO$_2$-NPs in FCt solution was ultrasonicated for 120 min and dispensed onto Petri plates; then, their solvent (acidified DIW, pH 5.2) was vacuum evaporated for 16 h. The dried formed films were peeled and immersed in 50 folds (w/v) from neutral DIW, which were agitated at $320 \times g$, and 10 mL from the supernatants was gathered for 180 min, with 30 min intervals. Samples were analyzed for Ti content according to Korn et al. [35], involving treatment with 40 folds (v/w) from concentrated hydrofluoric (50%) and sulfuric (98%) acids then dilution with 3% HNO$_3$ and ion determination using ICP (inductively coupled plasma optical emission spectrometer, OES-5110, Agilent Inc. Santa Clara, CA).The experiments were performed in triplicate and their mean values were calculated.

2.6. Hydrolytic Degradation of NPs-Based Films. The hydrolytic degradation percentage of NPs-based films (FCt-NP and FCt/TiO$_2$-NP composites) was performed in triplicate at $25 \pm 2°$Cfor 10 h, with 60 min intervals, using 10×10 mm film squares. The NP films were immersed in neutral DIW, with slow stirring, for each interval time; then, they were attained via filtration to disregard DIW and dissolved materials. The residual films were vacuum dried and weighed to assess their mass loss [36].

3. Results and Discussion

3.1. TiO$_2$-NP Phytosynthesis Using PRE. The TiO$_2$-NPs could be successfully synthesized using PRE, as evidenced from their characterization (Figure 1). The phytosynthesized TiO$_2$-NPs appeared with spherical and matched shapes with slight NP agglomerations (Figure 1(a)). The TiO$_2$-NP size distribution ranged from 13.42 to 63.84 nm, with 34.21 nm median size and 36.71 nm mean size (Figure 1(b)). The recorded Zeta potential average for these phytosynthesized TiO$_2$-NPs was –24.8 mV.

Numerous bioactive compounds are contained in PRE, including polyphenols, vitamins, flavonoids, esters, and protein. The polyphenols, vitamin C, and many other phytoconstituents contain extensive hydroxyl groups with strong reducing capability [22]. PRE was acknowledged to contain extraordinarily elevated phenolic compounds as natural antioxidants sources [37]. Thus, these biactive phytoconstituents are assumingly the one responsible for reducing TiO$_2$ to their NP form.

The PPE was effectively employed for the phytosynthesis of many metal nanoparticles, e.g., silver, gold, and zinc [22, 23, 38]; this is matching with its capability forTiO$_2$-NP synthesis in current study.

3.2. Fungal Chitosan Extraction. The chitosan was effectually extracted from *A. brasiliensis* mycelia; the extracted FCt had a molecular weight of 28,400 Da with 92.1% deacetylation degree.

The successfulness of FCt extraction from *A. brasiliensis* confirmed foregoing investigations that reported the fungi potentialities as sustainable alternative sources for Cts production [26, 28, 29, 39]; these reports applied the extracted FCt, from varied fungal genera, in the environmental and biomedical fields.

3.3. Nanoparticle Characterization. The FTIR spectral evaluation was conducted for FCt-NPs, TiO$_2$-NPs, and their nanocomposite (FCt/TiO$_2$-NPs) to appraise their biochemical bonds and the potential interaction/crosslinkage between the synthesized NPs. For TiO$_2$-NP spectra (Figure 2, TiO$_2$-
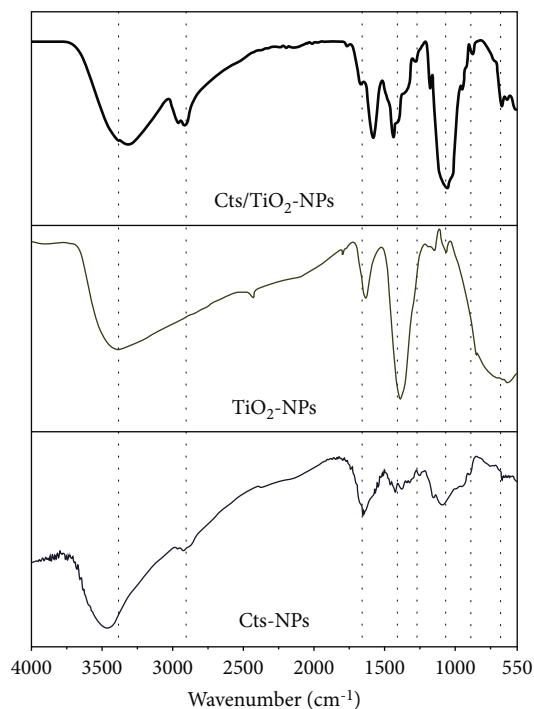
FIGURE 2: Infrared spectral analysis (FTIR) of chitosan nanoparticles (Cts-NPs), titanium dioxide nanoparticles (TiO$_2$-NPs), and their composite (Cts/TiO$_2$-NPs).

NPs), the representative broad peak of Ti–O–Ti stretching was detected around 612 cm^{-1} wavenumber. The appeared vibrated bands at 1107 and 1120 cm^{-1} are specified the stretching/bending modes of CH$_3$ and Ti–OH, respectively, of the NPs surface groups [40].

The sharp peak (at 1638 cm^{-1}) and the broad peak (at 3405 cm^{-1}) are mainly attributed to the NP adsorbed water and occurrence of hydroxyl groups, respectively [14]. The hydroxyl groups' presence is commonly involving the photocatalytic activity augmentations; with the increased amount of OH– on TiO$_2$-NP surface, their higher electron transportability and enhanced photocatalytic activity could be assumed [41].

The appeared peak at 651 cm^{-1} in TiO$_2$-NP spectrum conceivably indicated the involvement of Ti anatase phase in phytosynthesized NPs; this phase could be further confirmed via X-ray diffraction (XRD) analyses. Conversely, the disappearance of any peaks around 2900 cm^{-1}, which indicates C–H stretching, validated that subtraction of the entire PRE organic components from the TiO$_2$-NP sample during their calcination [14].

For FCt-NP spectrum (Figure 2, Cts-NPs), the strong wide peak around 3453 cm^{-1} could correspond to combined O–H stretching and hydrogen bonding; the peak wideness with increased intensity could indicate hydrogen bonding enhancement after NP synthesis [30]. The FCt-NP spectrum displayed also (at 1171 cm^{-1}) a sharp indicating peak for P=O, due to crosslinkage of FCt with TPP. The main characteristic absorption peaks of FCt were detected at 1714 cm^{-1} (C=O carbonyl stretching within the secondary amide I band), at 1541 and 1322 cm^{-1} (the bending vibration of
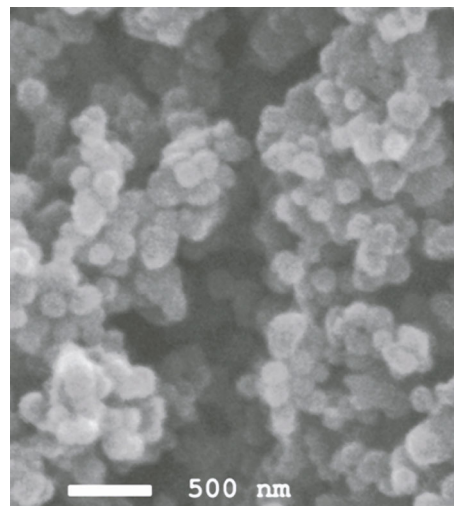
FIGURE 3: Scanning electron micrograph of nanoparticles composited from nanochitosan and nano-TiO$_2$.

N–H in amide II and the amide III absorption, respectively), and at 1083 cm^{-1} (due to C–O–C stretching).

For FCt/TiO$_2$-NPs, the appeared peak at 1391 cm^{-1} indicates the CH$_3$ band stretching vibrations in the nanocomposite [32, 33], and the TiO$_2$-NP incorporation had obvious impact on the intensities of characteristic peaks (Figure 2, Cts/TiO$_2$-NPs).

The nanocomposite spectrum displayed many characteristic bands and peaks from both FCt-NPs and TiO$_2$-NPs (designated by the vertical lines on the figure). The Ti–O band within 550–700 cm^{-1} range designated TiO$_2$ immobilization onto FCt matrix [42]. Compared with pure FCt-NP spectrum, many corresponding bands to amino, hydroxyl, and amide groups were shifted in FCt/TiO$_2$-NP composite spectrum; these IR shifts confirmed the interaction between both the conjugated NPs.

The composited FCt/TiO$_2$-NP microstructure and morphology were elucidated using SEM imaging (Figure 3); they appeared with homogenized spherical shapes with some aggregation due to polymer collapse. The TiO$_2$-NPs were mostly capped with FCt-NPs and composed uniform mixtures, as was formerly reported [33, 42]. The low aggregate size in the nanocomposites is assumingly attributive to the organic nature of FCt that could hinder the aggregation of TiO$_2$-NPs [43].

3.4. Release Pattern of TiO$_2$-NPs from FCt–NP Nanocomposite.

The release pattern of TiO$_2$-NPs from their nanocomposite with FCt–NPs is performed throughout 180 min releasing time (Figure 4); the released TiO$_2$ amounts from the nanocomposite were 31.2% after the first hour and reached 50.2% at the experiment end. The release pattern TiO$_2$-NPs and its influence with stirring time was indicated from other colloids, cream, and sunscreen [44, 45]; the TiO$_2$ release percentages in these studies were higher than the obtained values in a current study, which indicate the high capability of FCt-NPs for entrapping and capping the TiO$_2$-NPs and preventing them from disintegration. The main suggested factor for TiO$_2$-NP
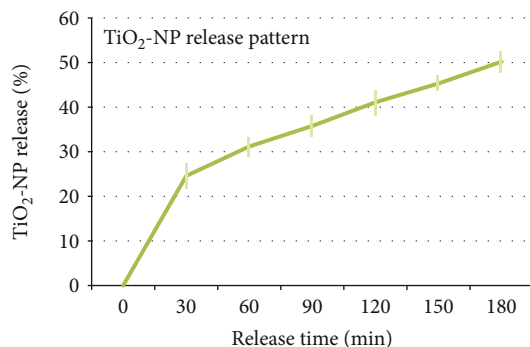
FIGURE 4: The release pattern of TiO$_2$-NPs from their nanocomposite with nanochitosan. *Values are mean of triplicates with the illustrated error bars.

FIGURE 5: The hydrodegradation patterns of prepared films from nanochitosan (CTs film) and its composite with TiO$_2$-NPs (CTs/TiO$_2$ film). *Values are mean of triplicates with the illustrated error bars.

releasing could be the degradation of FCt-based film that assists the liberation of capped metal NPs.

The controlled release of TiO$_2$-NPs, via their conjugation with FCt-NPs, is highly important for sustained fortification of plants with Ti ions for longer times and required concentrations [12, 46].

Many patents and inventions advocated TiO$_2$-NP applications in plant fertilization purposes, either as liquid or colloidal compositions, which could promote foliar and root growth [6, 12]; this supports the potential application of current fabricated FCt/TiO$_2$-NP composites as sustained and controlled source of Ti ions for plant fertilization. In addition, the controlled release of Ti, via incorporation in FCt/TiO$_2$-NP composites, could be highly beneficial for providing the plant with this essential element without its potential toxicity at higher doses [6]. The sustained release of TiO$_2$-NPs could, additionally, provide advantageous long-lasting antimicrobial potentiality against the pathogenic microbial communities in treated soils [2, 3], whereas the application of TiO$_2$-NP fertilizers was stated to have no effect on the community structure of either rhizobia or arbuscular mycorrhizal fungi that colonized plant roots, at any concentration [47]. This expected antimicrobial power from FCt/TiO$_2$-NPs could have influential consequences to protect soils and plants from pathogenic microbes.

3.5. Hydrolytic Degradation Patterns of Nanocomposed Films. The hydrolytic degradation patterns of composed films from FCt–NPs and FCt/TiO$_2$-NPs are illustrated in Figure 5. Both NPs-based films were gradually degraded and lost their weights with prolongation of experiments; the FCt/TiO$_2$-NPs-based film showed faster degradation than FCt–NPs-based film. The FCt/TiO$_2$-NP film completely degraded after 7 h of treatment, whereas the FCt–NPs film lost 67.4% of its weight at this time and its degradation percentage was 93.2% after 10 h of treatment (Figure 5).

The degradation rate of FCt/TiO$_2$-NPs-based film could be correlated with TiO$_2$-NP release from this nanocomposite, as the degradation rate was 42.8% after 3 h and the liberated TiO$_2$-NPs was slightly higher than this percentage, at the same time. The excess liberated amounts from the nanopolymer composite are assumingly due to decreased electrostatic bonds between them and electron exchanges within the nanocomposite after its hydrolytic destabilization [36, 48].
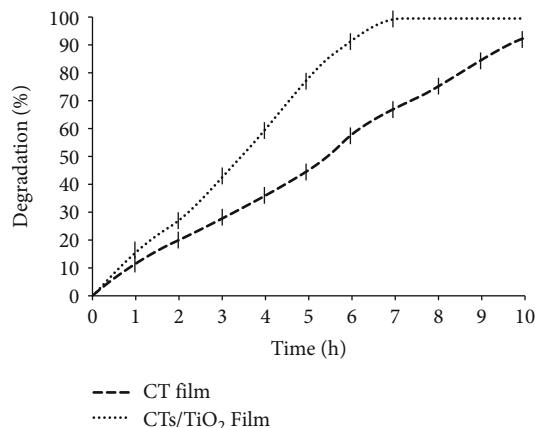
Theoretically, TiO$_2$-containing films are assumed to have a slower rate of degradation because of the antimicrobial action of TiO$_2$-NPs that can retard microbial degradation of composited films [48], but the composed films from the PLA/TiO$_2$ composite exhibited greatly higher hydrolytic degradation rate than films from PLA resin [36]; this increased degradability of TiO$_2$-incorporated films was attributed to the photodegradation properties of TiO$_2$-NPs, which is activated by NP exposure to UV and visible lights and lead to faster degradation of their composited films [36, 49]. These harmonized results with ours could advocate the incorporation of TiO$_2$-NPs into nanocomposites to control their hydrodegradability [42]. Additionally, the improvement in the biodegradability of chitosan/TiO$_2$ hybrid composite was reported as a TiO$_2$ dose dependent [31, 48], which advocates further experiments to specify the exact optimum TiO$_2$-NPs for controlling films' degradability.

However, the fabricated nanocomposite here from FCt/TiO$_2$-NPs could have elevated potentiality for application as liquid spray for foliar feeding or as powder for soil amendment [50].

4. Conclusion

The phytosynthesis of TiO$_2$-NPs was innovatively achieved using PRE and their nanocomposites with FCt-NPs had homogenous organization and miniature sizes. The nanocomposite had a faster hydrodegradability which resulted from TiO$_2$-NP addition, which advocates its application as liquid spray for foliar feeding or as powder for soil amendment. These formulated nanocomposites could be possible candidates for application as nanofertilizers to deliver TiO$_2$-NPs into plants in a controlled manner. However, more investigations are required to judge the practical application of FCt/TiO$_2$-NP nanocomposite as a fertilizer.

Data Availability

The datasets generated during and/or analyzed during the current study are available from the corresponding author on reasonable request.

Ethical Approval

This article does not contain any studies with human or animal subjects.

Conflicts of Interest

The author declares that he has no known competing financial interests or personal relationships that could have appeared to influence the work reported in this paper.

Acknowledgments

Supplementary Materials

The supplementary file includes the graphical abstract. (*Supplementary Materials*)

References

[1] F. Ghooshchi, "Influence of titanium and bio-fertilizers on some agronomic and physiological attributes of triticale exposed to cadmium stress," *Global NEST Journal*, vol. 19, no. 3, pp. 458–463, 2017.

[2] S. Yaghoubi, W. Schwietert, and J. P. Mccue, "Biological roles of titanium," *Biological Trace Element Research*, vol. 78, no. 1-3, pp. 205–217, 2000.

[3] X. Zhang, G. Xiao, Y. Wang, Y. Zhao, H. Su, and T. Tan, "Preparation of chitosan-TiO$_2$ composite film with efficient antimicrobial activities under visible light for food packaging applications," *Carbohydrate Polymers*, vol. 169, pp. 101–107, 2017.

[4] E. Morteza, P. Moaveni, H. A. Farahani, and M. Kiyani, "Study of photosynthetic pigments changes of maize (*Zea mays* L.) under nano Tio$_2$ spraying at various growth stages," *Springerplus*, vol. 2, no. 1, pp. 1–5, 2013.

[5] S. C. Capaldi Arruda, A. L. Diniz Silva, R. Moretto Galazzi, R. Antunes Azevedo, and M. A. Zezzi Arruda, "Nanoparticles applied to plant science: a review," *Talanta*, vol. 131, pp. 693–705, 2015.

[6] S. Lyu, X. Wei, J. Chen, C. Wang, X. Wang, and D. Pan, "Titanium as a beneficial element for crop production," *Frontiers in Plant Science*, vol. 8, 2017.

[7] M. R. Naderi and A. Danesh-Shahraki, "Nanofertilizers and their roles in sustainable agriculture," *International Journal of Agriculture and Crop Sciences*, vol. 5, no. 19, pp. 2229–2232, 2013.

[8] G. N. Rameshaiah, S. Jpallavi, and S. Shabnam, "Nano fertilizers and nano sensors–an attempt for developing smart agriculture," *International Journal of Engineering Research and General Science*, vol. 3, no. 1, pp. 314–320, 2015.

[9] S. Ahmed, M. Ahmad, B. L. Swami, and S. Ikram, "A review on plants extract mediated synthesis of silver nanoparticles for antimicrobial applications: a green expertise," *Journal of Advanced Research*, vol. 7, no. 1, pp. 17–28, 2016.

[10] M. Mandeh, M. Omidi, and M. Rahaie, "*In vitro* influences of TiO$_2$ nanoparticles on barley (*Hordeum vulgare* L.) tissue culture," *Biological Trace Element Research*, vol. 150, no. 1-3, pp. 376–380, 2012.

[11] U. Song, M. Shin, G. Lee, J. Roh, Y. Kim, and E. J. Lee, "Functional analysis of TiO$_2$ nanoparticle toxicity in three plant species," *Biological Trace Element Research*, vol. 155, no. 1, pp. 93–103, 2013.

[12] M. Janmohammadi, N. Sabaghnia, S. Dashti, and M. Nouraein, "Investigation of foliar application of nano-micronutrientfertilizers and nano-titanium dioxide on some traits of barley," *Biologija*, vol. 62, no. 2, pp. 148–156, 2016.

[13] V. Patidar and P. Jain, "Green Synthesis of TiO$_2$ Nanoparticle Using Moringa Oleifera Leaf Extract," *International Research Journal of Engineering and Technology*, vol. 4, no. 3, pp. 470–473, 2017.

[14] S. P. Goutam, G. Saxena, V. Singh, A. K. Yadav, R. N. Bharagava, and K. B. Thapa, "Green synthesis of TiO$_2$ nanoparticles using leaf extract of *Jatropha curcas* L. for photocatalytic degradation of tannery wastewater," *Chemical Engineering Journal*, vol. 336, pp. 386–396, 2018.

[15] M. Nadeem, D. Tungmunnithum, C. Hano et al., "The current trends in the green syntheses of titanium oxide nanoparticles and their applications," *Green Chemistry Letters and Reviews*, vol. 11, no. 4, pp. 492–502, 2018.

[16] P. Makvandi, G. W. Ali, F. Della Sala, W. I. Abdel-Fattah, and A. Borzacchiello, "Biosynthesis and characterization of antibacterial thermosensitive hydrogels based on corn silk extract, hyaluronic acid and nanosilver for potential wound healing," *Carbohydrate Polymers*, vol. 223, article 115023, 2019.

[17] P. Makvandi, G. W. Ali, F. Della Sala, W. I. Abdel-Fattah, and A. Borzacchiello, "Hyaluronic acid/corn silk extract based injectable nanocomposite: a biomimetic antibacterial scaffold for bone tissue regeneration," *Materials Science and Engineering: C*, vol. 107, article 110195, 2020.

[18] E. N. Zare, P. Makvandi, A. Borzacchiello, F. R. Tay, B. Ashtari, and V. V. T. Padil, "Antimicrobial gum bio-based nanocomposites and their industrial and biomedical applications," *Chemical Communications*, vol. 55, no. 99, pp. 14871–14885, 2019.

[19] R. Jamaledin, C. K. Y. Yiu, E. N. Zare et al., "Advances in antimicrobial microneedle patches for combating infections," *Advanced Materials*, vol. 32, no. 33, article 2002129, 2020.

[20] C. Y. Wang, P. Makvandi, E. N. Zare, F. R. Tay, and L. N. Niu, "Advances in antimicrobial organic and inorganic nanocompounds in biomedicine," *Advanced Therapeutics*, vol. 3, no. 8, article 2000024, 2020.

[21] P. Makvandi, C. Y. Wang, E. N. Zare, A. Borzacchiello, L. N. Niu, and F. R. Tay, "Metal-based nanomaterials in biomedical applications: antimicrobial activity and cytotoxicity aspects," *Advanced Functional Materials*, vol. 30, no. 22, article 1910021, 2020.

[22] H. Yang, Y. Y. Ren, T. Wang, and C. Wang, "Preparation and antibacterial activities of $^{Ag/Ag\,+\,/Ag\,3+}$ nanoparticle composites

made by pomegranate (*Punica granatum*) rind extract," *Results in Physics*, vol. 6, pp. 299–304, 2016.

[23] F. Mohamed, M. Rabia, and M. Shaban, "Synthesis and characterization of biogenic iron oxides of different nanomorphologies from pomegranate peels for efficient solar hydrogen production," *Journal of Materials Research and Technology*, vol. 9, no. 3, pp. 4255–4271, 2020.

[24] S. N. A. Mohamad Sukri, K. Shameli, M. Mei-Theng Wong, S. Y. Teow, J. Chew, and N. A. Ismail, "Cytotoxicity and antibacterial activities of plant-mediated synthesized zinc oxide (ZnO) nanoparticles using *Punica granatum* (pomegranate) fruit peels extract," *Journal of Molecular Structure*, vol. 1189, pp. 57–65, 2019.

[25] A. Ali and S. Ahmed, "A review on chitosan and its nanocomposites in drug delivery," *International Journal of Biological Macromolecules*, vol. 109, pp. 273–286, 2018.

[26] A. A. Tayel, S. A. Ibrahim, M. A. al-Saman, and S. H. Moussa, "Production of fungal chitosan from date wastes and its application as a biopreservative for minced meat," *International Journal of Biological Macromolecules*, vol. 69, pp. 471–475, 2014.

[27] A. A. Tayel, "Microbial chitosan as a biopreservative for fish sausages," *International Journal of Biological Macromolecules*, vol. 93, no. Part A, pp. 41–46, 2016.

[28] A. A. Tayel, M. M. Gharieb, H. R. Zaki, and N. M. Elguindy, "Bio-clarification of water from heavy metals and microbial effluence using fungal chitosan," *International Journal of Biological Macromolecules*, vol. 83, pp. 277–281, 2016.

[29] S. Alsharari, A. A. Tayel, and S. H. Moussa, "Soil emendation with nano-fungal chitosan for heavy metals biosorption," *International Journal of Biological Macromolecules*, vol. 118, no. Part B, pp. 2265–2268, 2018.

[30] A. I. Alalawy, H. A. El Rabey, F. M. Almutairi et al., "Effectual anticancer potentiality of loaded bee venom onto fungal chitosan nanoparticles," *International Journal of Polymer Science*, vol. 2020, Article ID 2785304, 9 pages, 2020.

[31] L. M. Anaya-Esparza, J. M. Ruvalcaba-Gómez, C. I. Maytorena-Verdugo et al., "Chitosan-TiO$_2$: a versatile hybrid composite," *Materials*, vol. 13, no. 4, 2020.

[32] F. A. Al-Sagheer and S. Merchant, "Visco-elastic properties of chitosan–titania nano-composites," *Carbohydrate Polymers*, vol. 85, no. 2, pp. 356–362, 2011.

[33] K. Kavitha, M. Prabhu, V. Rajendran, P. Manivasankan, P. Prabu, and T. Jayakumar, "Optimization of nano-titania and titania–chitosan nanocomposite to enhance biocompatibility," *Current Nanoscience*, vol. 9, no. 3, pp. 308–317, 2013.

[34] A. A. Tayel, W. F. El-Tras, S. H. Moussa, and S. M. El-Sabbagh, "Surface decontamination and quality enhancement in meat steaks using plant extracts as natural biopreservatives," *Foodborne Pathogens and Disease*, vol. 9, no. 8, pp. 755–761, 2012.

[35] M. d. G. A. Korn, A. C. Ferreira, A. C. S. Costa, J. A. Nóbrega, and C. R. Silva, "Comparison of decomposition procedures for analysis of titanium dioxide using inductively coupled plasma optical emission spectrometry," *Microchemical Journal*, vol. 71, no. 1, pp. 41–48, 2002.

[36] A. Buzarovska and A. Grozdanov, "Biodegradable poly(L-lactic acid)/TiO$_2$ nanocomposites: Thermal properties and degradation," *Journal of Applied Polymer Science*, vol. 123, no. 4, pp. 2187–2193, 2012.

[37] B. Singh, J. P. Singh, A. Kaur, and N. Singh, "Phenolic compounds as beneficial phytochemicals in pomegranate (*Punica*

granatum L.) peel: A review," *Food Chemistry*, vol. 261, pp. 75–86, 2018.

[38] N. Ahmad, S. Sharma, and R. Rai, "Rapid green synthesis of silver and gold nanoparticles using peels of Punica granatum," *Advanced Materials Letters*, vol. 3, no. 5, pp. 376–380, 2012.

[39] H. A. el Rabey, F. M. Almutairi, A. I. Alalawy et al., "Augmented control of drug-resistant *Candida* spp. via fluconazole loading into fungal chitosan nanoparticles," *International Journal of Biological Macromolecules*, vol. 141, pp. 511–516, 2019.

[40] P. Manivasakan, V. Rajendran, P. R. Rauta et al., "Effect of TiO$_2$ nanoparticles on properties of silica refractory," *Journal of the American Ceramic Society*, vol. 93, no. 8, pp. 2236–2243, 2010.

[41] A. Jamil, T. H. Bokhari, T. Javed et al., "Photocatalytic degradation of disperse dye Violet-26 using TiO2 and ZnO nanomaterials and process variable optimization," *Journal of Materials Research and Technology*, vol. 9, no. 1, pp. 1119–1128, 2020.

[42] L. Yang, L. Jiang, D. Hu et al., "Swelling induced regeneration of TiO$_2$-impregnated chitosan adsorbents under visible light," *Carbohydrate Polymer*, vol. 140, pp. 433–441, 2016.

[43] C. Kim, J. Lee, and S. Lee, "TiO$_2$ nanoparticle sorption to sand in the presence of natural organic matter," *Environmental Earth Sciences*, vol. 73, no. 9, pp. 5585–5591, 2015.

[44] C. Botta, J. Labille, M. Auffan et al., "TiO$_2$-based nanoparticles released in water from commercialized sunscreens in a life-cycle perspective: structures and quantities," *Environmental Pollution*, vol. 159, no. 6, pp. 1543–1550, 2011.

[45] S. Jeon, E. Kim, J. Lee, and S. Lee, "Potential risks of TiO2 and ZnO nanoparticles released from sunscreens into outdoor swimming pools," *Journal of Hazardous Materials*, vol. 317, no. 5, pp. 312–318, 2016.

[46] S. Compant, A. Samad, H. Faist, and A. Sessitsch, "A review on the plant microbiome: ecology, functions, and emerging trends in microbial application," *Journal of Advanced Research*, vol. 19, pp. 29–37, 2019.

[47] D. J. Burke, N. Pietrasiak, S. F. Situ et al., "Iron oxide and titanium dioxide nanoparticle effects on plant performance and root associated microbes," *International Journal of Molecular Sciences*, vol. 16, no. 10, pp. 23630–23650, 2015.

[48] I. Kustiningsih, A. Ridwan, D. Abriyani, M. Syairazy, T. Kurniawan, and D. R. Barleany, "Development of chitosan-TiO$_2$ nanocomposite for packaging film and its ability to inactive Staphylococcus aureus," *Oriental Journal of Chemistry*, vol. 35, no. 3, pp. 1132–1137, 2019.

[49] N. Nakayama and T. Hayashi, "Preparation and characterization of poly(L-lactic acid)/TiO$_2$ nanoparticle nanocomposite films with high transparency and efficient photodegradability," *Polymer Degradation and Stability*, vol. 92, no. 7, pp. 1255–1264, 2007.

[50] L. Bellani, G. Siracusa, L. Giorgetti et al., "TiO$_2$ nanoparticles in a biosolid-amended soil and their implication in soil nutrients, microorganisms and *Pisum sativum* nutrition," *Ecotoxicology and Environmental Safety*, vol. 190, article 110095, 2020.

Research Article

Study on Thermal Behavior of Some Biocompatible and Biodegradable Materials Based on Plasticized PLA, Chitosan, and Rosemary Ethanolic Extract

Cornelia Vasile [iD],[1] **Niţă Tudorachi** [iD],[1] **Traian Zaharescu,**[2] **Raluca Nicoleta Darie-Nita** [iD],[1] **and Catalina Natalia Cheaburu-Yilmaz** [iD][1]

[1]*Department of Physical Chemistry of Polymers, "Petru Poni" Institute of Macromolecular Chemistry, 41A Gr. Ghica Voda Alley, 700487 Iasi, Romania*
[2]*National Institute for Electrical Engineering (INCDIE ICPE CA), 313 Splaiul Unirii, P.O. Box 149, 030138 Bucharest, Romania*

Correspondence should be addressed to Cornelia Vasile; cvasile@icmpp.ro and Raluca Nicoleta Darie-Nita; darier@icmpp.ro

Thermal characterization of some multifunctional environmentally friendly materials based on plasticized poly (lactic acid) (PLA)/chitosan (CS) and rosemary extract (R) previously obtained is presented. Differential scanning calorimetry (DSC) associated with other complex investigations such as chemiluminescence and coupled thermogravimetry (TG)/Fourier-transform infrared spectroscopy (FT-IR)/mass spectroscopy (MS) was performed in order to test both the thermal behavior and the biocomposition–property relationship. It was established that the rosemary ethanolic extract offers an efficient protection against thermoxidative degradation to the new developed plasticized PLA-based biocomposites which show good thermal properties, being suitable for both medical and food packaging applications.

1. Introduction

The green and biodegradable composites are interesting materials for environmental-friendly food packaging and biomedical fields.

However, biodegradable polymers cannot be widely used because of their high prices, low thermostability, and mechanical properties [1]. Among the biodegradable polymers, poly (lactic acid) (PLA) is a reliable alternative, being a biobased material with good clarity, high strength, and moderate barrier properties. PLA has biodegradability and annually renewable availability and can be processed by standard melt processes such as injection moulding, film blowing, or melt spinning [1]. Industrial implementation of PLA-based materials is impeded due to its low thermal stability, sensitivity to hydrolysis, low crystallization rate, and high brittleness. PLA is degraded during thermal processing or under hydrolytic conditions, resulting in rapid reduction of molecular weight that affects the final properties of the materials [2, 3]. Most

reported data indicates that its thermal degradation occurs either by a random main-chain scission reaction [4], as well as by depolymerization, oxidative degradation, and transesterification reactions [5, 6] The reaction was found under these experimental conditions to be of first order with an activation energy of 94.0 and 105.3 kJ/mole and preexponential factor 6.43×10^5 and $1.91 \times 10^6\, s^{-1}$, respectively [7]. Moreover, reactive end groups, residual catalyst, unreacted starting monomer, and other impurities may influence the PLA thermal degradation [5] Many efforts were made to suppress polymer degradation in the melt [8] or to accelerate degradation of worn-out PLA-based products/waste. Its serious drawbacks consist of low deformation at break but with high modulus and low heat resistance. PLA has very low crystallinity, leading to inferior thermostability problems during its long service life [9–12]. Therefore, some properties required to be improved. Different solutions have been tested to overcome them making PLA suitable for competing against oil derivative polymers. PLA needs to be modified to improve

its processing or material properties. Several heat resistance modification methods have been applied, such as nucleating agent addition, fiber reinforcement, compounding, blending, stereoisomer complexation, copolymerization, chemical modification, and additive incorporation [13, 14].

The additives (nucleating agents, natural additives, stabilizers, etc.) when used in a concentration range between 1 and 5 wt% have no effects on film transparency. At loadings between 20 and 30 wt%, the filler acts as a nucleating agent promoting the development of crystallinity.

The most practical method to obtain soft, flexible, and ductile characteristics and inherent thermal stability of PLA is its blending with various plasticizers (e.g., esters, tributyl ortho-acetyl citrate, tributyl citrate, triacetin (triglyceride 1,2,3-triacetoxypropane), polyethylene glycol (PEG), di (ethyl-hexyl phthalate, tricresyl phosphate or triisooctyl trimellitate, and butyl benzoate) [15–17]. It was found that the plasticized PLA with tributyl o-acetyl citrate (ATBC) reduced brittlenes of PLA; the sheets and films obtained from plasticized PLA/CS biocomposites have satisfactory transparence and mechanical and improved thermal properties [18–20]. Good results were also obtained when plastifying PLA by using PLA oligomer, l-lactide, poly (ethylene glycol), and epoxidized soybean oil. Epoxidized soybean oil significantly increased the elongation at break and reduced the glass transition temperature because of the changes in chain mobility [21]. Some blends (PLA/ATBC, PLA/polyester bioplasticizer as LAPOL108, and PLA/tributyl citrate plasticizer TBC) present an increase in crystallinity degree value. The same changes are found for the PLA/PEG blend in accordance with the results given in literature [22].

The PLA formulations offering satisfactory properties of materials can be accomplished by the addition of various additives able to improve the features of basic polymer.

Chitosan (CS) biopolymer exhibits outstanding properties as biocompatibility and biodegradability being a relevant candidate in the field of biomaterials [23] It was approved by the Food and Drug Administration (FDA) for use in wound dressings [24] and food packaging. The development of new biodegradable packaging materials, such as PLA/CS films, could be an interesting alternative to change PLA properties.

Some naturally occurring compounds can delay oxidative deterioration of contacting food products, maintaining their nutritional quality and also improving oxidative stability of other types of materials. As an example, the natural antioxidants from a certain extract from herbs and spices such as rosmarinic acid from rosemary, thymol from oregano, eugenol from clove, and curcumin from turmeric are rich in polyphenolic compounds that provide long-term oxidative stability as well as offer additional health benefits [19, 25]. High antioxidative capacity and phenolics of herbs and spices could potentially substitute synthetic antioxidants such as butylated hydroxytoluene (BHT), butylated hydroxyanisole (BHA), propyl gallate (PG), octyl gallate, and tert-butylated hydroquinone (TBHQ) in the food system. Moreover, the synthetic antioxidants are thermally unstable and decompose at higher temperatures. In the food industry, widely apply cooking methods such as baking, frying, boiling, and roasting use high temperature that may also degrade herbs and spices

and diminish their antioxidative capacity. However, these kinds of natural additives have been scarcely studied [26]. The impact of temperature on total antioxidant capacity of various herbs and spices such as cinnamon, clove, nutmeg, mace, oregano, rosemary, sage, and turmeric was followed. Tomaino and others [27] and Khatun and others [28] evaluated the antioxidant activity of spices of ethanol extract of cloves, cinnamon, nutmeg, mace, and turmeric, and they found that the thermal treatments may increase the antioxidant activity by releasing bound antioxidants or by the formation of new compounds with antioxidant properties. It was found that the ethanol extracts of cloves, cinnamon, nutmeg, mace, and turmeric showed to have antioxidative potential such as DPPH radical-scavenging and peroxy radical-scavenging activities. This was also proved by other authors by heating several essential oils (clove, cinnamon, nutmeg, oregano, mace, tumeric, etc.) [26].

The degradation rates can be controlled by blending PLA with additives, inorganic fillers, and nanoparticles, although other factors determine degradation of PLA-based materials such as manufacture procedures, outer service, and environmental conditions. The control of the PLA degradation is mandatory for both medical applications and for the plastic industry. The mechanism as well as the rate of degradation reaction for PLA-based materials seems to be affected by a wide variety of compositional and property variables. Therefore, the assessment of the thermal behavior of all kinds of new materials with application in medical and food industry field is an important requirement. To obtain PLA-based materials with special properties such as antioxidant and antimicrobial activities and biocompatibility, with wide applications both in medical field and food preservation, much complex formulations should be used. Incorporation of CS and rosemary extract into plasticized PLA led to materials possessing such multifunctional properties [29].

The thermal behavior of some biocomposites based on plasticized PLA containing CS and rosemary ethanolic extract is presented in this study by applying differential scanning calorimetry (DSC), chemiluminescence method (CL), and coupled thermogravimetry (TG)/Fourier-transform infrared spectroscopy (FT-IR)/mass spectroscopy (MS). By applying these coupled methods of investigation, the composition–property relationship for the developed biocomposites was establish. It has been found that the addition of CS shifted the glass transition temperature (T_g) to slightly higher values while the cold crystallization temperature (T_{cc}) of PLA-based biocomposites to lower values. It was explained by the effect of CS which is able to promote the crystallization of PLA, leading to an increased crystallization degree of the biocomposites in respect with that of plasticized PLA, because the melting heat takes higher values for biocomposites with increased CS content. The results of the chemiluminescence study proved that the rosemary ethanolic extract is a good stabilizer for thermoxidative degradation of PLA. The PLA/PEG/6CS and PLA/PEG/CS/R biocomposites show the highest characteristic temperature values and apparent activation energy of decomposition. It was concluded that the plasticized PLA/CS/R materials show good thermal properties and most of thermal degradation

products are nontoxic being recommended for both medical and food packaging applications.

2. Experimental

2.1. Materials. Poly (lactic acid) (PLA) (trade name: PLA 2002D) from NatureWorks LLC, UK, with a melt flow index of 5-7 g/10 min (conditions, 210°C/2.16 kg) and a content of 96% L-lactide and isomer D 4%, was used. Average molecular weight determined by GPC was 4475 kDa. According to the literature data, it has a density of 1.25 g/cm^3, melting point of 152°C, and glass transition temperature of 58°C; the crystallinity depends on isomer content and thermal history; water permeability at 25°C is 172 g/m^2 per day; and percentage of biodegradation/mineralization is 100%.

Chitosan (CS) with 200-800 cP viscosity in 1% acetic acid, 75-85% deacetylation degree, and MW $= 190 - 300$ kDa was provided and used as received from Sigma-Aldrich.

Rosemary extract (R) in powder form was obtained following a previously reported procedure by the solvent extraction method in a Soxhlet unit [30]. Rosemary leaves were collected from local farms, dried at ambient temperature, and subsequently milled (Laboratory of Radiation Chemistry, INCDIE-ICPE CA, Bucharest, Romania). Ethanol was used as an extraction solvent. After collection of the rosemary extract in an ethanol solution, the powder was separated by precipitation induced by the addition of water. The insoluble material was filtered and washed with acetone until it was dried. The extract was further dried under vacuum at ambient temperature. A greenish-yellow fine powder was obtained and stored in desiccators to avoid the absorption of moisture. Its main components are carnosol and carnosic acid which show in the UV spectra a λ_{max} around 283 and 246 nm, while for rosmarinic acid, absorbances at 230, 270, 280, and 330 nm were obtained [31]. Its amount of total phenols was of 112.5 mg GAE (gallic acid equivalent)/g dw (dry weight), while the total flavonoid content was of 261.5 (mg QE (quercetin equivalents)/g dw) [25]. The present study intended to evidence its effect on plasticized PLA together with chitosan on the thermal behavior of some biocomposites.

Poly (ethylene glycol) (PEG) BioUltra 4.000 (Sigma-Aldrich) was used as plasticizer.

PLA-based biocomposites were prepared using different amounts of chitosan or/and rosemary extract by incorporating them into PLA matrix in a melt state using a fully automated laboratory Brabender station (Brabender® Plasti-Corder® Lab-Station EC, Brabender GmbH & Co. KG, Duisburg, Germany). The processing temperature was 165°C for 10 min, at a rotor speed of 60 rpm. The PLA/PEG/rosemary/chitosan biocomposite systems prepared contained 20 wt% PEG, 3 and 6 wt% CS, and 0.5 wt% rosemary ethanolic extract (R). More details on characteristics/properties of the biocomposites studied and their preparation are found in a previous paper [29].

2.2. Investigation Methods

2.2.1. Differential Scanning Calorimetry (DSC). A TA Instrument Q20 Differential Scanning Calorimeter (New Castle, DE, USA) was employed for the thermal characterization,

sample amount being of ~10 mg. All of the samples were cooled down to 0°C and heated up to 250°C, so below and above materials expected glass transition and melting temperature. After first heating run, all samples were kept for 2 min at 250°C and then cooled down to 0°C with a cooling rate of 5°C/min and heated again for a second run up to 250°C with a heating rate of 10°C/min. An empty crucible was used as reference. All measurements were performed under nitrogen atmosphere. The degree of crystallinity (X_c) of the PLA and its composites was calculated by dividing the melting enthalpy of the sample by $\Delta H^o_m = 93.7$ J/g [32, 33], which is equilibrium enthalpy of a PLA sample with 100% crystallinity. An overall accuracy of ±0.5°C in temperature and ±1% in enthalpy was estimated. The final results are the average of three recordings.

2.2.2. Chemiluminescence (CL). The LUMIPOL 3 unit (SAS, Bratislava, Slovakia) chemiluminescence spectrometer was used in the recording of nonisothermal emission intensity dependencies on temperature on film samples with small weights not exceeding 5 mg. The selected temperature range starts from room temperature being ended at 250°C. The measured temperatures had a low error (±0.5°C). Heating rates were 2, 3.7, 5, and 10°C min^{-1}. CL determinations were carried out in air under static conditions. The CL intensity values are normalized to sample mass for their reliable comparison. The activation energy of the oxidation process was determined by the Kissinger method [34–37].

2.2.3. Coupled Thermogravimetry/Fourier-Transform Infrared Spectroscopy/Mass Spectroscopy (TG/FTIR/MS). Thermal degradation was followed by simultaneous TG/FTIR/MS thermal analyses. The thermal study was performed on a STA 449 F1 Jupiter apparatus (Netzsch STA 44F1, Germany). The heating program started from 30°C up to 600°C at a 10°C min^{-1} heating rate, under nitrogen as a purge and protective gas for a flow rate of 40 ml/min. The temperature reproducibility of TG was ±2°C, and the nonvolatile fraction was ±3%. The thermobalance was coupled with a Vertex 70 IR spectrophotometer and an Aeolos QMS 403C mass spectrometer (Netzsch, Germany) for *in situ* recording of the spectral characteristics of the degradation gaseous products. For each recording, 12-15 mg of sample was placed in Al$_2$O$_3$ crucible. Temperature calibration was done with standard indium, zinc, tin, bismuth, and aluminum of 99.99% purity. Volatile degradation products in a temperature-controlled environment were directly transferred both to an electron impact ion source of a mass spectrometer QMS 403C Aeolos (Netzsch, Germany) type and to an infrared (FTIR) spectrometer (Bruker, Germany), via a heated capillary tube, and analyzed by *in situ* vapor phase FTIR. Transfer of the degradation gaseous products was realized through two isothermal lines.

3. Results and Discussion

3.1. DSC Results. DSC measurements on plasticized PLA-based biocomposites were carried out both by heating and cooling. The thermal properties of these materials, such as

glass transition temperature (T_g), crystallization temperature (T_c), cold crystallization temperature (T_{cc}), melting temperature (T_m), crystallization enthalpy (ΔH_c), melting enthalpy (ΔH_m), and crystallinity degree (X_c), were evaluated. The DSC curves of the studied biocomposites containing CS and 0.5% R comparatively with those of PEG-plasticized PLA are presented in Figure 1, and the results are summarized in Table 1.

In the DSC curves, glass transition and melting processes were clearly evidenced. In the 45-65°C range, both glass transition of PLA and melting of PEG 4000 [38] can occur, the DSC curves showing two processes with the second one at about 60°C for most biocomposites with the exception of PLA/PEG/6CS/0.5R which show only one temperature indicating a good dispersion of components in a PLA-based matrix. The first peak is placed at lower temperature around 50°C and could be assigned to PEG melting taking into consideration literature data. The intense crystallization peaks have been found for PEG of 4000 and 20,000 g/mol located on 38 and 44°C, [39], respectively, while in the DSC curve of the PLA/PEG sample, the crystallization peak is not obvious in the temperature range, but a T_g transition can be noticed. The behavior proved that the PEG is a typical crystalline polymer and the PLA is a semicrystalline polymer with slow rate of crystallization.

Melting process occurs in 153-157°C and also shows a small premelting peak at 145°C. The cold crystallization process can be easily observed only for PLA/PEG/0.5R and PLA/PEG/3CS/0.5R biocomposites in the first heating run between 90 and 92°C (Figure 1(a)), while in the second run, this process is present for almost all samples, excepting those with high CS content (Figure 1(b)). Incorporation of a bioactive plasticizer such as PEG led to a decrease of glass transition temperature (from $T_g = 66$°C for PLA to 50-60°C for plasticized systems) because of the increase of PLA chain mobility. Other thermal characteristics remain unchanged. All values are similar with those reported in literature [40–42] and in our previous paper for PLA plasticized with ATBC [20].

Some authors found differences in thermal behavior in respect with PLA containing essential oils (EOs). It was found that both PEG and EOs led to the formation of flexible PLA/PEG/EO films with significant drop in the glass transition temperature (T_g) and mechanical property [43]. The lower enthalpy values for the melt crystallization could be affected by evaporation or degradation of essential oils. A change in thermal properties of PLA indicates the extent of the plasticizing effect provided by EOs, and those decreases could be ascribed to the increase in the chain mobility of polymer matrix. A similar drop in thermal properties has been reported for thymol and cinnamaldehyde-enriched PLA films [44, 45]. Kamthai and Magaraphan studied the PLA/bagasse carboxymethyl cellulose composites and found that the increment of isosorbide diester plasticizer concentration decreased glass transition, melting, and decomposition temperatures, as well as the reduction of storage modulus, while their elongation was significantly improved with increasing plasticizer content. The results were explained by the synergistic effect of the isosorbide diesters which caused a lowering Tg (acting as a lubricant) and an increase of the

chain mobility at low temperature, but they also induced a cold crystallization acting as nucleating agents. The melting temperature Tm was reduced. The composite with 15 wt% isosorbide diesters showed higher T_m, so at this concentration, the system showed a better thermal stability than the others [41, 42].

The addition of chitosan into plasticized PLA increased the X_c up to ~26-29% especially at low CS amount (~3 wt%) when compared with the samples without CS and with PEG-plasticized PLA (X_c of 25%) (see Table 1 and ref. 29). The increase in the crystallinity degree has a decrease effect of impact strength [16, 18].

In the present study, the addition of CS to PLA-based systems shifted the T_g to slightly higher values while the cold crystallization to lower temperatures showing that the CS can promote the crystallization of PLA. This is in accordance with results of other authors who also found that chitosan acts as a nucleating agent, promoting a faster crystallization of PLA. A significant improvement in tensile, flexural, and impact strength of the hybrid composites was observed as the weight percentage of Basalt Fiber (BF) and CS increases. Glass transition temperature (T_g) and percentage of crystallinity (X_c) increase, as weight percentage of BF (25%) and CS (10%) increases as showed by DSC measurements [46]. When recording the DSC curves by cooling (not shown), a crystallization temperature was found occurring between 70 and 80°C, whose values increased with increasing CS content of the biocomposites. This could be due to the restriction in chain reorganization in CS presence, probably because of phase separation. PEG is a typical low molecule polymeric plasticizer. It is recognized as the most studied promoter for PLA, manifesting the desirable compatibility with PLA even at the loading up to 30 wt%. The enhancement of the growth rate of PLA spherulites by the presence of PEG is well documented [47]. Lai et al. [48] found that its action as nucleation agent and promoter may dramatically improve the crystallization kinetics of the polymer matrix.

3.2. Chemiluminescence. The properties of polymer blends/biocomposites reflect usually the contribution of components. When oxidation is the discussed process, the results depend of the mechanistic features of interphase interactions. The thermal stability of PEG-plasticized PLA-based systems is characterized by analogous aspects which gather the present nonisothermal chemiluminescence spectra in two groups (Figure 2). The presence of shoulders was observed at two different temperatures: 150°C for the samples containing CS and control (PLA/PEG) and 175°C for the samples, where rosemary acts as a stabilizer agent. This shift could have occurred due to the protection activity of active components of natural extract on the decomposition of hydroperoxides.

The progress of degradation is much clear at a moderate heating rate of 5°C/min. The unrestricted propagation of oxidation is observed at 225°C with a maximum CL emission. The T_{CLmax} is modified for samples containing rosemary extract because it delayed the oxidation process. This is also proved by a slight increase in the activation energy values of R-containing samples (Table 2) because it stimulates the blocking action of the peroxyl radical oxidation. This delay

(a)

(b)
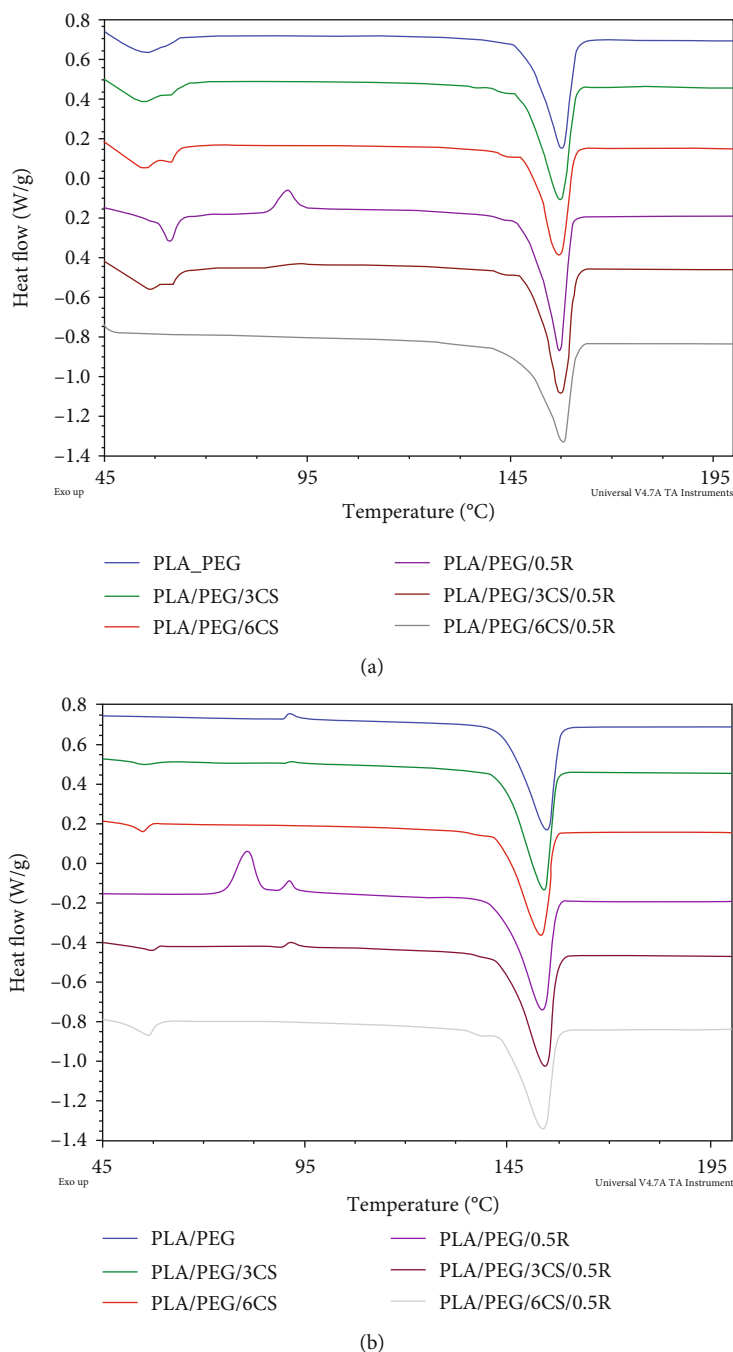
FIGURE 1: DSC curves of plasticized PLA, PLA/PEG/R, and PLA/PEG/CS/R biocomposites, recorded in the first heating run (a) and the second heating run (b).

is explained by the scavenging activity of the phenolic components of R on the free radicals sprung by fragmentation of polymer backbones. While PLA generates radicals by the cleavage of ester units [49], PEG is scissored on the ethylene oxide sites [50]. The contributions of the two components are difficult to be individually evaluated because the oxidation occurs randomly even though rosemary protector is active. However, a prominent CL peak is present in the PLA/PEG blend, which allows supposing that R has a concealing action on the main biocomposite component.

If the thermal behaviors based on activation energy of the PLA/PEG/CS and PLA/PEG compositions are compared, the improvement in the thermal stability of the former blend can be noticed. The temperature shift toward greater values when chitosan and rosemary are present is a confirmation of their collaboration in the propagation steps of oxidation.

The values of onset oxidation temperature follow some certain tendencies (Table 2 and Figure 3). The CS at low concentration decreases the OOT values especially at small heating rates but a tendency to increase it was found at higher

TABLE 1: Thermal characteristics of the plasticized PLA/PEG/CS/R systems determined by the DSC method.

Sample	T_g (°C)	T_{cc} (°C)	ΔH_{cc} (J/g)	T_m (°C)	ΔH_m (J/g)	T_{cr} (°C)	Crystallinity degree X (%)
For the first heating run							
PLA/PEG	49.3; 54.1	—	—	157.7	23.8	70.0	25.1
PLA/PEG/3CS	49.2	—	—	157.4	27.9	73.1	29.8
PLA/PEG/6CS	50.1; 60.8	—	—	157.0	24.9	77.8	26.6
PLA/PEG/0.5R	53.6; 60.2	90.2	2.6	157.1	26.1	66.7	27.9
PLA/PEG/3CS/0.5R	50.5; 60.8	92.5	—	157.3	26.4	70.7	28.2
PLA/PEG/6CS/0.5R	—	—	—	157.9	26.2	80.5	27.9
For the second heating run							
PLA/PEG	—	91.4	0.36	154.7	25.3	—	27.0
PLA/PEG/3CS	53.8	91.6	—	153.8	27.8	—	29.7
PLA/PEG/6CS	52.7	—	—	153.3	25.4	—	27.1
PLA/PEG/0.5R	—	80.9	8.00	153.7	27.3	—	29.1
PLA/PEG/3CS/0.5R	54.6	91.6	0.34	154.3	27.6	—	29.5
PLA/PEG/6CS/0.5R	52.3	—	—	153.6	26.7	—	28.5

Glass transition (T_g), cold crystallization (T_{cc}), melting (T_m), and crystallization (T_{cr}) temperatures; cold crystallization (ΔH_{cc}) and melting (ΔH_m) enthalpies; crystallinity degree (X).

heating rates. The presence of rosemary has an unexpected decreasing effect. This apparent behavior is conducted by the degradation of PLA, which takes place in two stages: a decomposition process and an oxidation in the bulk. As it is shown in Figure 2, the generation of hydroperoxides is notified by an oxidation peak. Furthermore, the increase in the concentration of CS leads to a disappearance of this CL emission shoulder followed by a significant increase of OOT (Figure 3). The highest OOT values are found for PLA/PEG/6CS and PLA/PEG/6CS/R biocomposites (Figure 3(b)). For each sample, OOT increases with increasing heating rate that may be the consequence of the increase of thermal movement of structural entities, especially small scission moieties.

Two mechanistic details can be analyzed: the small fragments from PLA consume a part of rosemary and the protector role of the last involved in the oxidation inhibition of primary large radicals. The increase of temperature does not make a difference between the various coexisting intermediates. The competition for rosemary in the blocking radicals generated by blending components determines higher values of activation energies. This feature is realistically based on the easier access of small fragments for the stabilization action instead of the inactivation of former radicals with larger chain configuration.

The thermal degradation of biocomposite components, PLA and PEG, occurs by macromolecule decomposition. The fragmentation of PLA and PEG chains is the main process through which these polymers are degraded. The formation of formic esters from PEG [50] and lactides from PLA [49] describes the sharp decrease in their molecular weights. According with previous results on the activation energy values required for the thermal degradation of PLA [51], the present data (Table 2) are placed on the lower limit. Other estimations reported various values that depend on the chosen method [52, 53]. Indeed, the sample composition plays a key role in the energetic characterization of degradation process.

On the beginning of oxidation, first 10 minutes, occurring in PLA/PEG blends, the evolution of degradation takes at different places if rosemary is present or not (Figure 4).

The dropping of the CL intensities in the samples free of rosemary alcoholic extract explains the lack of any oxidation prevention. The free radicals that appeared during sample preparation are immediately oxidized, and their decay is reflected in the variation of emission intensities. By contrast, the rosemary extract blocks the oxidation of neighboring radicals for a short time on the first minutes. For the two pairs of compositions, the isothermal CL curves drawn in the presence of R are placed under the similar curves recorded on free rosemary samples. It reveals the involvement of natural phenolic antioxidants in the diminution of oxidative ageing of PLA. The further reactions with oxygen will involve the spread of radicals that are formed during thermal testing at 170°C. The amplitudes of increasing CL intensities are higher in respect with the intensities recorded at 10 minutes of heating, in the samples without R. The PLA/PEG sample shows the well-defined maximum emission values after 10 minutes. The next parts of CL spectra start suddenly in the stabilized composition. In the formulation free of R, radicals are available for oxidation describing a pseudoplateau followed by a smooth increase. The pairs consisting of specimens, PLA/PEG/3CS and PLA/PEG/3CS/R, exhibit intensity peaks at 40 and 50 minutes, respectively. The curve slope for rosemary-containing sample decreases more gradually than the curve drawn for unprotected blend. For other pairs, PLA/PEG/6CS and PLA/PEG/6CS/R where the higher content of CS is present, the evolution of CL intensities is slower where R natural protection acts efficiently. These CL results confirm the benefic contribution of R and the degrading trend induced by CS. The biocomposites with PLA as a main phase (matrix) demonstrate that the progress of oxidative degradation requires activation energies not more than 55 kJ mol^{-1}. Because the blends stabilized with R exhibit slightly higher values of apparent activation energy
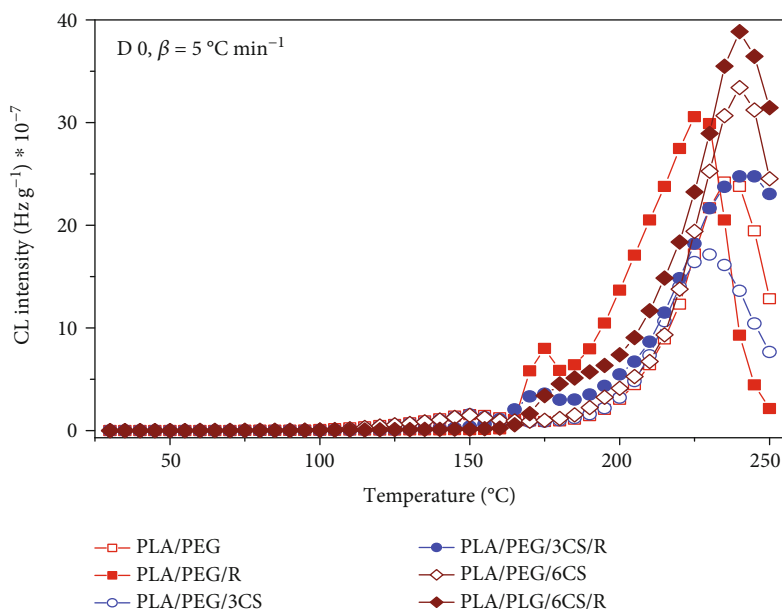
FIGURE 2: The dependence of the CL intensity on temperature for plasticized PLA-based system of various compositions: all samples PLA/PEG and PLA/PEG/CS; PLA/PEG/R and PLA/PEG/CS/R.

TABLE 2: Onset oxidation temperature (OOT) and apparent activation energy (Ea) for the oxidation of the PLA/PEG and PLA/PEG/CS/R biocomposites determined by nonisothermal chemiluminescence method at different heating rates.

Sample	Heating rate ($^\circ$C min^{-1})	OOT ($^\circ$C)	Equation	Correlation coefficient	Ea (kJ mol^{-1})
PLA/PEG	3.7	185	$Y = 2.71 - 6.29\,X$	0.98344	52.54
	5.0	201			
	10.0	218			
	15.0	231			
PLA/PEG/3CS	3.7	179	$Y = 2.55 - 6.14\,X$	0.97148	51.05
	5.0	197			
	10.0	212			
	15.0	225			
PLA/PEG/6CS	3.7	192	$Y = 2.71 - 6.29\,X$	0.98344	52.30
	5.0	208			
	10.0	220			
	15.0	232			
PLA/PEG/R	3.7	182	$Y = 3.15 - 6.38\,X$	0.99378	53.04
	5.0	188			
	10.0	208			
	15.0	225			
PLA/PEG/3CS/R	3.7	180	$Y = 2.95 - 6.33\,X$	0.97528	52.63
	5.0	196			
	10.0	215			
	15.0	223			
PLA/PEG/6CS/R	3.7	192	$Y = 3.40 - 6.65\,X$	0.89551	55.29
	5.0	216			
	10.0	224			
	15.0	245			
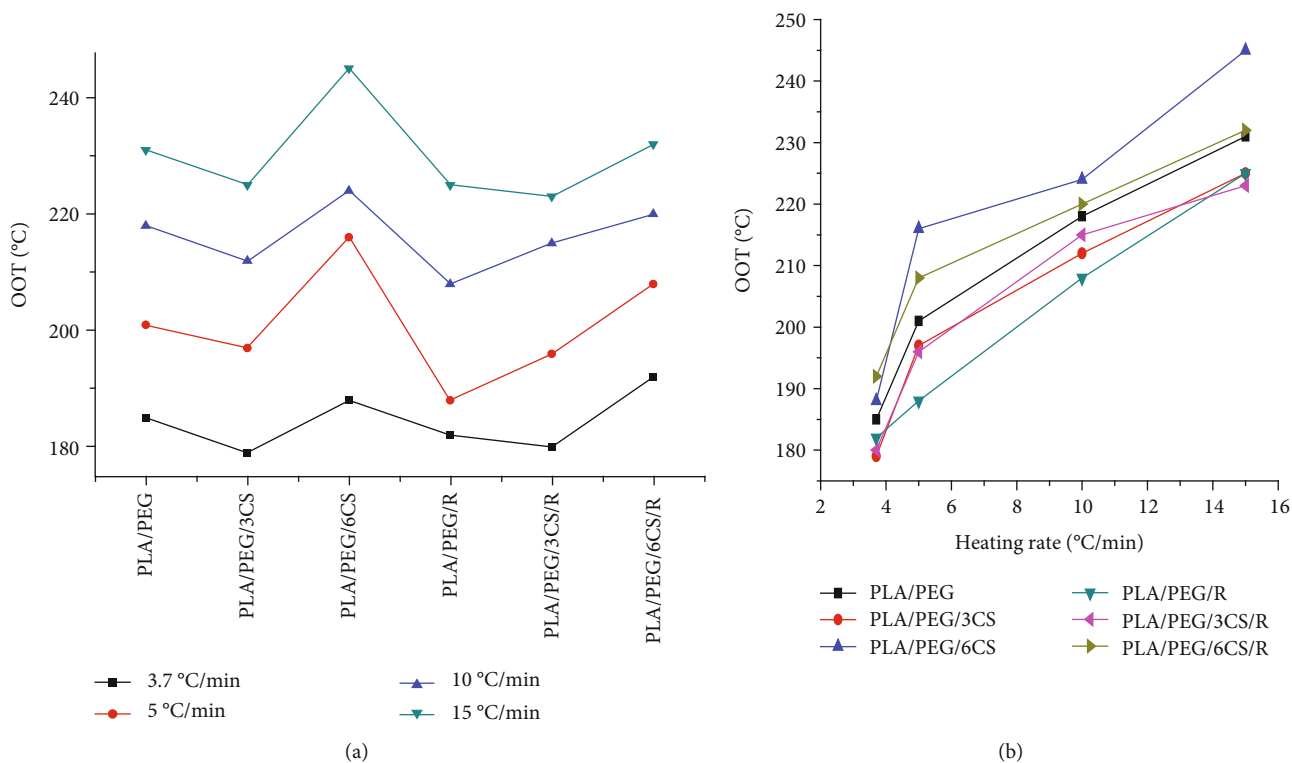
FIGURE 3: Dependence of OOT on sample composition (a) and on heating rates (b).
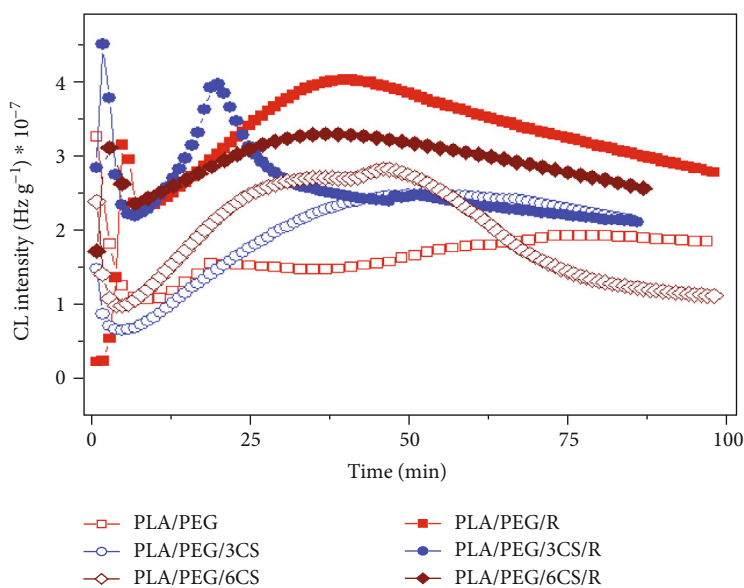
FIGURE 4: CL spectra for plasticized PLA samples of various compositions recorded in isothermal conditions at 170°C.

that there were found for samples free of oxidation protector, the presence of rosemary extract is a reliable solution for the improvement of thermal stability of PLA. It means that only a small part of molecules is converted into peroxyl radicals and the most part of materials is decomposed onto low-weight fragments.

From the data of Table 3, two main features can be envisaged: (1) the activation energies (Ea) required by unstabilized samples are similar with the values found for poly (lactic acid) [51], and (2) because the differences in the activation energies involved in the oxidative degradation of homologous compositions are small, the presence of phenolic components from rosemary extract hinders only the oxidation of scission fragments, the depolymerization being unaffected. Furthermore, the lower contents of chitosan drops smoothly down the value of activation energy due to its concerns in the propagation of oxidation. The oxidative degradation of polymers starts with the scission of weaker bonds and the formation

TABLE 3: TG data for PEG-plasticized PLA containing chitosan and powdered rosemary ethanolic extract.

Sample	Degradation step	T_{onset} (°C)	T_{max} (°C)	ΔW (%)	T_{10} (°C)	T_{20} (°C)	GS (°C)	
	I	276.8	321.4	82.52	285.5	298	334	(337)
PLA/PEG	II	372.2	401.5	16.30			394	(400)
	Residue			1.18				
	I	280.8	325.8	73.72	290.2	294	325	(334)
PLA/PEG/3CS	II	369.2	409.4	20.40				(407)
	Residue			5.88				
	I	285.8	323.3	79.38	292.5	304.5	336	(332)
PLA/PEG/6CS	II	371.1	402	18.48			394	(410)
	Residue			2.14				
	I	284.8	336.4	83.03	294	307.5	348	(342)
PLA/PEG/0.5R	II	375.3	402.8	15.04				(415)
	Residue			1.93				
	I	282.7	329.7	69.15	293.5	312.6	345	(343)
PLA/PEG/3CS/0.5R	II	370.3	395.4	21.36				(399)
	Residue			9.49				
	I	294.7	332.6	79.77	303	314	341	(340)
PLA/PEG/6CS/0.5R	II	377.5	406.1	17.96			406	(410)
	Residue			2.27				

Decomposition temperatures: T_{onset}: onset of decomposition; T_{max}: temperature corresponding to maximum mass loss rate and corresponding to 10% (T_{10}) and 20% (T_{20}) mass loss (ΔW); GS: the temperature at which the maximum amount of gas was released (determined from Gram–Schmidt curves using Proteus software while in brackets are values evaluated from 3D spectra using OPUS programme) from each decomposition step. The accordance of both types of GS values is evident.

of intermediates as the initiators of propagation stages [54]. The formation and the decay of peroxyl radicals are proved by the emission peak appeared in the nonisothermal CL spectra at 150°C and 175°C for the oxidative degradation of samples free of R (Figure 4) and rosemary-protected polymer blends (Figure 4), respectively. This difference is an evident proof of antioxidant activity of rosemary extract by the increasing formation temperature with 25°C, a significant value in the kinetic analysis of the stability of studied systems.

The further reactions involving free radicals (see Scheme 1) follow various routes when the interaction between the entities born from both polymers voids the generation of oxidation products.

The evolution of oxidation depicted by Figure 4 is an additional proof for the stability protection brought about by R. The best example is the pair curves recorded for PLA/PEG/6CS in the presence and free of rosemary extract. The maximum CL intensities are reached after 29 minutes, when the sample is protected, while the unstabilized sample has the corresponding peak after 20 minutes at the same temperature (170°C). Analogous evidences may take into consideration the main role of R in the delay of oxidative degradation of studied blends. The former entities that appeared by molecular chain scissions were presented earlier [55, 56]. They follow different paths by which they are decayed: either the formation of peroxyl intermediates generates stable oxidation products or they interact to each other coupling them in larger structures. The present CL measurements on PLA/PLG blends with and without rosemary suggest the general scheme depicting the degradation of PLA/PEG formulations. Microstructural differences were also described

by other authors studying PLA-b-PEG-b-PLA triblock copolymer [57]. The addition of oxidation protector directs the radicals appearing from both components toward their interaction by intermolecular configurations [58]. The abundances of oxygenated products born by various propagation reactions, like molecular rearrangements or transesterification, are diminished by the presence of R, which provides increasing amounts of lactide and carbonyl derivatives. The most important role of methyl moieties in PLA degradation consists of the involvement of small radicals in the decay of macroradicals [55, 59]. The ESR investigations have stated that the tertiary methyls are easily radiolised explaining the decrease of molecular weight of components.

3.3. TG/DTG/FTIR/MS Study. Thermal stability, including initial decomposition temperature (T_{onset}), temperature of maximum rate of degradation (T_{max}), decomposition temperature at 10% and 20% weight loss (T_{10} and T_{20}), and, respectively, GS temperature—the temperature at which the maximum amount of gas was released (determined from Gram–Schmidt curves using Proteus software) of the PEG-plasticized PLA materials, can be determined by thermogravimetry. The TG/DTG curves of the biocomposites are given in Figures 5(a) and 5(b), while the thermogravimetric data are summarized in Table 3. According to the previous results [25] and literature data [60–65], thermal degradation of PLA is a single-step process involving the nonradical decomposition, radical alkyl-oxygen homolysis, and radical acryl-oxygen homolysis. This polymer material is the precursor to the formation of an intramolecular transesterification, which undergoes ester pyrolysis and unzipping depolymerization
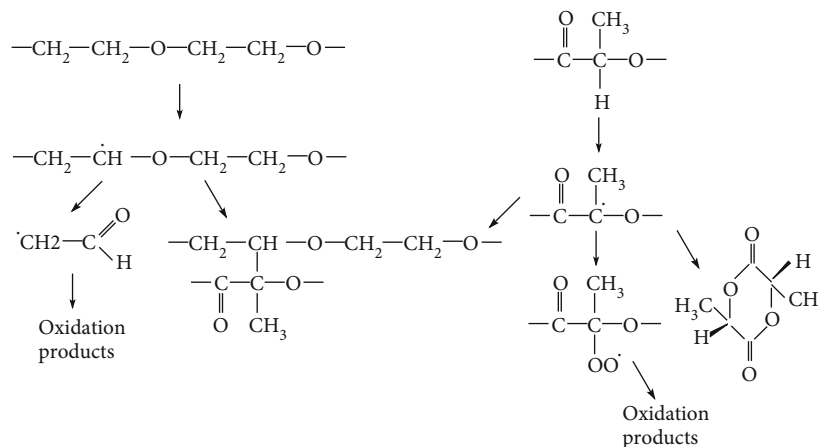
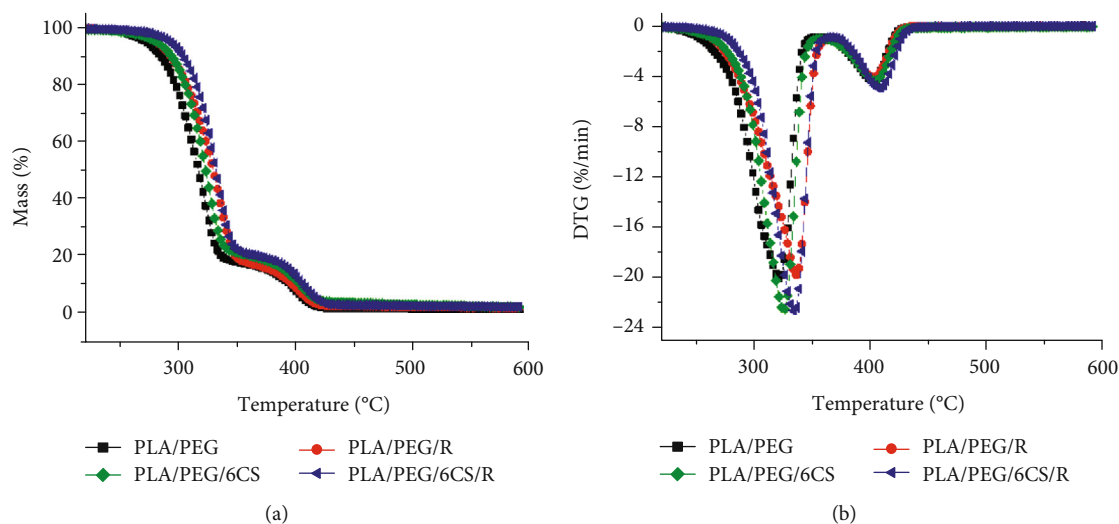SCHEME 1: Oxidative mechanism scheme of PLA/PEG blends.

FIGURE 5: TG (a) and DTG (b) curves for PLA-based blends and biocomposites containing PEG, chitosan, and rosemary ethanolic extract.

random chain scission. The PEG-plasticized PLA decomposes in two steps occurring between 270–375°C and 375–430°C temperature ranges. The decomposition of all other biocomposites is similar with that of plasticized PLA with some particularities offered by each active component chitosan or/and rosemary ethanolic extract. The first step which is the main one occurs with a mass loss (ΔW) of 69-83 wt%, while the second that takes place shows a mass loss of 15-21 wt%. The residue amount is higher after decomposition of the biocomposites containing chitosan, because of the carbonization process occurring in polysaccharides. It can easily be observed from Figures 5(a) and 5(b) that by incorporating both of the CS and rosemary extract, the curves are shifted to higher temperatures proving that the new multicomponent materials are more thermostable than plasticized PLA.

The highest onset (T_{onset}) temperature of decomposition start, maximum (T_{max}) decomposition temperature corresponding to maximum rate of mass loss, GS and decomposition temperatures corresponding to 10 wt% (T_{10}) and 20 wt% (T_{20}) mass loss, respectively, are found for the PLA/PEG/6CS and PLA/PEG/CS/R biocomposites (Table 3). This variation

appears much clearer in Figure 6. This means that in these biocomposites, both bioactive components act synergistically for improving thermal stability of materials. Similar results were found in other papers as for PLA/epoxidized vegetable oils [66]. Other authors found that at temperatures < 250°C, the nanocomposites exhibited good thermal stability and could effectively block about 65% of UVB and UVC irradiation [67]. For other types of materials, the thermal behavior is different. Isosorbide diesters decreased the T_{max} of plasticized PLA/carboxymethyl cellulose (CMCB) composites with the narrow range, i.e., by 10°C. The composite with 20 wt% of plasticizer showed a two-step decomposition; the major decomposition of PLA/CMCB occurs in the temperature range of 250–350°C [41]. In the PLA/5% microcrystalline cellulose (MCC) binary composites, a shift to lower temperatures of about 10°C in T_{max} value was observed, while a decrease of about 25°C was detected for the PLA/5MCC/1Ag ternary composite which indicates that combining the presence of microcrystalline cellulose and silver nanoparticles affects the thermal degradation process. As degradation proceeds, the effect of the hydrogen bonding interactions
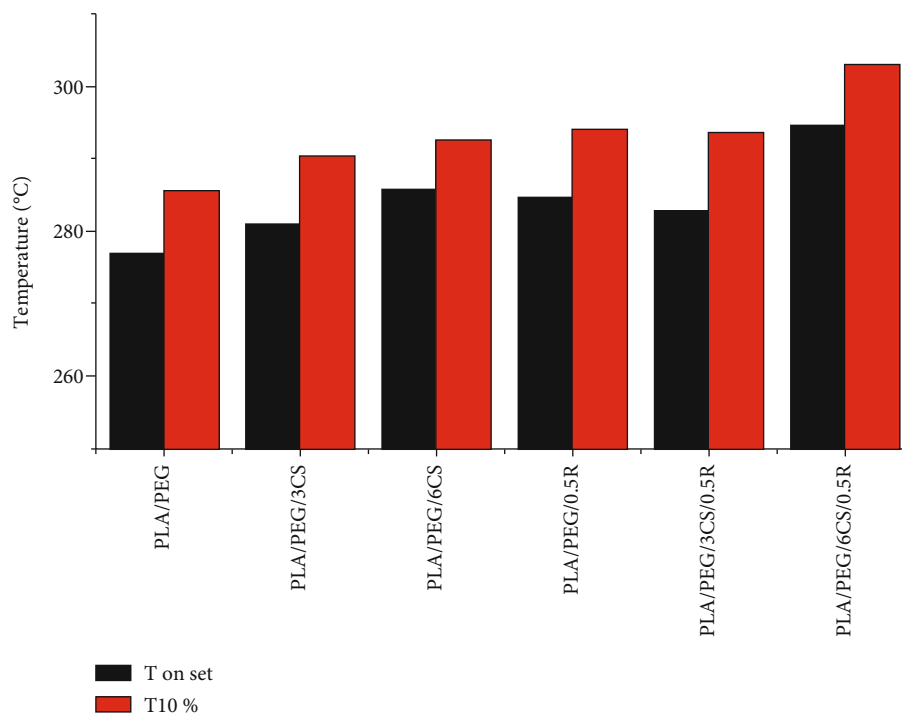
Figure 6: The variation of the T_{onset} and T_{10} with the composition of PEG-plasticized PLA biocomposite.

decreases, but char and gases evolved from cellulose degradation may interact with solid PLA [68].

The processing of thermogravimetric data obtained after thermal degradation was performed using the "Thermokinetics-3" software (Netzsch "Thermokinetics-3," version 2008.05). By using 18 different reaction models included in the software, the multiple linear regression (MLR) method allows the obtaining of the most probable kinetic model, describing each thermal degradation step through a comparison between recorded nonisothermal experimental data and calculated data.

The conversion equations $f(\alpha)$ that used one single-step model are shown below:

Reaction order nth model, sFn:

$$f(\alpha) = (1 - \alpha)^n, \tag{1}$$

where n is the reaction order and α is conversion degree.

nth reaction order of the autocatalytic model, CnB:

$$f(\alpha) = (1 - \alpha)^n (1 + K_{cat} \cdot \alpha). \tag{2}$$

K_{cat} is the autocatalytic constant, n is the reaction order, and α is conversion degree.

As it can be seen from the data of Table 4, the sCnB model is characteristic for both the degradation steps of most samples excepting the first one of PLA/PEG/0.5R and PLA/-PEG/3CS, while the sFn model describes thermal degradation of PLA/PEG/0.5R both steps, the second step of the PLA/PEG degradation and the first one of PLA/PEG/3CS and PLA/PEG/3CS/0.5R samples. The nth model, sFn, is commonly used to check the mechanism of polymer decomposition [69]. It was demonstrated that the autocatalytic

degradation mechanism may lead to acceleration of degradation. The autocatalysis manifests in nonmonotonicity of the conversion function, and it has a complex role in the PLGA erosion that leads to size-dependent heterogeneities for uniformly bulk-eroding polymer microspheres [70, 71]. However, in the present study, the autocatalytic constant (K_{cat}) took small values. The variation of the apparent activation energy for both decomposition steps (and also corresponding preexponential factor) of thermal degradation on the composition of the PEG-plasticized PLA-based materials is similar with that of characteristic temperatures (Figure 7). The highest E values were found for PLA/PEG/6CS/0.5R biocomposite which should be the most thermally stable one.

The values reported in literature for kinetic parameters of decomposition of systems containing PLA differ in respect with experimental conditions used and evaluation method applied. Yang and Lin [7] found the decomposition reaction of PLA to be of first order with an apparent activation energy of 94.0 and 105.3 kJ mole^{-1} and pre-exponential factor 6.43 × 10^5 s^{-1} and 1.91 × 10^6 s^{-1}, respectively. McNeil and Leiper reported that the pyrolysis was a first-order reaction kinetic equation, the apparent activation energy as 119 kJ mole^{-1} [71, 72]. Aoyagi et al. also reported a complex change in the activation energy value of 80–160 kJ mole^{-1} [73]. Sivalingam and Madras investigated the thermal degradation of PLA both under conditions of dynamic and isothermal heating. They reported that the apparent activation energies of pyrolysis were 42.7 and 105.4 kJ mole^{-1} for the random chain scission and the specific chain scission for the dynamic heating by using the Friedman analytical method and 92.9 kJ mole^{-1} for isothermal conditions of heating, respectively [74]. These values are enough similar with ours taking into consideration the differences between experimental conditions.

TABLE 4: Kinetic parameters obtained by the multiple linear regression (MLR) method.

Sample	Temperature range (°C)	Reaction type	Ea (kJ mol^{-1})	Log A (s^{-1})	Reaction order	Log K_{cat}	Correl coeff.
PLA/PEG	250-350	sCnB	143	10.44	0.93	-0.110	0.9999
	350-450	sFn	130	7.82	0.39	—	0.9977
PLA/PEG/3CS	250-340	sFn	138	11.59	2.58	—	0.9984
	340-480	sCnB	134	8.43	2.30	0.176	0.9947
PLA/PEG/6CS	250-350	sCnB	143	10.29	0.93	0.284	0.9999
	340-480	sCnB	138	8.49	0.80	-0.542	0.9978
PLA/PEG/0.5R	250-350	sFn	132	9.25	0.53	—	0.9999
	350-450	sFn	132	7.97	0.42	—	0.9990
PLA/PEG/3CS/0.5R	220-350	sFn	145	12.04	1.28		0.9986
	350-470	sCnB	152	9.29	1.90	1.147	0.9985
PLA/PEG/6CS/0.5R	250-350	sCnB	178	13.34	0.79	-0.244	0.9999
	350-480	sCnB	159	9.89	0.81	0.045	0.9992

"s" indicates that the thermal degradation takes place in one step, and Fn and CnB represent the single reaction model involved in the thermal degradation process. Ea: apparent activation energy; A: preexponential factor.
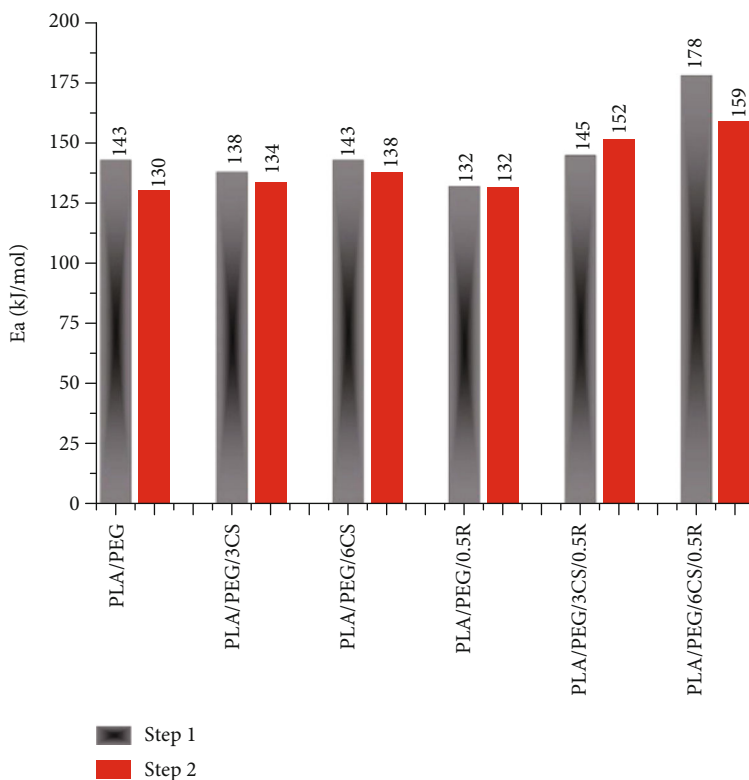

FIGURE 7: Dependence on composition of the apparent activation energy of the first and second step of the thermal decomposition of PEG-plasticized PLA-based samples.

Nonisothermal degradation kinetics, proposed by Kissinger, Kissinger-Akahira-Sunose, Flynn-Wall-Ozawa, and Augis and Bennett models, are utilized to estimate the activation energies (Ea) for PLA, which were found to be 254.1, 260.2, 257.0, and 259.1 kJ mol^{-1}, respectively. The reduced Ea values of bionanocomposite films may be elucidated by intermolecular distance and enrichment in chain mobility. The evolved gaseous products like hydrocarbons, carbon dioxide, carbon monoxide, and cyclic oligomers are successfully identified with TG-FTIR analysis [75].

3D FTIR spectra of the decomposition products give some information about the change in their composition after incorporation of CS and R. From the data presented in Figure 8, it is evident that the FTIR spectra show difference both in the intensity of the bands and also in the number of bands. The spectra of the products from decomposition of the biocomposites containing CS are much complex in 2000-3000 cm^{-1}, and the main bands appear at higher temperatures.

The 2D FTIR spectra of the degradation products of the plasticized PLA-based biocomposites taken at both GS

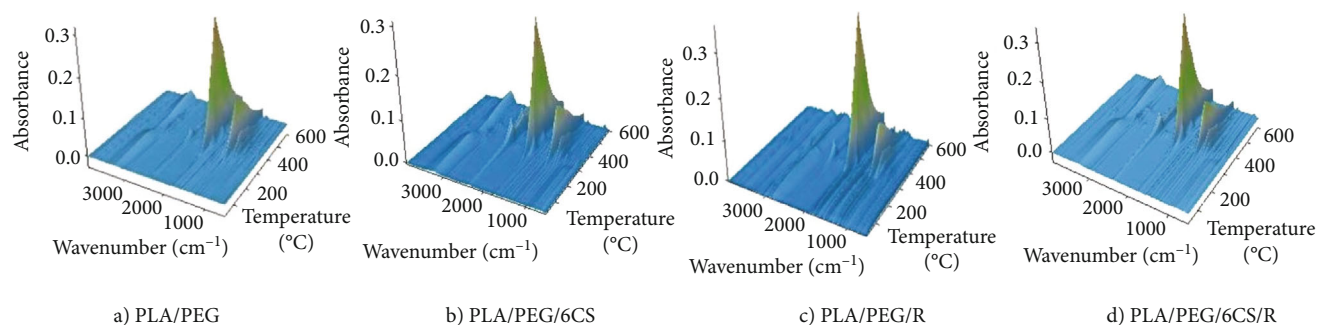a) PLA/PEG   b) PLA/PEG/6CS   c) PLA/PEG/R   d) PLA/PEG/6CS/R

FIGURE 8: 3D FTIR spectra of the decomposition products of PEG-plasticized PLA biocomposites.

temperatures (Figures 9(a) and 9(b) are almost similar, probably because of the resulting many products that have similar structures and they have overlapped bands which make the interpretation of the spectra difficult. The differences between systems of different compositions are found in 2100-3200 cm^{-1} and 1300–1700 cm^{-1} wavenumber regions. At an average maximum gas evolution temperature of 330-340°C, the following differences are observed (Figure 9(a)): 3253 cm^{-1} (O-H stretch, H-bonded) and 2820 cm^{-1} (C-H stretch) are absent in the spectra of PLA/PEG and PLA/-PEG/6CS/R, and the ratios of the intensity of the bands 2360, 2321, and 2362 cm^{-1} (C=O, C-N, and COO- stretching) are different being clearly spited only in PLA/PEG spectrum. 1681 (carbonyl C=O stretch), 1641 (C=C stretch), 1606, 1550, and 1489 cm^{-1} (aromatic domain and N-H bending, C-O stretching vibration (amide) and C-C stretching from phenyl groups, COO- stretching, and CH$_2$ bending) are present only in the PLA/PEG/R spectrum [76]. These bands probably correspond to the fragments that resulted from α-pinene and 1,8-cineole products which may evolve from rosemary ethanolic extract. At an average maximum GS of 400-415°C (Figure 9(b)) besides the abovementioned differences in the spectra corresponding to 330-340°C decomposition temperature, the bands in the 2990-2819 cm^{-1} (C-H stretch and =C-H stretch) region are found with different intensity ratios and differences in the 650-930 cm^{-1} region (=C-H bending, aromatic sp^2 C-H, and alkene sp^2 C-H bending) again much evident in the PLA/PEG/R spectrum [77]. Much information about the decomposition products are obtained from the MS spectra (Figures 10(a) and 10(b)).

Comparing FTIR spectrum results with those obtained from MS of Figure 10 indicates different products that resulted both at the two temperatures at which they are collected and also between different systems. The MS spectra of the decomposition products collected at high temperature show many fragments (Figure 10(b)) in comparison with those from lower decomposition temperature (Figure 10(a)) and also fragments with higher m/z. Comparing the MS spectra of PLA/PEG with those of PLA/PEG/6CS biocomposite, it is evident that the fragments with low m/z are fewer in the second spectra at both GS temperatures, because by PLA and chitosan, decomposition results larger fragments. The PLA/PEG/6CS/R biocomposite shows the much complex MS spectra. In all spectra, decomposition products can be identified that resulted from PLA as a large amount of cyclic oligomers through the random degradation process, acetal-

dehyde (m/z 15, 26, and 43), 2,3-pentadione, acrylic acid, lactide mesoform, or DL form [78, 79]. Common decomposition products were also H$_2$O, CO$_2$, and hydrocarbons (m/z of 18, 44, 12-17, etc., respectively) [80].

Thermal degradation of the chitosan is a complex reaction involving two or even three degradation stages. Hong et al. [81] studied the thermal degradation of chitosan in nitrogen, and they found that it depends on heating rate; the kinetic parameter constants of the thermal degradation vary with the degree of decomposition and increase with the reaction temperature. The degradation process of CS usually begins with random splitting of β-1,4-glycosidic bonds (depolymerization) followed by N-acetyl linkage (deacetylation). Simultaneously with chitosan chain scission, cleavage and/or destruction of its functional groups (amino, carbonyl, amide, and hydroxyl) occur. In addition, chitosan depolymerization may lead to formation of free radicals which induce oxidation processes. The degradation products identified by GC-MS and that could arise from CS were 5-hydroxy-1,3-pentadiene, cyclohex-1-en-6-ol, 4,5-dihydroxy-pent-1-ene, 1-ethylbenzene, 6-hydroxy-2, 4-hexadinol, and 3,5,6-trihydroxyhexanol [82–84]. The 80 and 67 fragments originate from the d-glucosamine moiety of the polymer and the 60 and 42 fragments from the N-ethyl-d-glucosamine moiety [85].

Several phenolic and terpenic compounds in *Rosmarinus officinalis L.* were identified by GC-MS as simple phenolics, phenolic acids (caffeic and rosmarinic acid), phenolic diterpenes (carnosic acid), and pentacyclic triterpenes (ursolic, oleanolic, and betulinic acid and betulin) and flavonoids [26, 86, 87]. These compounds are different from those arising from the other two components of the studied systems explaining the differences between FTIR and MS spectra recorded for decomposition products at various temperatures and different compositions.

An efficient heating method is necessary to get maximum benefits of antioxidant compounds. Degradation of carnosic acid, carnosol, rosmarinic acid, and a mixture of three was studied by Zhang and others [88] by using HPLC. Several degradation products also formed by exposure to light. Ethanolic standards for rosemary extract were tested in various conditions, for example, carnosic acid, carnosol, rosmarinic acid, and a mixture of three exposed to six different conditions such as -10°C, 4°C in the dark, room temperature with light exposure, room temperature in the dark, 40°C with light exposure, and 40°C in the dark. The effect of temperature and
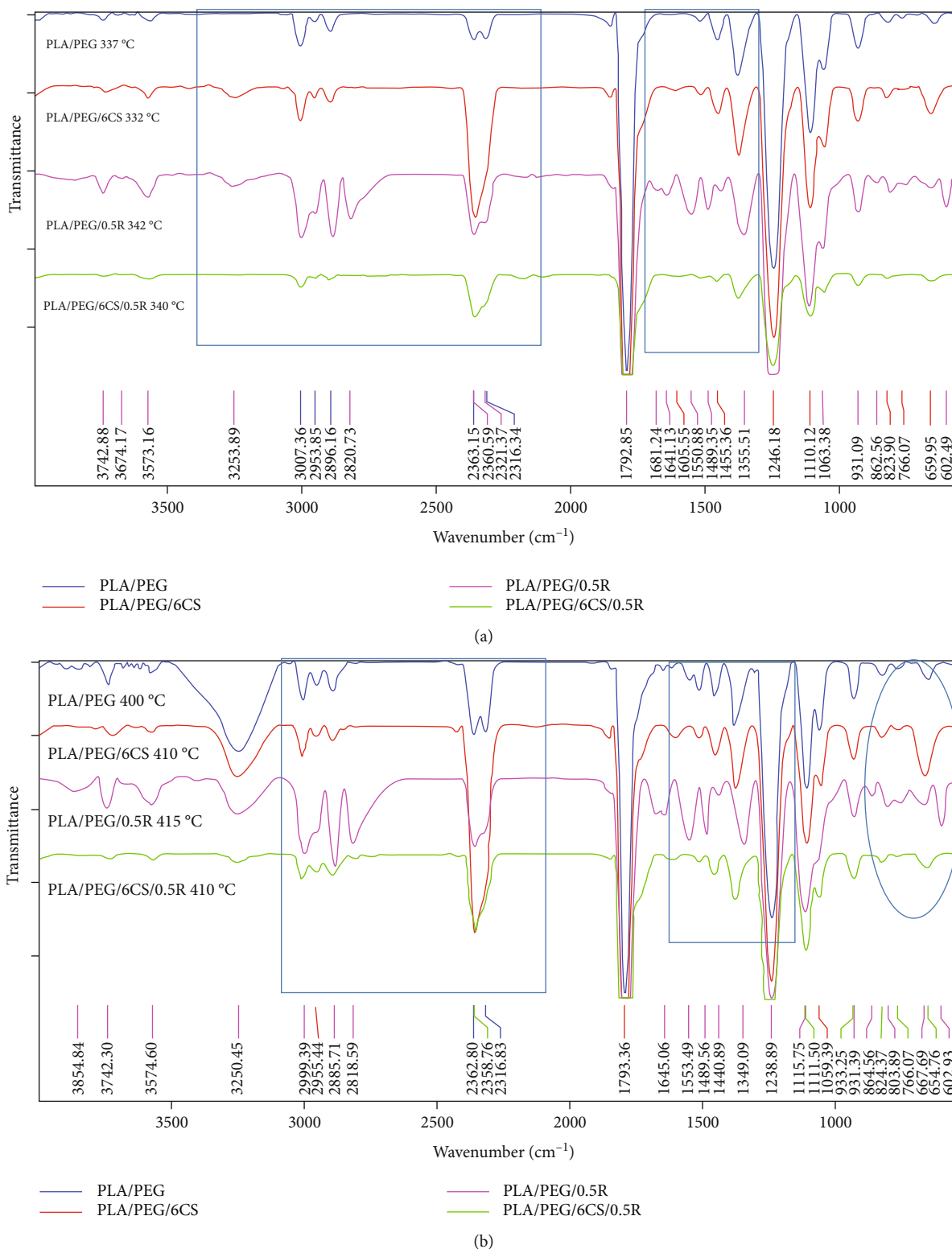
Figure 9: 2D FTIR spectra of the volatile decomposition products of PEG-plasticized PLA biocomposites at two GS temperatures of their evolution of ~330-340°C (a) and 410°C (b).

light was observed for 13 days. Rosmarinic acid did not degrade either by itself or in the mixture, whereas carnosic acid was fairly stable than carnosol degradation. Carnosic acid by itself and in the mixture was quite stable. Rosmanol,

epirosmanol, and epirosmanol ethyl ether major degradation products were also observed in HPLC chromatograms of carnosol and effect of temperature was also noticed during the formation of these degradation products. Rosmanol was

FIGURE 10: MS spectra corresponding to a maximum decomposition rate temperature of two steps in DTG curves: ~330-340°C (a) and 400-415°C (b).

present in the highest amount when stored at -10°C. Rosmadial and 11-ethoxy-rosmanol semiquinone also appeared as degradation products in carnosol HPLC chromatograms.

No toxicity or allergic responses were found for most of identified degradation products [89].

4. Conclusion

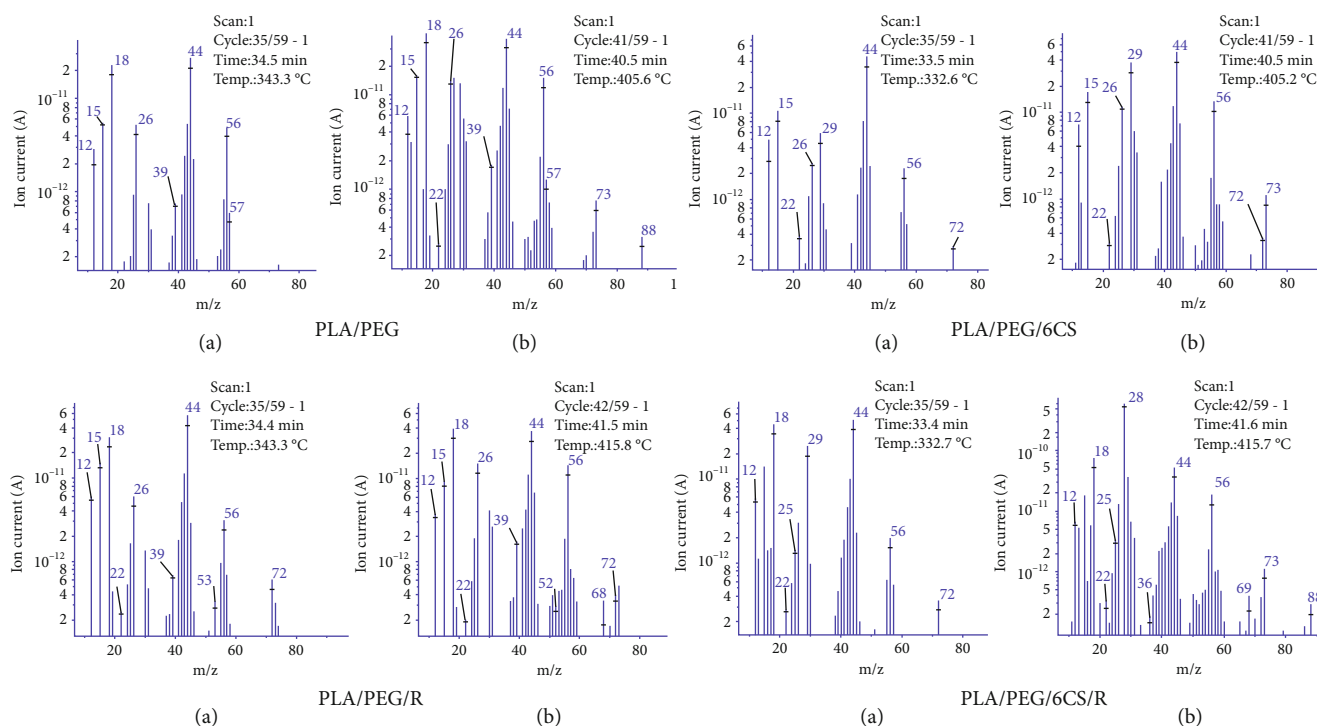Thermal behavior of some multifunctional environmentally friendly materials exhibiting antimicrobial/antioxidant activities and biocompatibility, based on PEG-plasticized PLA/CS and rosemary extract (R), has been investigated. Differential scanning calorimetry, combined with other complex investigations such as chemiluminescence and coupled thermogravimetry/Fourier-transform infrared spectroscopy/mass spectroscopy methods, was applied both to test the thermal behavior and to establish the composition–property relationship for the developed biocomposites. It has been established that the addition of CS shifted the T_g to slightly higher values while the cold crystallization temperature of PLA-based biocomposites to lower temperatures showing that the CS can promote the crystallization of PLA. This is also proved by the increase of the crystallization degree of the biocomposites in respect with that of plasticized PLA. Melting temperature is not changed while melting heat takes higher values for biocomposites in respect with PLA/PEG blend. It has been evidenced by a chemiluminescence study that the rosemary ethanolic extract is a good stabilizer for thermoxidative degradation of PLA. The highest onset (T_{onset}), maximum (T_{max}), and, respectively, GS temperature and decomposition temperatures corresponding to 10% (T_{10}) and 20% (T_{20}) mass loss are found for

the PLA/PEG/6CS and PLA/PEG/CS/R biocomposites. The same biocomposites also show the highest values for apparent activation energy of decomposition. Therefore, the plasticized PLA/CS/R materials show good thermal properties and most of thermal degradation products are nontoxic being recommended as suitable for both medical and food packaging applications.

Data Availability

The data used to support the findings of this study are available from the corresponding author upon request.

Additional Points

Highlights. New plasticized PLA-based materials have been obtained by melt blending with chitosan and powdered rosemary ethanolic extract. The effect of natural additives on the thermal behavior of PEG-plasticized PLA was assessed. The thermal characteristics confirmed the good thermal performance of these biocomposites for application in biomedicine or food packaging field.

Conflicts of Interest

The authors declare that there is no conflict of interest regarding the publication of this paper.

Acknowledgments

References

[1] L. Chen, X. Qiu, Z. Xie et al., "Poly(L-lactide)/starch blends compatibilized with poly(L-lactide)-g-starch copolymer," *Carbohydrate Polymers*, vol. 65, no. 1, pp. 75–80, 2006.

[2] M. A. Elsawy, K. H. Kim, J. W. Park, and A. Deep, "Hydrolytic degradation of polylactic acid (PLA) and its composites," *November Renewable and Sustainable Energy Reviews*, vol. 79, pp. 1346–1352, 2017.

[3] V. Taubner and R. Shishoo, "Influence of processing parameters on the degradation of poly(L-lactide) during extrusion," *Journal of Applied Polymer Science*, vol. 79, no. 12, pp. 2128–2135, 2001.

[4] M. C. Gupta and V. G. Deshmukh, "Thermal oxidative degradation of poly-lactic acid," *Colloid & Polymer Science*, vol. 260, no. 3, pp. 308–311, 1982.

[5] S. H. Hyon, K. Jamshidi, and Y. Ikada, "Effects of residual monomer on the degradation of DL-lactide polymer," *Polymer International*, vol. 46, no. 3, pp. 196–202, 1998.

[6] H. Yu, N. Huang, C. Wang, and Z. Tang, "Modeling of poly(L-lactide) thermal degradation: theoretical prediction of molecular weight and polydispersity index," *Journal of Applied Polymer Science*, vol. 88, no. 11, pp. 2557–2562, 2003.

[7] M. R. Mitchell, R. E. Link, M.-H. Yang, and Y.-H. Lin, "Measurement and Simulation of Thermal Stability of poly(lactic acid) by thermogravimetric analysis," *Journal of Testing and Evaluation*, vol. 37, no. 4, p. 102271, 2009.

[8] S. Gogolewski, M. Jovanovic, S. M. Perren, J. G. Dillon, and M. K. Hughes, "The effect of melt-processing on the degradation of selected polyhydroxyacids: polylactides, polyhydroxybutyrate, and polyhydroxybutyrate-co-valerates," *Polymer Degradation and Stability*, vol. 40, no. 3, pp. 313–322, 1993.

[9] S. Saeidlou, M. A. Huneault, H. Li, and C. B. Park, "Poly(lactic acid) crystallization," *Progress in Polymer Science*, vol. 37, no. 12, pp. 1657–1677, 2012.

[10] M. Savaris, V. D. Santos, and R. N. Brandalise, "Influence of different sterilization processes on the properties of commercial poly(lactic acid)," *Materials Science and Engineering: C*, vol. 69, pp. 661–667, 2016.

[11] H. Tsuji and I. Fukui, "Enhanced thermal stability of poly(lactide)s in the melt by enantiomeric polymer blending," *Polymer*, vol. 44, no. 10, pp. 2891–2896, 2003.

[12] Z. Jing, X. Shi, and G. Zhang, "Competitive stereocomplexation and homocrystallization behaviors in the poly(lactide) blends of PLLA and PDLA-PEG-PDLA with controlled block length," *Polymers*, vol. 9, no. 12, p. 107, 2017.

[13] F.-L. Jin, R.-R. Hu, and S.-J. Park, "Improvement of thermal behaviors of biodegradable poly(lactic acid) polymer: a review," *Composites Part B: Engineering*, vol. 164, pp. 287–296, 2019.

[14] R. M. Rasal, A. V. Janorkar, and D. E. Hirt, "Poly(lactic acid) modifications," *Progress in Polymer Science*, vol. 35, no. 3, pp. 338–356, 2010.

[15] A. Ruellan, V. Ducruet, and S. Domenek, "Plasticization of poly(lactide)," in *Poly(lactic acid) Science and Technology: Processing, Properties, Additives and Applications*, Polymer Chemistry Series No. 12, pp. 124–170, The Royal Society of Chemistry, 2015.

[16] M. Rapa, R. N. Darie-Niță, A. Irimia et al., "Comparative analysis of two bioplasticizers used to modulate the properties of PLA biocomposites," *Materiale Plastice*, vol. 54, no. 4, pp. 610–615, 2017.

[17] M. Râpă, R. N. Darie-Niță, E. Grosu et al., "Effect of plasticizers on melt processability and properties of PHB," *Journal of Optoelectronics and Advanced Materials*, vol. 17, no. 11-12, pp. 1778–1784, 2015.

[18] M. Rapa, R. N. Darie-Niță, and C. Vasile, "Influence of plasticizers over some physico-chemical properties of PLA," *Materiale Plastice*, vol. 54, no. 1, pp. 73–78, 2017.

[19] M. Râpă, C. Vasile, E. Grosu et al., *PCT/RO2016 /000028/27.12.2016. PLA -based active and degradable biocomposites for food packaging, publication WO/2018/117885/ 28.06*, International Application No.:PCT/RO2016/000028, 2018.

[20] M. Râpă, A. C. Mitelut, E. E. Tanase et al., "Influence of chitosan on mechanical, thermal, barrier and antimicrobial properties of PLA-biocomposites for food packaging," *Composites Part B: Engineering*, vol. 102, pp. 112–121, 2016.

[21] R. N. Darie-Niță, C. Vasile, A. Irimia, R. Lipșa, and M. Râpă, "Evaluation of some eco-friendly plasticizers for PLA films processing," *Journal of Applied Polymer Science*, vol. 133, no. 13, 2016.

[22] O. Martin and L. Avérous, "Poly(lactic acid): plasticization and properties of biodegradable multiphase systems," *Polymer*, vol. 42, no. 14, pp. 6209–6219, 2001.

[23] F. Croisier and C. Jérôme, "Chitosan-based biomaterials for tissue engineering," *European Polymer Journal*, vol. 49, no. 4, pp. 780–792, 2013.

[24] I. Wedmore, J. G. McManus, A. E. Pusateri, and J. B. Holcomb, "A special report on the chitosan-based hemostatic dressing: experience in current combat operations," *The Journal of Trauma*, vol. 60, no. 3, pp. 655–658, 2006.

[25] R. Darie-Niță, C. Vasile, E. Stoleru et al., "Evaluation of the rosemary extract effect on the properties of polylactic acid-based materials," *Materials*, vol. 11, no. 10, p. 1825, 2018.

[26] N. T. Maheshwari, Kansas State University, Manhattan Kansas, 2016, 1994, http://krex.k-state.edu/dspace/handle/ 2097/20596.

[27] A. Tomaino, F. Cimino, V. Zimbalatti et al., "Influence of heating on antioxidant activity and the chemical composition of some spice essential oils," *Food Chemistry*, vol. 89, no. 4, pp. 549–554, 2005.

[28] M. Khatun, S. Eguchi, T. Yamaguchi, H. Takamura, and T. Matoba, "Effect of thermal treatment on radical-scavenging activity of some spices," *Food Science and Technology Research*, vol. 12, no. 3, pp. 178–185, 2006.

[29] C. Vasile, E. Stoleru, R. N. Darie-Nița, R. P. Dumitriu, D. Pamfil, and L. Tarțau, "biocompatible materials based on plasticized Poly(lactic acid), chitosan and rosemary ethanolic Extract I. Effect of chitosan on the properties of plasticized Poly(lactic acid) materials," *Polymers*, vol. 11, no. 6, p. 941, 2019.

[30] T. Zaharescu, S. Jipa, W. Kappel, D. Artenie-Mariș, M. Mariș, and A. Mantsch, *E-Polymers*, vol. 1, p. 149, 2009, http://www .e-polymers.org.

[31] N. Troncoso, H. Sierra, L. Carvajal, P. Delpiano, and G. Gunther, "Fast high performance liquid chromatography and ultraviolet-visible quantification of principal phenolic antioxidants in fresh rosemary," *Journal of Chromatography A*, vol. 1100, no. 1, pp. 20–25, 2005.

[32] H.-J. Liu, C.-T. Hsieh, and D. S.-G. Hu, "Solute diffusion through degradable semicrystalline polyethylene glycol/poly(L-lactide) copolymers," *Polymer Bulletin*, vol. 32, no. 4, pp. 463–470, 1994.

[33] X. Liu, M. Dever, N. Fair, and R. S. Benson, "Thermal and mechanical properties of poly(lactic acid) and poly(ethylene/butylene succinate) blends," *Journal of environmental polymer degradation*, vol. 5, no. 4, pp. 225–235, 1997.

[34] H. E. Kissinger, "Reaction kinetics in differential thermal analysis," *Analytical Chemistry*, vol. 29, no. 11, pp. 1702–1706, 1957.

[35] P. Budrugeac and E. Segal, "Applicability of the Kissinger equation in thermal analysis," *Journal of Thermal Analysis and Calorimetry*, vol. 88, no. 3, pp. 703–707, 2007.

[36] J. P. Elder, "The general applicability of the Kissinger equation in thermal analysis," *Journal of Thermal Analysis*, vol. 30, no. 3, pp. 657–669, 1985.

[37] R. M. R. Wellen and E. L. Canedo, "On the Kissinger equation and the estimate of activation energies for non- isothermal cold crystallization of PET," *Polymer Testing*, vol. 40, pp. 33–38, 2014.

[38] https://www.perkinelmer.com/lab-solutions/resources/docs/APP_TgandMeltofPolyethylene.pdf.

[39] S. Jia, D. Yu, Y. Zhu, Z. Wang, L. Chen, and L. Fu, "Morphology, Crystallization and thermal behaviors of PLA-based composites: wonderful effects of hybrid GO/PEG via dynamic impregnating," *Polymers*, vol. 9, no. 12, pp. 528–535, 2017, https://www.mdpi.com/journal/polymers.

[40] N. T. T. Trang, N. T. Chinh, N. V. Giang et al., "Hydrolysis of green nanocomposites of poly(lactic acid) (PLA), chitosan (CS) and polyethylene glycol (PEG) in acid solution," *Green Processing and Synthesis*, vol. 5, no. 5, pp. 443–449, 2016.

[41] S. Kamthai and R. Magaraphan, "Thermal and mechanical properties of polylactic acid (PLA) and (CMCB) composite by adding isosorbide diesters," *AIP Conference Proceedings*, vol. 1664, article 060006, 2015.

[42] M. Bijarimi, S. Ahmad, R. Rasid, M. A. Khushairi, and M. Zakir, "Poly(lactic acid) / poly(ethylene glycol) blends: mechanical, thermal and morphological properties," *AIP Conference Proceedings*, vol. 1727, article 020002, 2016.

[43] J. Ahmed, N. Hiremath, and H. Jacob, "Antimicrobial, rheological, and thermal properties of plasticized polylactide films incorporated with essential oils to InhibitStaphylococcus aureusandCampylobacter jejuni," *Journal of Food Science*, vol. 81, no. 2, pp. E419–E429, 2016.

[44] M. Ramos, A. Jimenez, M. Peltzer, and M. C. Garrigos, "Development of novel nano-biocomposite antioxidant films based on poly (lactic acid) and thymol for active packaging," *Food Chemistry*, vol. 162, pp. 149–155, 2014.

[45] Y. Qin, J. Yang, and J. Xue, "Characterization of antimicrobial poly(lactic acid)/poly(trimethylene carbonate) films with cinnamaldehyde," *Journal of Materials Science*, vol. 50, no. 3, pp. 1150–1158, 2015.

[46] A. A. J. Kumar and V. Srinivasan, "Mechanical and thermal properties of chitosan filled poly lactic acid/basalt fiber hybrid composites," *Journal of Advanced Microscopy Research*, vol. 11, no. 1, pp. 23–30, 2016.

[47] J. Z. Xu, Z. J. Zhang, H. Xu, J. B. Chen, R. Ran, and Z. M. Li, "Highly enhanced crystallization kinetics of poly(l-lactic acid) by poly(ethylene glycol) grafted graphene oxide simultaneously as heterogeneous nucleation agent and chain mobility promoter," *Macromolecules*, vol. 48, no. 14, pp. 4891–4900, 2015.

[48] W. C. Lai, W. B. Liau, and T. T. Lin, "The effect of end groups of PEG on the crystallization behaviors of binary crystalline polymer blends PEG/PLLA," *Polymer*, vol. 45, no. 9, pp. 3073–3080, 2004.

[49] N. Kameno, S. Yamada, T. Amimoto, K. Amimoto, H. Ikeda, and N. Koga, "Thermal degradation of poly(lactic acid) oligomer: reaction mechanism and multistep kinetic behavior," *Polymer Degradation and Stability*, vol. 134, pp. 284–295, 2016.

[50] J. Glastrup, "Degradation of polyethylene glycol. A study of the reaction mechanism in a model molecule: tetraethylene glycol," *Polymer Degradation and Stability*, vol. 52, no. 3, pp. 217–222, 1996.

[51] T. Zaharescu, M. Râpă, and V. Marinescu, "Chemiluminescence kinetic analysis on the oxidative degradation of poly(lactic acid)," *Journal of Thermal Analysis and Calorimetry*, vol. 128, no. 1, pp. 185–191, 2017.

[52] R. Al-Itry, K. Lamnawar, and A. Maazouz, "Improvement of thermal stability, rheological and mechanical properties of PLA, PBAT and their blends by reactive extrusion with functionalized epoxy," *Polymer Degradation and Stability*, vol. 97, no. 10, pp. 1898–1914, 2012.

[53] Y. Fan, H. Nishida, Y. Shirai, Y. Tokiwa, and T. Endo, "Thermal degradation behaviour of poly(lactic acid) stereocomplex," *Polymer Degradation and Stability*, vol. 86, no. 2, pp. 197–208, 2004.

[54] D. J. Carlsson, C. J. B. Dobbin, and D. M. Wiles, "Direct observations of macroperoxyl radical propagation and termination by electron spin resonance and infrared spectroscopies," *Macromolecules*, vol. 18, no. 10, pp. 2092–2094, 1985.

[55] T. Zaharescu, M. Râpă, E.-M. Lungulescu, and N. Butoi, "Filler effect on the degradation of γ-processed PLA/vinyl POSS hybrid," *Physical Chemistry*, vol. 153, pp. 188–197, 2018.

[56] R. Dorati, I. Genta, L. Montanari et al., "The effect of γ-irradiation on PLGA/PEG microspheres containing ovalbumin," *Journal of Controlled Release*, vol. 107, no. 1, pp. 78–90, 2005.

[57] Q. Breche, G. Chagnon, G. Machado et al., "Mechanical behaviour's evolution of a PLA- b -PEG-b-PLA triblock copolymer during hydrolytic degradation," *Journal of The Mechanical Behavior of Biomedical Materials*, vol. 60, pp. 288–300, 2016.

[58] R. Scaffaro, A. Maio, F. Lopresti et al., "Synthesis and self-assembly of a PEGylated-graphene aerogel," *Composites Science and Technology*, vol. 128, pp. 193–200, 2016.

[59] M. Oliveira, E. Santos, A. Araújo, G. J. M. Fechine, A. V. Machado, and G. Botelho, "The role of shear and stabilizer on PLA degradation," *Polymer Testing*, vol. 51, pp. 109–116, 2016.

[60] D. Cam and M. Marucci, "Influence of residual monomers and metals on poly (L-lactide) thermal stability," *Polymer*, vol. 38, no. 8, pp. 1879–1884, 1997.

[61] F. D. Kopinke and K. Mackenzie, "Mechanistic aspects of the thermal degradation of poly(lactic acid) and poly(β-hydroxybutyric acid)," *Journal of Analytical and Applied Pyrolysis*, vol. 40-41, no. 40/41, pp. 43–53, 1997.

[62] P. Nugroho, H. Mitomo, F. Yoshii, and T. Kume, "Degradation of poly(L-lactic acid)by γ-irradiation," *Polymer Degradation and Stability*, vol. 72, no. 2, pp. 337–343, 2001.

[63] G. Reich, "Ultrasound-induced degradation of PLA and PLGA during microsphere processing: influence of formulation variables," *European Journal of Pharmaceutics and Biopharmaceutics*, vol. 45, no. 2, pp. 165–171, 1998.

[64] G. Y. Lee, *Thermal degradation of poly(lactic acid)*, Graduate Institute of Environmentally Polymeric Materials of KaoYuan University, Taiwan, ROC, 2006.

[65] F. D. Kopinke, M. Remmler, K. Mackenzie, M. Möder, and O. Wachsen, "Thermal decomposition of biodegradable polyesters–II. Poly(lactic acid)," *Polymer Degradation and Stability*, vol. 53, no. 3, pp. 329–342, 1996.

[66] B. Chieng, N. Ibrahim, Y. Then, and Y. Loo, "Epoxidized vegetable oils plasticized poly(lactic acid) biocomposites: mechanical, thermal and morphology properties," *Molecules*, vol. 19, no. 10, pp. 16024–16038, 2014, https://www.mdpi.com/journal/molecules.

[67] C. P. Chang, I.-C. Wang, and Y.-S. Perng, "Enhanced thermal behavior, mechanical properties and UV shielding of polylactic acid (PLA) composites reinforced with nanocrystalline cellulose and filled with nanosericite," *Cellulose Chemistry and Technology*, vol. 47, no. 1-2, pp. 111–123, 2013.

[68] E. Fortunati, I. Armentano, A. Iannoni, and J. M. Kenny, "Development and thermal behaviour of ternary PLA matrix composites," *Polymer Degradation and Stability*, vol. 95, no. 11, pp. 2200–2206, 2010.

[69] A. Y. Snegirev, V. A. Talalov, V. V. Stepanov, O. P. Korobeinichev, I. E. Gerasimov, and A. G. Shmakov, "Autocatalysis in thermal decomposition of polymers," *Polymer Degradation and Stability*, vol. 137, pp. 151–161, 2017.

[70] A. N. Ford Versypt, D. W. Pack, and R. D. Braatz, "Mathematical modeling of drug delivery from autocatalytically degradable PLGA microspheres—a review," *Journal of Controlled Release*, vol. 165, no. 1, pp. 29–37, 2013.

[71] I. C. McNeill and H. A. Leiper, "Degradation studies of some polyesters and polycarbonates–1\. Polylactide: General features of the degradation under programmed heating conditions," *Polymer Degradation and Stability*, vol. 11, no. 3, pp. 267–285, 1985.

[72] I. C. McNeill and H. A. Leiper, "Degradation studies of some polyesters and polycarbonates–2\. Polylactide: Degradation under isothermal conditions, thermal degradation mechanism and photolysis of the polymer," *Polymer Degradation and Stability*, vol. 11, no. 4, pp. 309–326, 1985.

[73] Y. Aoyagi, K. Yamashita, and Y. Doi, "Thermal degradation of poly[(R)-3–hydroxybutyrate], poly[ε-caprolactone], and poly[(S)-lactide]," *Polymer Degradation and Stability*, vol. 76, no. 1, pp. 53–59, 2002.

[74] G. Sivalingam and G. Madras, "Thermal degradation of binary physical mixtures and copolymers of poly(ε-caprolactone), poly(D, L-lactide), poly(glycolide)," *Polymer Degradation and Stability*, vol. 84, no. 3, pp. 393–398, 2004.

[75] A. K. Pal and V. Katiyar, "Thermal degradation behaviour of nanoamphiphilic chitosan dispersed poly (lactic acid) bionanocomposite films," *International Journal of Biological Macromolecules*, vol. 95, pp. 1267–1279, 2017.

[76] C. M. Topala and L. D. Tataru, "ATR-FTIR study of thyme and rosemary oils extracted by supercritical carbon dioxide," *Revista de Chimie*, vol. 67, no. 5, pp. 842–846, 2016.

[77] https://www.cpp.edu/~psbeauchamp/pdf/spec_ir_nmr_spectra_tables.pdf.

[78] H. Nishida, T. Mori, S. Hoshihara, Y. Fan, Y. Shirai, and T. Endo, "Effect of tin on poly(l-lactic acid) pyrolysis," *Polymer Degradation and Stability*, vol. 81, no. 3, pp. 515–523, 2003.

[79] S. Tsuge, H. Ohtani, and C. Watanabe, *Pyrolysis-GC/MS Data Book of Synthetic Polymers: Pyrograms, Thermograms and MS of Pyrolyzates*, vol. 420, Elsevier, 2011, https://books.google.ro/books?id=mbtybfqbEs8C&printsec=frontcover&hl=ro&source=gbs_ge_summary_r&cad=0#v=onepage&q&f=false.

[80] H. Lin, L. Han, and L. Dong, "Thermal degradation behavior and gas phase flame-retardant mechanism of polylactide/PCPP blends," *Journal of Applied Polymer Science*, vol. 131, no. 13, p. 40480, 2014.

[81] P.-Z. Hong, S.-D. Li, C.-Y. Ou, C.-P. Li, L. Yang, and C.-H. Zhang, "Thermogravimetric analysis of chitosan," *Journal of Applied Polymer Science*, vol. 105, no. 2, pp. 547–551, 2007.

[82] I. Corazzari, R. Nistico, F. Turci et al., "Advanced physico-chemical characterization of chitosan by means of TGA coupled on-line with FTIR and GCMS: thermal degradation and water adsorption capacity," *Polymer Degradation and Stability*, vol. 112, pp. 1–9, 2015.

[83] M. A. Diab, A. Z. El-Sonbati, M. M. Al-Halawany, and D. M. D. Bader, "Thermal stability and degradation of chitosan modified by cinnamic acid," *Open Journal of Polymer Chemistry*, vol. 2, no. 1, pp. 14–20, 2012.

[84] M. A. Diab, A. Z. El-Sonbati, and D. M. D. Bader, "Thermal stability and degradation of chitosan modified by benzophenone," *Spectrochimica Acta. Part A, Molecular and Biomolecular Spectroscopy*, vol. 79, no. 5, pp. 1057–1062, 2011.

[85] J. Mattai and E. R. Hayes, "Characterization of chitosan by pyrolysis–mass spectrometry," *Journal of Analytical and Applied Pyrolysis*, vol. 3, no. 4, pp. 327–334, 1982.

[86] M. Islamcevic-Razborsek, D. Brodnjak Voncina, V. Dolecek, and E. Voncina, "Determination of major phenolic acids, phenolic diterpenes and triterpenes in rosemary (Rosmarinus officinalis L.) by gas chromatography and mass spectrometry," *Acta Chimica Slovenica*, vol. 54, pp. 60–67, 2007.

[87] J. Damasius, P. R. Venskutonis, V. Kaskoniene, and A. Maruska, "Fast screening of the main phenolic acids with antioxidant properties in common spices using on-line HPLC/UV/DPPH radical scavenging assay," *Analytical Methods*, vol. 6, no. 8, p. 2774, 2014.

[88] Y. Zhang, J. P. Smuts, E. Dodbiba, R. Rangarajan, J. C. Lang, and D. W. Armstrong, "Degradation study of carnosic acid, carnosol, rosmarinic acid, and rosemary extract (Rosmarinus officinalisL.) assessed using HPLC," *Journal of Agricultural and Food Chemistry*, vol. 60, no. 36, pp. 9305–9314, 2012.

[89] M. T. Cronin, J. Madden, D. Roberts, and S. Enoch, *Chemical toxicity prediction: category formation and read-across*, Royal Society of Chemistry, 2013.

Research Article

Effectual Anticancer Potentiality of Loaded Bee Venom onto Fungal Chitosan Nanoparticles

Adel I. Alalawy [1], **Haddad A. El Rabey** [1,2] **Fahad M. Almutairi** [1], **Ahmed A. Tayel** [3] **Mohammed A. Al-Duais** [1,4] **Nahla S. Zidan** [5,6] **and Mohamed I. Sakran** [1,7]

[1]*Biochemistry Department, Faculty of Science, University of Tabuk, Saudi Arabia*
[2]*Bioinformatics Department, Genetic Engineering and Biotechnology Research Institute, University of Sadat City, Sadat City, Egypt*
[3]*Faculty of Aquatic and Fisheries Sciences, Kafrelsheikh University, Egypt*
[4]*Chemistry Department, Faculty of Science, Ibb University, Yemen*
[5]*Department of Nutrition and Food Science, Faculty of Home Economics, University of Tabuk, Saudi Arabia*
[6]*Department of Home Economics, Faculty of Specific Education, Kafrelsheikh University, Egypt*
[7]*Biochemistry Section, Chemistry Department, Faculty of Science, Tanta University, Egypt*

Correspondence should be addressed to Haddad A. El Rabey; elrabey@hotmail.com
and Ahmed A. Tayel; tayel_ahmad@yahoo.com

Chitosan and its nanoparticles (NPs) could be extracted from numerous fungal species and used as effectual carriers for bioactive compounds. The fungal chitosan (FC) was innovatively acquired from *Fusarium oxysporum* grown mycelia, characterized and used for NP synthesis and loading with bee venom (BV). The nano-FC (NFC) had 192.4 nm mean NP diameter, 38.22% loading capacity, and 92.42% entrapment efficiency. BV release from NFC was pH and time dependent; burst BV release was detected at the first 6 h, followed by gradual releases up to 30 h. The *in vitro* anticancer potentiality valuation, of NFC, BV, and NFC/BV nanoconjugates against HeLa cervix carcinoma, revealed that they all had potent dose-dependent anticancer activity; BV/NFC nanoconjugates were the most effective with $IC_{50} = 200 \mu g/mL$. The fluorescent staining of treated HeLa cells with BV/NFC nanoconjugates, with DAPI and acridine orange/propidium iodide combination, indicated the appearance of early apoptosis, secondary apoptosis, and secondary necrosis markers and their increment with exposure prolongation. The production of NFC from *F. oxysporum* and their loading with BV are strongly counseled for production of potent natural antitumor agent with augmented activity against cervix carcinoma.

1. Introduction

Chitosan (Cts), the astounding amino polysaccharide derived from deacetylated chitin, has numerous practical advantages (e.g., its biodegradability, nontoxicity, biocompatibility, and effectual bioactivities) [1]. The Cts bioactivities encouraged its biomedical utilization in frequent applications (e.g., drug delivery, tissue engineering, anticancer treatment, antimicrobial formulations, and wound-healing dressing) [2]. The Cts charges and contents from amine groups are mostly the keys for its bioactive physiognomies (e.g., drug carrying, mucoadhesion, antimicrobial activity, drug release controlling, *in situ* gelation, and permeation enhancement) [3], which promoted its wide application as drug carrier and enhancer. Cts was promisingly extracted from the biomass of numerous fungal species [4–9]; the extracted fungal chitosan (FC) had comparable or superior bioactive attributes than accustomed commercial Cts.

Bee venom (BV) is the released defense weapon from honeybee (*Apis mellifera*) when their colony is attacked. BV

contains composited mixtures from bioactive peptides that could protect bees' colony against a broad diversity of predators and invaders. The contained bioactive components in BV include melittin (the major BV constituent), adolapin, apamin, degranulating peptide (for mast cell), enzymes (hyaluronidase and phospholipase A2), and some nonpeptide constituents (e.g., dopamine, histamine, and norepinephrine) [10, 11].

The BV or its constituents (e.g., melittin) were extensively investigated as potential treatment and inhibitors of tumor types; they exhibited multiple potential molecular anticancer mechanisms [11–13]. Numerous studies and reviews were documented to verify the anticancer capabilities of either BV or melittin toward various tumor types [14–18]; they concluded that BV with its components has auspicious anticancer and cytotoxic agents with broader spectrum toward multiple tumor cell types.

The nanotechnology involvement in most biomedical fields became much prevalent, including nanomaterial applications themselves as antimicrobial, anticancer, antiviral, and biocidal agents, or their loading with bioactive drugs/compounds to increase their solubility, stability, functionality, and delivery to the human body [19]. The nanopolymers, particularly nano-Cts and nano-FC (abbreviated thereafter as NFC), were from the most evaluated nanomaterials for their bioactivity and functionality as drug carriers, biopreservatives, and antimicrobial, anticancer, and gene delivery agents, individually or composited with other active compounds [3, 20–23].

The Cts nanoparticles were effactually used as carriers and enhancers of different animal venoms including snake, scorpion, and BV, for their evaluation as anticancer agents [24–28].

Accordingly, current study targeted the production of NFC, its loading with BV, and evaluation of their physiognomies and bioactivities to inhibit cervix adenocarcinoma (HeLa) cells and elucidate their potential action as anticancer agents.

2. Materials and Methods

2.1. Fungal Chitosan (FC) Extraction. Fungal culture, *Fusarium oxysporum* f. sp. *medicaginis*, ATCC® 52169™ (abbreviated thereafter as *Fom*), was used herein for FC production. Broth and agar media of potato dextrose (PDB and PDA, Difco Laboratories, Sparks, MD) were employed for *Fom* culture propagation and maintenance. Fungal incubation in PDB was prolonged for 7 days at 28°C under agitated aerobic conditions. The FC extraction was accomplished according to Tayel et al. [6]. Briefly, after cultivation, *Fom* mycelia were harvested via filtration, washed by deionized water (DW), and dried at 45°C in air oven. Dried *Fom* mycelia were deproteinized (using 1 M of NaOH), demineralized (using 1 M of acetic acid), and deacetylated (with 58% *w/v* NaOH solution at 110°C for 90 min); the filtration and extensive DW washing were repeated after each step. The FC deacetylation degree (DDA) was determined from its FTIR (Fourier-transform infrared spectroscopy) spectrum, using the Baxter et al.

formula [29]:

$$DDA\ (\%) = 100 - \left(\frac{A1655}{A3450} \times 115\right), \tag{1}$$

whereas the FC molecular weight (MW) was measured via chromatography (gel permeation attached to refractive index detector (Postnova, Eresing, Germany)).

2.2. Synthesis of Nanofungal Chitosan Loaded with Bee Venom. The synthesis of nanoparticles (NPs) from FC and their loading with BV depended on previous method modifications [20, 24], using the incorporation technique. Briefly, stock solutions were made from FC (2.0 mg/mL, in diluted acetic acid solution), TPP (sodium tripolyphosphate, 1.0 mg/mL of DW), and BV (1.0 mg/mL of DW). The TPP solution was minutely dropped (at a rate of 350 μL/min) into vigorously stirred FC solution, up to a final ratio of FC : TPP = 3 : 1 *w/w*. The stirring continued for 60 min after TPP dropping, and the resulted illuminated suspension containing nanofungal chitosan (NFC) was centrifuged at 28.000 × *g*, washed with DW, recentrifuged, and lyophilized. For the BV-loaded NFC, the BV was firstly added to the FC solution (to have a BV concentration of 500 μg/mL), stirred for 30 min, then the TPP solution and the rest of the aforementioned steps were applied.

2.3. Characterization of Synthesized NPs

2.3.1. FTIR Spectrophotometry. The FTIR (PerkinElmer™ FTIR V. 10.03.08, Germany) spectra of FC, NFC, BV, and BV/NFC nanocomposite were measured at wavenumbers of 450-4000 cm^{-1}. Powdered samples were merged with KBr (at 1% ratio, *w/w*), and their FTIR transmission spectra were plotted.

2.3.2. NP Physiognomic Analysis. The NP size range, mean, median, distribution (polydispersity index (PDI)), and charges (zeta potential) were measured for NFC and BV/NFC nanoconjugates, using Zetasizer (Malvern Instruments, UK), based on DLS (dynamic light scattering) technique. Additionally, the shape, distribution, and size of synthesized BV/NFC nanoconjugates were screened via electron microscopy (Transmission) imaging (TEM, Leica™ Leo0430, Cambridge Ltd, UK); the TEM carbon-coated grid was charged with NP solution and 1% uranyl acetate, air dried, and loaded into TEM for examination.

2.4. Evaluation of BV Encapsulation and Release

2.4.1. Protein Assay. Based on the "Bradford method," a standardized assay kit for protein (Pierce™ Coomassie, Thermo Scientific-Pierce, Rockford, IL) was operated for determining free BV concentration in the NP solution. The formed color from BV conjugation was spectrophotometrically measured at 595 nm absorption. BSA (bovine serum albumin) was utilized as the comparable standard protein.

2.4.2. Loading and Encapsulation Efficiency Measurement. Specified amounts (10 μg) from BV-loaded NFC were

dissolved in DW in centrifugal tubes by vigorous vortexing, and then, the solution was centrifuged at $28.000 \times g$ for 35 min at 10°C. The BV loading capacity (LC) and encapsulation efficiency (EE) were calculated as follows [20]:

$$\text{LC (\%)} = \left(\frac{\text{Total BV amount} - \text{Free BV in supernatant}}{\text{NP weight}} \right) \times 100,$$

$$\text{EE (\%)} = \left(\frac{\text{Total BV amount} - \text{Free BV in supernatant}}{\text{Total BV amount}} \right) \times 100.$$

$$(2)$$

2.4.3. In Vitro BV Release.

For BV release examination, the BV/NFC-NPs were transferred after centrifugation to clean centrifugal tubes with 3 mL of acetate buffer (pH 5.2) or phosphate buffer (PBS, pH 7.1). The tubes were maintained at 37 ± 1°C, and 100 μL samples were collected at time intervals of 2 h for 30 h; then, the protein contents were measured spectrophotometrically for each sample.

The released BV protein mass (M_i) at specific time (i) was calculated as follows [20]:

$$M_i = C_i V + \sum C_i - {}_1 V_s, \tag{3}$$

where C_i is the BV concentration in release solution at time i, V is the total release solution volume, and V_s is the sample volume.

2.5. NP Anticancer Activity

2.5.1. Cell Line Culture.

Human cell lines of cervix carcinoma (HeLa) obtained from EGY-NCI (National Cancer Institute, Cairo, Egypt) were used. Culturing of HeLa cells in EMEM medium (supplemented with 10% (v/v) fetal calf serum, 2.0 mM L-glutamine, 0.1 mM nonessential amino acids, 1.5 g/L NaHCO$_3$, and 1.0 mM sodium pyruvate) was performed in humidified air with 5% CO$_2$ at 37°C.

2.5.2. Evaluation of NP Antiproliferative Activity.

The BV/NFC-NPs antiproliferative activity was assessed using MTT (3-(4,5-dimethylthiazole-2-yl)-2,5-diphenyltetrazolium bromide) reduction assay [30]. In a 96-well polystyrene plate, each well contained 100 μL from complete medium, tumor cells ($\sim 1 \times 10^4$) were inoculated and incubated for 24 h in humidified air with 5% CO$_2$ at 37°C. After cell adherence, wells received gradual amounts of NFC, BV, and BV/NFC-NPs, after dissolving in DW, to have a concentration range of 0-500 μg/mL from each agent. After another 24 h of incubation, fresh media were added to replace the treatment solution and 10 μL of MTT solution (5 mg/mL of media without phenol red and serum) and plates were additionally incubated for further 3 h until purple formazan color appeared. After supernatant discarding, formazan crystals were dissolved with 100 μL of DMSO and the color was appraised at 540 nm absorbance within 1 h. Plain DMSO served as control.

The cell viability (%) was calculated as [(Absorbance of treated)/(Absorbance of control)] $\times$ 100.

2.5.3. Valuation of HeLa Cell Apoptosis Using Acridine Orange/Propidium Iodide Combined Staining.

The HeLa cell potential apoptosis, after treatment with BV/NFC nanoconjugate, was valuated via combined staining with acridine orange (AO) and propidium iodide (PI) [31]. HeLa cell suspension ($\sim 2 \times 10^5$ cells/mL) was treated with BV/NFC-NPs at 500 μg/mL concentration and incubated for 24 and 48 h in humidified air with 5% CO$_2$ at 37°C. Treated and control cells were rinsed using PBS, then double stained for 15 min with AO (10 mg/mL) and PI (4 mg/mL) in the dark. Images were captured (using fluorescence microscope Olympus BX51, Tokyo, Japan) based on the appearance of apoptosis indicators, i.e., the green-, orange-, and red-stained cells/organelles, within 25 min after staining.

2.5.4. Appraisal of Cell Apoptosis via DAPI Staining.

The BV/NFC-NPs-induced apoptosis was further analyzed using nuclear dye DAPI (4′,6-diamidino-2-phenylindole) fluorescent staining to detect nucleic DNA fragmentation and condensation in treated cells [32]. The treated HeLa cells were handled as mentioned in Section 2.5.3; then, after PBS washing, they were fixed with paraformaldehyde (4%) for 12 min and permeabilized with buffer (containing 0.5% Triton X-100 and 3% paraformaldehyde), then 50 μL of DAPI (with 1 μg/mL concentration) was added and kept for 60 min. The fluorescent micrographs were captured to demonstrate the liberated and condensed nuclei fragments stained by DAPI fluorescent dye.

3. Results

The FC extraction and production, from *Fom* grown mycelia, were gainfully achieved in this work; the FC productivity was 2.41 g/L of fermentation medium. The produced FC had a molecular weight of 51.6 kDa and DDA of 88.4%.

The process effectiveness of ionic gelation to transform FC into NFC and loading it with BV was assessed using FTIR to reveal their biochemical bonding and interactions.

The FTIR spectra of FC, NFC, BV, and NFC/BV nanoconjugates are presented in Figure 1. In the spectrum of *Fom*-extracted FC (Figure 1, FC), the strong peak around 3452 cm^{-1} corresponds to the combined hydrogen bonding and O–H stretching; the N–H stretching (from primary amines) was overlapped in this region. The specified absorption peaks and bands of the FC were detected at 1718 cm^{-1} (carbonyl (C=O) stretching of the secondary amide I band), peaks at 1539 cm^{-1} and 1324 cm^{-1} (designated the amide II (N–H) bending vibration and the absorption of amide III, respectively), and at 1079 cm^{-1} (belongs to the C–O–C stretching). The spectrum of NFC (Figure 1, NFC) indicated some differences from FC spectrum; the peak of 3452 cm^{-1} in FC became wider in NFC with amplified relative intensity, which indicates the enhancement in hydrogen bonding. The NFC spectrum showed also a sharp P=O peak at 1174 cm−1, indicating the cross-linkage with TPP. Generally, the main characteristic peaks and bands in FC spectrum appeared in NFC spectrum, but with slight shifting of them to close wavenumbers.
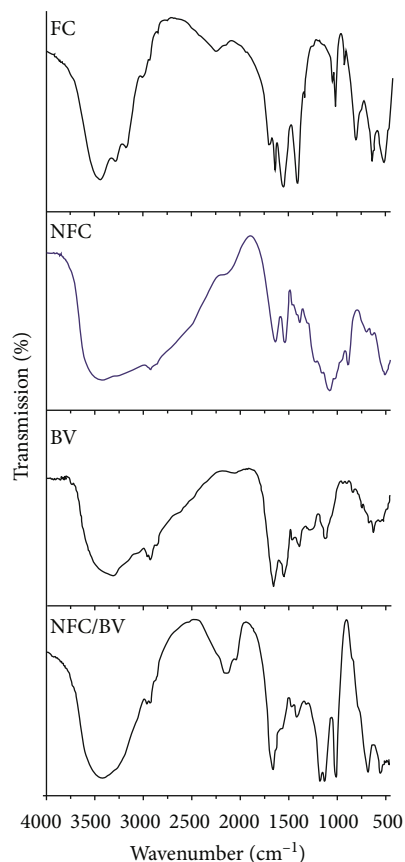
FIGURE 1: FTIR spectra of synthesized molecules of fungal chitosan (FC), bee venom (BV), nano-FC (NFC), and BV/NFC nanocomposite.

For the BV spectrum, the observed peak at absorbance region of 3250–3450 cm^{-1} indicates the free vibrations of N–H stretching. The FTIR spectrum of BV also indicated the characteristic amide bands, i.e., amide I (1651 cm^{-1}), amide II (1532 cm^{-1}), and the bands at 1112 cm^{-1} and 1040 cm^{-1} that indicate unsystematic coil conformation (Figure 1, BV). In the FTIR spectrum of NFC/BV nanoconjugate, the BV absorbance peak for N–H stretching at 3318 cm^{-1} was reduced and shifted to 3421 cm^{-1} (Figure 1, NFC/BV). The amide I indicated band in the BV at 1651 cm^{-1} was also shifted to a higher wavenumber (1654 cm^{-1}) in BV/NFC.

The characteristic attributes of synthesized NP from FC and BV are illustrated in Table 1.

The NFC had smaller average (mean) particle diameters, median diameter, and size range than BV/NFC nanocomposite. The PDI values were <0.5 for both synthesized NPs (0.262 for NFC and 0.414 for BV/NFC nanocomposite), which indicates a matched and favorable NP size distribution (Table 1). Both NP types had positive Z-potentialities; the BV loading into NFC slightly reduced their positivity from +33.7 (for NFC) to +27.2 (for BV/NFC nanocomposite).

The particle shape, size, and distribution, for BV/NFC nanocomposite, were further elucidated via TEM imaging (Figure 2). The nanoconjugate particles mostly appeared with spherical shapes and smooth surfaces, uniform distribution with size range of ~168-256 nm (Figure 2).

The calculated LC and EE, of BV in NFC, were 38.22 and 92.42%, respectively. The BV release from NFC was *in vitro* evaluated at pH 5.2 and 7.0, through direct dispersion during 30 h of release duration. The BV release patterns from NFC are plotted in Figure 3.

The BV release had a pH- and time-dependent manner; lower BV percentages were released in pH 7.1 than in pH 5.2. The releasing pattern revealed a burst BV release at the first 6 h; after that, gradual releases were detected with experiment prolongation for 30 h. The released BV ratios were 67.2 and 71.4% after 6 h, and the maximum release percentages were 76.2 and 81.3%, at the duration end, in pH 7.1 and 5.2, respectively.

The anticancer potentialities of NFC, BV, and FC/BV-NPs measured with the decrement of HeLa cell viability, after exposure to different concentrations from synthesized agents, are plotted in Figure 4. The entire agents had potent anticancer activity toward examined cells; the activities of all agents were dose-dependent. The most forceful agent was the NFC/BV nanoconjugates then the BV and lastly the NFC. After 24 h of exposure to a concentration of 500 μg/mL, only 8.3 and 22.3% of cells remained viable after treatment with NFC/BV-NPs and BV, respectively. The 200 μg/mL concentration from NFC/BV-NPs could kill 50% of cancerous cells after 24 h (Figure 4).

Fluorescent imaging was applied to elucidate the cytotoxic effects of NFC/BV composites toward examined cancerous cells (Figure 5). The potential apoptotic effect after HeLa cell treatment with NFC/BV nanoconjugates (at 500 μg/mL concentration) was investigated using DAPI staining (Figure 5, DAPI). The exposure to nanoconjugate induced observable morphological apoptosis signs in treated HeLa cells, e.g., membrane blebbing, cell shrinkage and rounding.

The apoptosis signs greatly increased and became more vigorous, with exposure prolongation from 24 to 48 h, to include most of the treated cancerous cells. While control cells had no apoptosis signs, the DAPI-stained treated cells had many brightly fluoresced fragments/nuclei; the DNA condensation and apoptosis signs increased dramatically in a time-dependent approach.

The cell apoptosis and necrosis were further elucidated via AO/PI double fluorescent staining (Figure 5, AO/PI); viable cancerous cells appeared with intact structures and green color for cells and nuclei. The early apoptosis signs include the appearance of chromatin condensation and bright green-stained nuclei, which clearly appeared after 24 h from treatment with NFC/BV nanoconjugate. The secondary necrosis and late apoptosis signs evidently appeared in HeLa cells after treatment for 48 h, with more chromatin condensation, dense orange-stained areas, and many stained nuclei with deep reddish-orange color.

4. Discussion

The achievement of FC was successfully conducted from *Fom* mycelia, which confirmed the investigations that indicated the high potentiality of fungi as sustainable sources for

TABLE 1: Characteristic attributes of synthesized nanoparticles from fungal chitosan (NFC) and its nanocomposite with bee venom (BV/NFC).

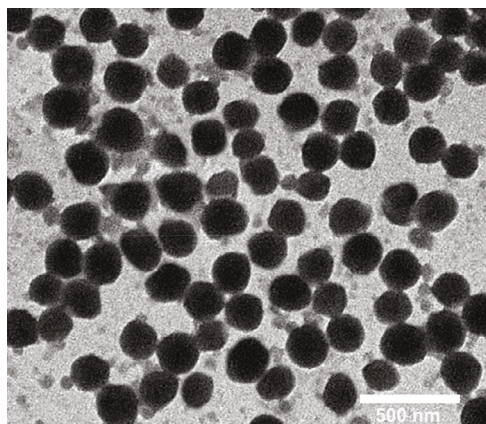| Nanoparticles	Size range (nm)	Median diameter (nm)	Mean diameter (nm)	Z-potential (mV)	PDI
NFC	92.1-157.3	121.6	129.1	+33.7	0.262
BV/NFC nanocomposite	147.3-269.6	186.3	192.4	+27.2	0.414

FIGURE 2: Transmission micrographs of synthesized nanocomposite from fungal chitosan and bee venom.

FIGURE 4: Cancer cell (HeLa) viability after exposure to nanofungal chitosan (FC-NPs), bee venom (BV), and their nanocomposite (FC/BV-NPs) for 24 h using different concentrations from each of them.
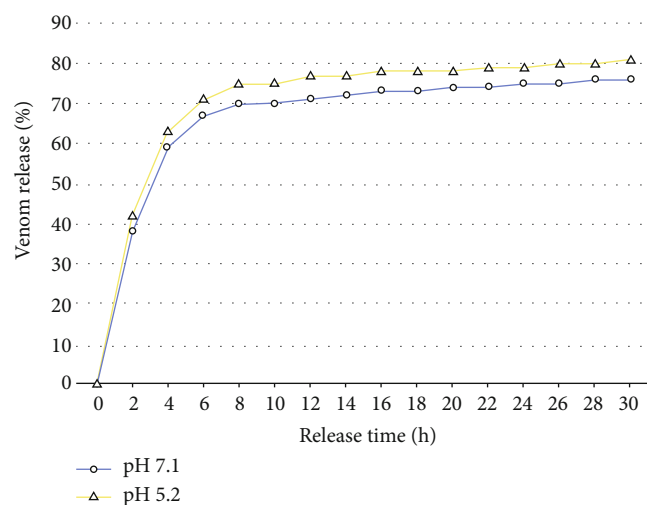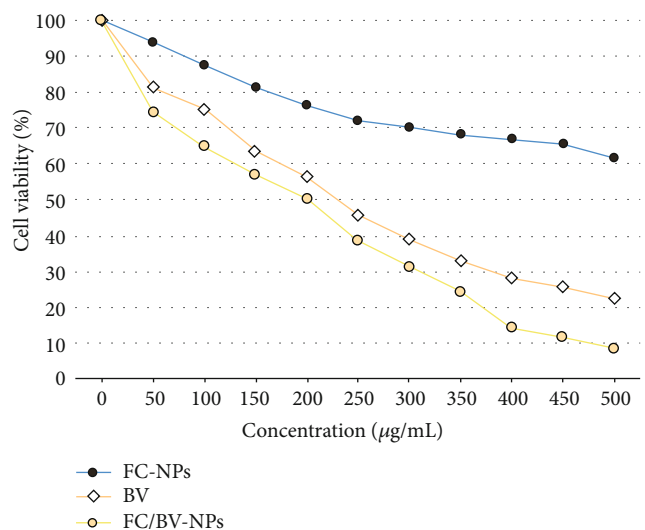

FIGURE 3: Bee venom release profile from fungal chitosan nanoparticles at different pH values (5.2 and 7.1) during the 30 h releasing period.

chitosan production [4–9, 22, 23]; these investigations recommended the application of FC, from many fungal species, in the biomedical and health-related fields.

The FTIR analysis of FC certified its comparable structure/groups to the standardized conventional chitosan [6, 33].

The slight shifting of many characteristic peaks and bands in FC spectrum to close wavenumbers in NFC spectrum validates the successful NFC cross-linkage and synthesis of targeted NPs [22]. The NFC and NFC/BV spectra were closely matched in most of the biochemical groups and wave-

number intensity; this indicates that BV did not chemically affect or change the NFC structure and accordingly maintain its biosafety for usage in the human body [29]. In the FTIR spectrum of NFC/BV nanoconjugate, the stretching and broadening of C–O (from NFC) and reduction of stretched N–H intensity (from BV) and their shifting to littler wavenumbers indicate the hydrogen bond formation between these active groups from BV and NFC [34].

The obtained data from "Zetasizer," regarding the synthesized NFC and BV/NFC nanoconjugate, revealed that BV/NFC nanoparticles had larger sizes than NFC particles; this could conceivably be due to the added molecular weight and composited structure after venom on nanochitosan [27], which verifies the elevated ability of current NFC to carry BV. For successful biomedical applications, functional nanocomposites are mostly manufactured in a NP size range from 20 up to 300 nm, considering that the "smallest particles could reach any part of the body" [35].

The BV release from NFC was very fast in the first 6 h of the experiment; this burst release is supposed to depend on the BV dissociation from the surface of NFC, as generally reported from loaded protein molecules on nanochitosan [21, 36]. Additionally, the early rapid release and diffusion of protein molecules from the surface of nanoparticles were stated as undeniable [37]. Subsequently, the slow BV release was seemingly attributed to slow degradation of entrapped protein molecules in NFC and the degradation of
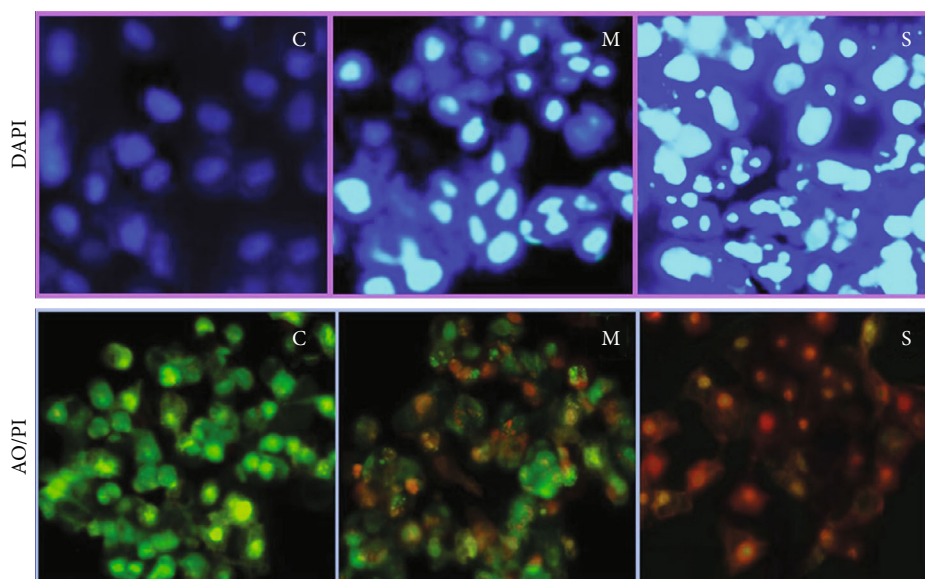
FIGURE 5: Fluorescent microscopic imaging of HeLa cancerous cells, stained with DAPI stain or acridine orange/propidium iodide (AO/PI) double staining, after treatment with 500 μg/mL from bee venom/fungal chitosan nanoparticles*. *C: control (untreated) cells; M: treated cells for 24 h; S: treated cells for 48 h.

nanoparticles itself [38]. The degradation rate of protein was supposed to exceed its releasing rate, after prolonged releasing period [39]. Additionally, BV was reported to engage the long chain of nanochitosan in a nonuniform manner, thus high percentages from it could be easily released in the early releasing period [28].

The release of BV was higher in pH 5.2 than in pH 7.1, which could be explained by the solubility preference of chitosan in weak acidic solutions than in neutral solutions; thus, the pH 5.2 condition could increase BV liberating from the solubilized NFC.

The induction of HeLa cell apoptosis/necrosis, after treatment with BV/NFC nanoconjugate, was evidenced via staining with fluorescent dyes. The lethal effect of BV/NFC nanoconjugates could be principally owed to BV anticancer potentiality, which was strengthened after loading onto NFC. The NFC polycationic nature is suggesting for facilitating particle attachment to tumor cells and enables more contact between BV and cell surface.

Animal venom peptides, especially BV, have a great potential for developing into biopharmaceuticals, with many limitations that could be overcome with their conjugation with polymeric nanocarriers like Cts to augment their chemical instability, half-lives, oral absorption, and target cytotoxicity [40].

Although the produced bioactive agents (NFC and BV) were extracted from fungal and insect sources, the transability of other biological components from these organisms to the human body is not expected because Cts and NFC are mostly polysaccharides extracted with harsh steps (e.g., very high alkalinity and temperature), leading to the elimination of any protein residues, while the BV is obtained from the bees' toxin glands and is anciently applied for treating various diseases with no evidences for genetic transferability during these treatments [13]. Nanoformulations are demon-

strated as well-suited for the administration of drug-like molecules; polymeric nanocarriers can enhance the drugs' half-life circulation and their deposition into diseased sites with diminished extravasation to healthy/normal tissues [41].

The BV antitumor activity was stated to depend primarily on close contact between its active constituents and cancer cells, which is essential to develop cell apoptosis/necrosis [42]. Melittin (the major protein constituent of BV) was confirmed for cancer therapy as a potent bioactive agent [43]; the main suggested functions of melittin involved cell membrane perturbing (leading to hemolytic and antimicrobial consequences) and the induction of vigorous structural alterations in these membranes (including pore formation, vesiculation, and fusion) [44]. Furthermore, melittin was verified to induce arrest in tumor cell cycle, inhibiting their growth, and apoptosis signs in different tumor cells [12]. Interestingly, BV melittin was demonstrated to specifically pursue cells that have extraordinary levels from Ras oncogene, i.e., tumor cells [45].

Apoptosis was appointed as the key function of BV anticancer action, as consequences from death receptor (DR) stimulation and inactivation of nuclear growth factor family kappa B (NF-κB) in cancer cell [11].

The application of AO/PI double fluorescent staining, for quantifying the apoptotic and necrotic consequence of BV/NFC nanoconjugate on HeLa cells, proved its applicability and efficiency. The variations in cell staining with green, orange, and reddish-orange as indicators for early apoptosis, late apoptosis, and secondary necrosis, respectively, were illustrated [31]. The tumor cell death indicators (apoptosis, necrosis, and lysis) were stated as the potential mechanisms, by which BV could inhibit tumor development [17]. A previous study [46] indicated that BV anticancer activity was more forceful against V79 than for HeLa cells; and its effect toward both cells was dose-dependent. The BV

role in the *in vivo* inhibition of cancer growth and proliferation was addressed to involve immune response stimulation of lymph nodes [42].

Interestingly, BV was illustrated to induce leukemia cell apoptosis, with no cytotoxicity on normal cells of the bone marrow [15]; the main regulators of BV-induced leukemic cell apoptosis are caspase-3 and Bcl-2 via suppression of mitogen-activated signaling paths [14]. The preceding flow cytometric analysis indicated BV capability for inducing ROS (reactive oxygen species) production, increasing cytoplasmic Ca^{2+} levels, releasing cytochrome C due to reduced potentials of mitochondrial membrane, and promoting caspase-3 activation, which consequently caused cell apoptosis [16].

The amount of BV binding sites from carbohydrate/amines on cancerous cell membranes was suggested to explain the varying sensitivity of cancer types to BV components [46]; thus, it is supposable here that loaded NFC with BV could generate more binding sites with HeLa cell membranes and accordingly strengthen the BV antiproliferative action toward these cells.

The modern approaches for NP safety assessment recommended the usage of in vitro/ex vivo models as essential prerequisites for their translation into applicable products [47]. The Safe-by-Design (SbD) concept is applied for the assessment of nanomaterial and nanopolymer potential consequences on the environment and human health and their uses to develop nanomedicines; according to the latest SbD criteria, NFC could be regarded as an ideal safe "nanobiocarrier" for delivering BV into the human body to fight cancer cells [48, 49].

5. Conclusion

The grown mycelia of *Fom* were innovatively employed as FC source, which was successfully utilized for NFC production and loading with BV. The BV/NFC nanoconjugate had favorable structural and biochemical physiognomies, plus their augmented anticancer bioactivity against cervix carcinoma (HeLa) cells. The BV/NFC nanoconjugate could induce serious apoptosis signs in HeLa cells in a time- and dose-dependent manner. The application and extra evaluation of BV/NFC nanoconjugates are strongly recommended as effective and natural anticancer agents.

Data Availability

The datasets generated during and/or analyzed during the current study are available from the corresponding author on reasonable request.

Conflicts of Interest

The authors declare that they have no conflicts of interest.

Acknowledgments

References

[1] E. I. Rabea, M. E. Badawy, C. V. Stevens, G. Smagghe, and W. Steurbaut, "Chitosan as antimicrobial agent: applications and mode of action," *Biomacromolecules*, vol. 4, no. 6, pp. 1457–1465, 2003.

[2] O. Felt, P. Buri, and R. Gurny, "Chitosan: a unique polysaccharide for drug delivery," *Drug Development and Industrial Pharmacy*, vol. 24, no. 11, pp. 979–993, 1998.

[3] A. Ali and S. Ahmed, "A review on chitosan and its nanocomposites in drug delivery," *International Journal of Biological Macromolecules*, vol. 109, pp. 273–286, 2018.

[4] A. A. Tayel, S. Moussa, K. Opwis, D. Knittel, E. Schollmeyer, and A. Nickisch-Hartfiel, "Inhibition of microbial pathogens by fungal chitosan," *International Journal of Biological Macromolecules*, vol. 47, no. 1, pp. 10–14, 2010.

[5] S. H. Moussa, A. A. Tayel, and A. I. Al-Turki, "Evaluation of fungal chitosan as a biocontrol and antibacterial agent using fluorescence-labeling," *International Journal of Biological Macromolecules*, vol. 54, pp. 204–208, 2013.

[6] A. A. Tayel, S. I. A. Ibrahim, M. A. al-Saman, and S. H. Moussa, "Production of fungal chitosan from date wastes and its application as a biopreservative for minced meat," *International Journal of Biological Macromolecules*, vol. 69, pp. 471–475, 2014.

[7] A. A. Tayel, M. M. Gharieb, H. R. Zaki, and N. M. Elguindy, "Bio-clarification of water from heavy metals and microbial effluence using fungal chitosan," *International Journal of Biological Macromolecules*, vol. 83, pp. 277–281, 2016.

[8] A. A. Tayel, "Microbial chitosan as a biopreservative for fish sausages," *International Journal of Biological Macromolecules*, vol. 93, article Part A, pp. 41–46, 2016.

[9] M. S. Alsaggaf, S. H. Moussa, N. M. Elguindy, and A. A. Tayel, "Fungal chitosan and *Lycium barbarum* extract as anti-listeria and quality preservatives in minced catfish," *International Journal of Biological Macromolecules*, vol. 104, article Part A, pp. 854–861, 2017.

[10] H. Raghuraman and A. Chattopadhyay, "Melittin: a membrane-active peptide with diverse functions," *Bioscience Reports*, vol. 27, no. 4-5, pp. 189–223, 2007.

[11] S. C. Pak, "Health benefits and uses in medicine of bee venom," in *Bee Products - Chemical and Biological Properties*, J. M. Alvarez-Suarez, Ed., pp. 287–306, Springer Int. Pub. AG, Cham, Switzerland, 2017.

[12] N. Oršolić, L. Šver, K. Bendelja, and I. Bašić, "Antitumor activity of bee venom," *Periodicum Biologorum*, vol. 103, pp. 49–54, 2001.

[13] A. Aufschnaiter, V. Kohler, S. Khalifa et al., "Apitoxin and its components against cancer, neurodegeneration and rheumatoid arthritis: limitations and possibilities," *Toxins*, vol. 12, no. 2, p. 66, 2020.

[14] S. J. Hong, G. S. Rim, H. I. Yang et al., "Bee venom induces apoptosis through caspase-3 activation in synovial fibroblasts of patients with rheumatoid arthritis," *Toxicon*, vol. 46, no. 1, pp. 39–45, 2005.

[15] D. O. Moon, S. Y. Park, M. S. Heo et al., "Key regulators in bee venom-induced apoptosis are Bcl-2 and caspase-3 in human leukemic U937 cells through downregulation of ERK and Akt," *International Immunopharmacology*, vol. 6, no. 12, pp. 1796–1807, 2006.

[16] S. W. Ip, H. C. Wei, J. P. Lin et al., "Bee venom induced cell cycle arrest and apoptosis in human cervical epidermoid

carcinoma Ca Ski cells," *Anticancer Research*, vol. 28, no. 2A, pp. 833–842, 2008.

[17] N. Oršolić, "Bee venom in cancer therapy," *Cancer Metastasis Reviews*, vol. 31, no. 1-2, pp. 173–194, 2012.

[18] G. Gajski and V. Garaj-Vrhovac, "Melittin: a lytic peptide with anticancer properties," *Environmental Toxicology and Pharmacology*, vol. 36, no. 2, pp. 697–705, 2013.

[19] S. K. Sahoo, S. Parveen, and J. J. Panda, "The present and future of nanotechnology in human health care," *Nanomedicine: Nanotechnology, Biology and Medicine*, vol. 3, no. 1, pp. 20–31, 2007.

[20] Q. Gan and T. Wang, "Chitosan nanoparticle as protein delivery carrier—systematic examination of fabrication conditions for efficient loading and release," *Colloids and Surfaces B: Biointerfaces*, vol. 59, no. 1, pp. 24–34, 2007.

[21] S. Jarudilokkul, A. Tongthammachat, and V. Boonamnuayvittaya, "Preparation of chitosan nanoparticles for encapsulation and release of protein," *Korean Journal of Chemical Engineering*, vol. 28, no. 5, pp. 1247–1251, 2011.

[22] S. Alsharari, A. A. Tayel, and S. H. Moussa, "Soil emendation with nano-fungal chitosan for heavy metals biosorption," *International Journal of Biological Macromolecules*, vol. 118, article Part B, pp. 2265–2268, 2018.

[23] H. A. El Rabey, F. M. Almutairi, A. I. Alalawy et al., "Augmented control of drug-resistant *Candida* spp. via fluconazole loading into fungal chitosan nanoparticles," *International Journal of Biological Macromolecules*, vol. 141, pp. 511–516, 2019.

[24] N. M. Dounighi, M. Damavandi, H. Zolfagharian, and S. Moradi, "Preparing and characterizing chitosan nanoparticles containing *Hemiscorpius lepturus* scorpion venom as an antigen delivery system," *Archives of Razi Institute*, vol. 67, pp. 145–153, 2012.

[25] N. Dounighi, M. Mehrabi, M. R. Avadi, H. Zolfagharian, and M. Rezayat, "Preparation, characterization and stability investigation of chitosan nanoparticles loaded with the *Echis carinatus* snake venom as a novel delivery system," *Archives of Razi Institute*, vol. 70, pp. 269–277, 2015.

[26] N. Mohammadpour Dounighi, R. Eskandari, M. R. Avadi, H. Zolfagharian, A. Mir Mohammad Sadeghi, and M. Rezayat, "Preparation and in vitro characterization of chitosan nanoparticles containing *Mesobuthus eupeus* scorpion venom as an antigen delivery system," *Journal of Venomous Animals and Toxins including Tropical Diseases*, vol. 18, no. 1, pp. 44–52, 2012.

[27] K. S. Rocha Soares, J. L. Cardozo Fonseca, M. A. Oliveira Bitencourt, K. S. C. R. Santos, A. A. Silva-Júnior, and M. F. Fernandes-Pedrosa, "Serum production against *Tityus serrulatus* scorpion venom using cross-linked chitosan nanoparticles as immunoadjuvant," *Toxicon*, vol. 60, no. 8, pp. 1349–1354, 2012.

[28] F. A. Taher, W. A. Moselhy, A. F. Mohamed, S. E. Didamony, K. M. Metwalley, and A. B. Zayed, "Preparation and characterization of shrimp derived chitosan and evaluation of its efficiency as bee venom delivery for cancer treatment," *International Journal of Advanced Research*, vol. 5, no. 5, pp. 370–388, 2017.

[29] A. Baxter, M. Dillon, K. D. Anthony Taylor, and G. A. F. Roberts, "Improved method for I.R. determination of the degree of N-acetylation of chitosan," *International Journal of Biological Macromolecules*, vol. 14, no. 3, pp. 166–169, 1992.

[30] D. Chowrasia, C. Karthikeyan, L. Choure et al., "Synthesis, characterization and anti cancer activity of some fluorinated 3,6-diaryl-[1,2,4]triazolo[3,4-b][1,3,4]thiadiazoles," *Arabian Journal of Chemistry*, vol. 10, pp. S2424–S2428, 2017.

[31] M. Hajrezaie, M. Paydar, C. Y. Looi et al., "Apoptotic effect of novel Schiff based $CdCl_2(C_{14}H_{21}N_3O_2)$ complex is mediated via activation of the mitochondrial pathway in colon cancer cells," *Scientific Reports*, vol. 5, no. 1, article 9097, 2015.

[32] M. A. Rahman and A. Hussain, "Anticancer activity and apoptosis inducing effect of methanolic extract of *Cordia dichotoma* against human cancer cell line," *Bangladesh Journal of Pharmacology*, vol. 10, no. 1, pp. 27–34, 2015.

[33] A. A. Tayel, S. H. Moussa, W. F. El-Tras, N. M. Elguindy, and K. Opwis, "Antimicrobial textile treated with chitosan from *Aspergillus niger* mycelial waste," *International Journal of Biological Macromolecules*, vol. 49, no. 2, pp. 241–245, 2011.

[34] M. Qiao, D. Chen, T. Hao, X. Zhao, H. Hu, and X. Ma, "Effect of bee venom peptide-copolymer interactions on thermosensitive hydrogel delivery systems," *International Journal of Pharmaceutics*, vol. 345, no. 1-2, pp. 116–124, 2007.

[35] H. F. Krug and P. Wick, "Nanotoxicology: an interdisciplinary challenge," *Angewandte Chemie (International Ed. in English)*, vol. 50, no. 6, pp. 1260–1278, 2011.

[36] Q. Gan, T. Wang, C. Cochrane, and P. McCarron, "Modulation of surface charge, particle size and morphological properties of chitosan–TPP nanoparticles intended for gene delivery," *Colloids and Surfaces B: Biointerfaces*, vol. 44, no. 2-3, pp. 65–73, 2005.

[37] S. Zhou, X. Deng, and X. Li, "Investigation on a novel core-coated microspheres protein delivery system," *Journal of Controlled Release*, vol. 75, no. 1-2, pp. 27–36, 2001.

[38] S. Zhou, X. Deng, M. Yuan, and X. Li, "Investigation on preparation and protein release of biodegradable polymer microspheres as drug-delivery system," *Journal of Applied Polymer Science*, vol. 84, no. 4, pp. 778–784, 2002.

[39] M. Amidi, S. G. Romeijn, G. Borchard, H. E. Junginger, W. E. Hennink, and W. Jiskoot, "Preparation and characterization of protein-loaded N-trimethyl chitosan nanoparticles as nasal delivery system," *Journal of Controlled Release*, vol. 111, no. 1-2, pp. 107–116, 2006.

[40] A. P. dos Santos, T. G. de Araújo, and G. Rádis-Baptista, "Nanoparticles functionalized with venom-derived peptides and toxins for pharmaceutical applications," *Current Pharmaceutical Biotechnology*, vol. 21, no. 2, pp. 97–109, 2020.

[41] S. Bisso and J. C. Leroux, "Nanopharmaceuticals: a focus on their clinical translatability," *International Journal of Pharmaceutics*, vol. 578, article 119098, 2020.

[42] N. Oršolić, L. Sver, S. Verstovsek, S. Terzic, and I. Basic, "Inhibition of mammary carcinoma cell proliferation in vitro and tumor growth in vivo by bee venom," *Toxicon*, vol. 41, no. 7, pp. 861–870, 2003.

[43] C. E. Dempsey, "The actions of melittin on membranes," *Biochimica et Biophysica Acta*, vol. 1031, no. 2, pp. 143–161, 1990.

[44] C. Leuschner and W. Hansel, "Membrane disrupting lytic peptides for cancer treatments," *Current Pharmaceutical Design*, vol. 10, no. 19, pp. 2299–2310, 2004.

[45] S. V. Sharma, "Melittin resistance: a counterselection for ras transformation," *Oncogene*, vol. 7, no. 2, pp. 193–201, 1992.

[46] N. Oršolić, "Potentiation of bleomycin lethality in HeLa and V79 cells by bee venom," *Archives of Industrial Hygiene and Toxicology*, vol. 60, no. 3, pp. 317–326, 2009.

[47] P. Wick, S. Chortarea, O. T. Guenat et al., "In vitro-ex vivo model systems for nanosafety assessment," *European Journal of Nanomedicine*, vol. 7, no. 3, pp. 169–179, 2015.

[48] S. Jesus, M. Schmutz, C. Som, G. Borchard, P. Wick, and O. Borges, "Hazard assessment of polymeric nanobiomaterials for drug delivery: what can we learn from literature so far," *Frontiers in Bioengineering and Biotechnology*, vol. 7, p. 261, 2019.

[49] M. Schmutz, O. Borges, S. Jesus et al., "A methodological safe-by-design approach for the development of nanomedicines," *Frontiers in Bioengineering and Biotechnology*, vol. 8, p. 258, 2020.